

ABSTRACT

Title of Document: **AN INVESTIGATION OF SOLID OXIDE
ELECTROCHEMICAL CELL
CHEMISTRY: AN OPERANDO
SPECTROSCOPIC APPROACH**

Yi Yu
Doctor of Philosophy, 2014

Directed By: Professor Bryan W. Eichhorn
Department of Chemistry and Biochemistry

Investigations of electrochemical reactions on solid oxide based electrochemical cells under operating conditions are described in this dissertation. *Operando* capabilities of ambient pressure X-ray photoelectron spectroscopy are utilized to study the specially designed single-sided electrochemical cells and to extract detailed information of cell processes. Mixed-ionic-electronic-conducting materials of cerium oxide are used as electrocatalysts.

Mappings of local surface potentials and length scales of the electrochemically active region on thin film CeO_{2-x} electrocatalysts are obtained in studies of water electrolysis and hydrogen electro-oxidation reactions. Electrochemically active region

is shown extend 150 - 200 μm away from current collectors. Foreign elements of silicon and carbon on the electrode are found as excellent trace markers of surface potentials and active region. The observations of transient intermediates (OH^- and Ce^{3+}) accumulation in the active region on CeO_{2-x} electrode allow for identification of the rate-limiting charge transfer process ($\text{H}_2\text{O} + \text{Ce}^{3+} \leftrightarrow \text{Ce}^{4+} + \text{OH}^- + \text{H}\cdot$) in both H_2O electrolysis and H_2 electro-oxidation reactions. The observed potential separation of the adsorbed OH^- and incorporated O^{2-} ions is interpreted by the effective double layer model and the surface potential step model, which provides insights into the gas-solid interface chemistry.

From studies of carbon dioxide electrolysis and carbon monoxide electro-oxidation over CeO_{2-x} -based solid oxide electrochemical cells, carbonate are identified as reaction intermediates in both electrochemical reactions. The steady-state concentration increase of CO_3^{2-} during CO_2 electrolysis and its slight decrease during CO electro-oxidation on CeO_{2-x} electrode suggest the charge transfer process to/from CO_3^{2-} is a rate-limiting process. The graphitic carbon formed on the CeO_{2-x} electrode surfaces during CO_2 electrolysis extends the electrochemically active region away from the Au electron source by enhancing the electronic conductivity of cerium oxide. Measurements of overpotentials at the electrode-electrolyte interface reveal very high charge transfer resistance at the interface for CO_2 electrolysis that dominates the cell losses in these environments.

Mechanistic information extracted from investigating these solid oxide electrochemical cells provides insight into the high temperature surface chemistry on mixed-ionic-electronic-conducting ceria electrodes, and is valuable and guiding to the

development of solid oxide fuel cells due to the similar chemical processes occurring in these electrochemical devices.

**AN INVESTIGATION OF SOLID OXIDE ELECTROCHEMICAL CELL
CHEMISTRY: AN OPERANDO SPECTROSCOPIC APPROACH**

By

Yi Yu

Dissertation submitted to the Faculty of the Graduate School of the
University of Maryland, College Park, in partial fulfillment
of the requirements for the degree of
Doctor of Philosophy
2014

Advisory Committee:

Professor Bryan W. Eichhorn, Chair

Professor Janice E. Reutt-Robey

Professor Sang Bok Lee

Professor Andrei Vedernikov

Professor Lourdes G. Salamanca-Riba, Dean's Representative

© Copyright by
Yi Yu
2014

Dedicated to my parents Guojun Yu and Peiran Li

Acknowledgements

I would like to express my greatest gratitude to Professor Bryan Eichhorn for all his help and guidance through my time at the University of Maryland. I would like to thank Dr. Chunjuan Zhang and Dr. Karen J. Gaskell for their discussions and insights to this work. I am very grateful to Professor Zhi Liu, Dr. Michael E. Grass, Dr. Rui Chang, and Baohua Mao at the Advanced Light Source at Lawrence Berkeley National Laboratory for their generous help to my experimental work. I also thank the members of the Eichhorn's research group: Zhufang Liu, Yang Peng, Aldo Ponce, Hao Lei, Christopher J. Snyder, Sanem Kocak, Dennis H. Mayo, Domonique Downing, Christopher M. Sims, Samantha DeCarlo, Aaron I. Geller, Jonathan F. Senn, Kim Huynh, and Luning Wang.

Members of the solid oxide fuel cell project also deserve an incredible amount of credit. They are Dr. Jeffrey C. Owrutsky, Dr. Michael B. Pomfret, Dr. Daniel A. Steinhurst, Professor Robert A. Walker, and Professor Gregory S. Jackson.

Thanks also to the members of my committee: Professor Janice Reutt-Robey, Professor Sang Bok Lee, Professor Andrei Vedernikov, and Professor Lourdes G. Salamanca-Riba for their helpful recommendations.

Support from the Office of Naval Research through Contract No. N000140510711 (Dr. Michele Anderson program manager) is greatly acknowledged. I thank the University of Maryland Nanocenter and the University of Maryland Energy Research Center for support. Department of Chemistry and Biochemistry at

the University of Maryland – College Park also provided the Millard and Alexander Fellowship that supported my Ph.D. work.

Finally, I would like to thank my parents for their unconditional support and unending love throughout my life.

Table of Contents

Dedication	ii
Acknowledgements	iii
Table of Contents	v
List of Publications	x
List of Figures.....	xi
List of Abbreviations	xviii
Chapter 1 General Introduction.....	1
1.1 Fuel Cells	3
1.2 Solid Oxide Fuel Cells	6
1.2.1 Historical Background	7
1.2.2 Operating Principles	8
1.2.3 Nernst Potential.....	8
1.2.4 Polarization	9
1.2.5 SOFC Components	11
1.2.6 Internal Reforming.....	21
1.3 X-ray Photoelectron Spectroscopy	23
1.3.1 Historic Background	23
1.3.2 Surface Analysis by X-ray Photoelectron Spectroscopy	24
1.3.3 Synchrotron Radiation Sources.....	29
1.3.4 Ambient Pressure X-ray Photoelectron Spectroscopy.....	32
1.4 Field of Research	36
1.5 Scope of the Dissertation	38

Chapter 2 Activity Mapping and Potential Mapping on Solid Oxide

Electrochemical Cell by <i>Operando</i> XPS	42
2.1 Introduction.....	42
2.1.1 Kinetic Energy Shift of Photoelectrons	43
2.1.2 Scope of the Chapter.....	44
2.2 Experimental	45
2.2.1 Solid Oxide Electrochemical Cell Preparation	45
2.2.2 Electrochemical Measurements	47
2.2.3 <i>Operando</i> Ambient Pressure X-ray Photoelectron Spectroscopy Measurement.....	48
2.3 Results & Discussions.....	49
2.3.1 Electrochemistry Characterization.....	52
2.3.2 Two-Dimensional X-ray Photoelectron Spectroscopy Mapping.....	55
2.3.3 Local Surface Potential Mapping	57
2.3.4 Electrochemically Active Region	58
2.3.5 Overpotential at the Electrode-Electrolyte Interface	62
2.4 Summary	66

Chapter 3 Water Electrolysis and Hydrogen Electro-Oxidation on Ceria-Based

Solid Oxide Electrochemical Cells	67
3.1 Introduction.....	67
3.2 Experimental	70
3.2.1 Solid Oxide Electrochemical Cell Preparation	70
3.2.2 Electrochemical Measurements	71

3.2.3 <i>Operando</i> Ambient Pressure X-ray Photoelectron Spectroscopy	
Measurement.....	72
3.3 Results & Discussions.....	73
3.3.1 Electrochemistry Characterization.....	76
3.3.2 Surface Hydroxyl Intermediates	78
3.3.3 Local Surface Potential Shifts of Hydroxyl and Oxide Ion	80
3.3.4 Dipole Model	81
3.3.5 Rate-Limiting Process.....	85
3.3.6 Surface Potential Step	86
3.3.7 Surface Potential Step versus Activation Overpotential.....	89
3.4 Summary	90
Chapter 4 Carbon Dioxide Activation and Carbonate Intermediates on Solid	
Oxide Electrochemical Cells	91
4.1 Introduction.....	91
4.1.1 Carbon Dioxide Reduction	91
4.1.2 Ceria-Based Solid Oxide Electrolysis Cells	94
4.1.3 Scope of the Chapter	95
4.2 Experimental	96
4.2.1 Solid Oxide Electrochemical Cell Preparation	96
4.2.2 Electrochemical Measurements	96
4.2.3 <i>Operando</i> Ambient Pressure X-ray Photoelectron Spectroscopy	
Measurement.....	97
4.3 Results & Discussions.....	98

4.3.1 C 1s and O 1s XPS.....	101
4.3.2 Reversible Change in Carbonate Coverage	104
4.3.3 Rate-Limiting Process.....	108
4.3.4 Reaction Mechanism of CO ₂ Activation	111
4.3.5 Overpotentials at the Pt-YSZ Interface.....	112
4.3.6 Electrochemically Active Region in CO/CO ₂ System.....	115
4.4 Summary	116
Chapter 5 Carbon Deposits and Pt-YSZ Overpotentials on Ceria-Based Solid Oxide Electrochemical Cell.....	117
5.1 Introduction.....	117
5.1.1 Carbon Dioxide Reduction on Ceria Catalyst.....	117
5.1.2 Scope of the Chapter	118
5.2 Experimental	119
5.2.1 Solid Oxide Electrochemical Cell Preparation	119
5.2.2 Electrochemical Measurements	120
5.2.3 <i>Operando</i> Ambient Pressure X-ray Photoelectron Spectroscopy Measurement.....	121
5.3 Results & Discussion	121
5.3.1 Graphitic Carbon Deposition on Ceria	124
5.3.2 Interpretations of Graphitic Carbon Deposition	126
5.3.3 Extension of Electrochemically Active Region.....	128
5.3.4 Overpotentials at the Electrode-Electrolyte Interface.....	130
5.3.5 Comparison with Studies of H ₂ /H ₂ O	132

5.4 Summary	132
Chapter 6 Summary and Future Work	133
6.1 Introduction.....	133
6.2 Summary of Major Results	133
6.2.1 Fundamental Characterization of Solid Oxide Electrochemical Cell Chemistry	133
6.2.2 Reaction Intermediates and Mechanisms.....	134
6.3 Future Works & Recommendations.....	135
6.3.1 Further Applications of <i>Operando</i> Techniques	135
6.3.2 <i>Operando</i> Studies of Electrolysis on Solid Oxide Electrocatalyst	136
6.3.3 Poisoning Mechanisms	137
6.3.4 Characterization of Cathode Materials	138
References	139

List of Publications

1. “Multielement Activity Mapping and Potential Mapping in Solid Oxide Electrochemical cells through the use of operando XPS” Zhang, C.; Grass, M. E.; Yu, Y.; Gaskell, K. J.; DeCaluwe, S. C.; Chang, R.; Jackson, G. S.; Hussain, Z.; Bluhm, H.; Eichhorn, B. W.; Liu, Z. *ACS Catalysis* 2012, 2, 2297
2. “Mechanistic Studies of Water Electrolysis and Hydrogen Electro-Oxidation on High Temperature Ceria-Based Solid Oxide Electrochemical Cells” Zhang, C.; Yu, Y.; Grass, M. E.; Dejoie, C.; Ding, W.; Gaskell, K.; Jabeen, N.; Hong, Y. P.; Shavorskiy, A.; Bluhm, H.; Li, W.-X.; Jackson, G. S.; Hussain, Z.; Liu, Z.; Eichhorn, B. W. *J. Am. Chem. Soc.* 2013, 135, 11572
3. “Carbon Deposits and Pt/YSZ Overpotentials in CO/CO₂ Solid Oxide Electrochemical Cells” Yu, Y.; Geller, A. I.; Mao, B.; Chang, R.; Liu, Z.; Eichhorn, B. W. *ECS Trans.* 2013, 57(1), 3119
4. “CO₂ Activation and Carbonate Intermediates: An *Operando* AP-XPS Study of CO₂ Electrolysis Reactions on Solid Oxide Electrochemical Cells” Yu, Y.; Mao, B.; Geller, A. I.; Chang, R.; Gaskell, K.; Liu, Z.; Eichhorn, B. W. *Phys. Chem. Chem. Phys.* 2014, 16, 11633

List of Figures

Figure 1-1. Schematic diagram of a generic fuel cell operation.....	5
Figure 1-2. Summary of various fuel cell types.....	6
Figure 1-3. Schematic diagram of a solid oxide fuel cell (SOFC).....	8
Figure 1-4. Typical fuel cell voltage-current characteristic at 800 °C with pure hydrogen as fuel.....	10
Figure 1-5. Variation of ionic conductivity of stabilized zirconia with dopant concentration (T = 807 °C).....	13
Figure 1-6. Schematic representation of lattice structure of perovskite, ABO ₃	14
Figure 1-7. A schematic drawing of the triple phase boundary (red solid line) in the anode region of a solid oxide fuel cell.....	17
Figure 1-8. Electrical conductivity measured at 1000 °C as a function of Ni content of Ni/YSZ cermet fired at different temperatures from 1200 to 1350 °C.....	18
Figure 1-9. Crystal structure of cerium oxide.....	20
Figure 1-10. Oxygen deficiency x in CeO _{2-x} as a function of oxygen equilibrium pressure and temperature.....	20
Figure 1-11. A schematic view of the photoemission process.....	24
Figure 1-12. A representative wide-range XPS scan of platinum spontaneously deposited on rhodium.....	25
Figure 1-13. The schematic drawing of the energy level diagram of core level photoelectron spectroscopy.....	26

Figure 1-14. Mean free path of electron in solid as a function of electron kinetic energy.....	29
Figure 1-15. A scheme of the Advanced Light Source (ALS) at Lawrence Berkeley National Laboratory (LBNL).....	31
Figure 1-16. A schematic drawing of the ALS endstation.....	34
Figure 1-17. Principle of AP-XPS differentially pump system.....	34
Figure 1-18. Exchangeable conic aperture separating the first pumping stage from the high pressure chamber.....	35
Figure 2-1. SEM image of the cross-section structure for a fractured 50 nm thick CeO _{2-x} cell.....	46
Figure 2-2. A photograph of an operating cell with the XPS electron detector (the cone) and three electrical contact probes (bent wires).....	48
Figure 2-3. Schematic illustration of cell geometry.....	50
Figure 2-4. Schematic illustrations of cell cross sections illustrating current flow directions and surface reactions under different biases.....	51
Figure 2-5. Linear sweep voltammetry (LSV) polarization curves of cells with different CeO _{2-x} film thicknesses (0, 50, and 250 nm) measured at ~720 °C with 0.5 Torr of 1:1 H ₂ /H ₂ O mixture.....	53
Figure 2-6. Electrochemical impedance spectroscopy (EIS) of a 250-nm-thick CeO _{2-x} cell under varied applied biases (-1.0, -0.3, OCV, +0.3, and +1.0 V) at ~720 °C with 0.5 Torr of 1:1 H ₂ /H ₂ O mixture.....	54
Figure 2-7. Spatially resolved XPS spectra of the C 1s, Si 2p, Ce 4d, and Zr 3d spectra obtained with a two-dimensional (2D) area detector on a 250-nm-	

thick CeO _{2-x} cell at +1.2 V applied potential (~720 °C with 0.5 Torr of 1:1 H ₂ /H ₂ O mixtures).....	56
Figure 2-8. Plots of the local surface potentials calculated from shifts in photoelectron kinetic energy away from OCV condition.....	58
Figure 2-9. Signatures of the electrochemically active region (yellow boxes) on the 50-nm and 250-nm thick CeO _{2-x} electrodes under applied biases (± 1.2 V) at ~720 °C with 0.5 Torr of 1:1 H ₂ /H ₂ O mixture.....	59
Figure 2-10. The relative concentrations of Ce ⁴⁺ measured <i>operando</i> under +1.2 V and -1.2 V at ~720 °C with 0.5 Torr of 1:1 H ₂ /H ₂ O mixture.....	60
Figure 2-11. The relative carbon concentration on the CeO _{2-x} surface after running the cells at ± 1.2 V with 0.5 Torr of 1:1 H ₂ /H ₂ O mixtures for a few cycles.....	61
Figure 2-12. Spatially resolved Pt 4f and Zr 3d spectra of the 250-nm-thick CeO _{2-x} cell at -1.2 V applied potential (~720 °C with 0.5 Torr of 1:1 H ₂ /H ₂ O mixtures).....	63
Figure 2-13. The Pt ⁰ and Zr ⁴⁺ surface potentials across the Pt-YSZ interface.....	65
Figure 3-1. Cross-sectional SEM image of a fractured cell showing the ~800 nm CeO _{2-x} film deposited on the YSZ electrolyte.....	71
Figure 3-2. Schematic drawing (not to scale) of the solid oxide electrochemical cell (SOC) assembly.....	73
Figure 3-3. Proposed surface electrochemical reaction mechanism under positive applied bias.....	75
Figure 3-4. Electrochemical linear sweep voltammetry (LSV) collected on the SOC	

with an 800-nm-thick ceria electrode under conditions of ~700 °C, 0.5 Torr 1:1 H ₂ /H ₂ O mixture.....	77
Figure 3-5. Electrochemical impedance spectroscopy (with 10 mV AC oscillating amplitude at zero DC applied bias) recorded on the SOC with an 800-nm-thick ceria electrode under conditions of ~700 °C, 0.5 Torr 1:1 H ₂ /H ₂ O mixture.....	77
Figure 3-6. Spatially resolved second derivative of the two-dimensional O 1s spectra collected under +1.2 V applied bias (~700 °C with 0.5 Torr of 1:1 H ₂ /H ₂ O mixtures).....	78
Figure 3-7. One representative 20-μm slice of O 1s spectra at x = -0.155 nm under +1.2 V (~700 °C with 0.5 Torr of 1:1 H ₂ /H ₂ O mixtures), fitted with gas-phase H ₂ O, OH ⁻ surface adsorbates, and solid-phase O ²⁻ species.....	79
Figure 3-8. Relative shifts in apparent BE under applied bias (±1.2 V) away from OCV for OH ⁻ and O ²⁻ peaks (~700 °C with 0.5 Torr of 1:1 H ₂ /H ₂ O mixtures).....	80
Figure 3-9. Schematic representation of bond dipoles for the Ce ³⁺ -OH and Ce ⁴⁺ -OH interactions on the CeO _{2-x} surface.....	82
Figure 3-10. Fraction of OH ⁻ and O ²⁻ under OCV and +1.2 V applied biases extracted from O 1s XPS spectra (~700 °C with 0.5 Torr of 1:1 H ₂ /H ₂ O mixtures).....	83
Figure 3-11. Spatially resolved Ce redox changes (Ce ³⁺ fraction) calculated from fitted Ce 4d spectra under OCV and ±1.2 V applied biases (~700 °C with 0.5 Torr of 1:1 H ₂ /H ₂ O mixtures).....	84

Figure 3-12. Spatially resolved BE separations (<i>i.e.</i> , surface potential steps) between surface OH ⁻ adsorbates and solid phase of O ²⁻ derived from O 1s spectra under OCV and ±1.2 V applied biases (~700 °C with 0.5 Torr of 1:1 H ₂ /H ₂ O mixtures).....	84
Figure 3-13. Correlation between Ce ³⁺ fraction changes and surface potential step changes under +1.2 V applied bias relative to OCV (~700 °C with 0.5 Torr of 1:1 H ₂ /H ₂ O mixtures).....	85
Figure 3-14. Interpretation of the potential losses across the gas-solid interface and CeO _{2-x} -YSZ interface showing the surface potential steps (χ) and the charge transfer overpotential (η).....	87
Figure 4-1. Schematic illustration of the electrochemical cell comprising a 300 nm Pt CE, a 300 nm Au current collector on top of a 30 nm Al ₂ O ₃ film (not shown) and 1000 nm CeO _{2-x} WE patterned onto a polycrystalline YSZ substrate.....	99
Figure 4-2. Schematic illustration of electro-chemical reactions on the specially designed single-sided SOC under positive and negative biases.....	100
Figure 4-3. Spatially-resolved XPS measurements of the C 1s obtained with a 2D area detector at 0, -1.5 and +2.0 V applied potentials (~600 °C with 0.5 Torr of 1:20 CO/CO ₂ mixtures).....	102
Figure 4-4. Integrated XPS spectra obtained by slicing a 60- μ m-wide segment from the corresponding photoelectron signal in Figure 4-3 at position of 0.0 mm.....	103

Figure 4-5. Integrated XPS spectra of the O 1s obtained at 0, -1.5 and +2.0 V applied biases at the cell position of 0.0 mm.....	104
Figure 4-6. Coverage changes of CO ₃ ²⁻ adsorbates away from OCV conditions derived from C 1s XPS spectra under -1.5 and +2.0 V applied bias (~600 °C with 0.5 Torr of 1:20 CO/CO ₂ mixtures).....	105
Figure 4-7. Coverage changes of CO ₃ ²⁻ adsorbates away from OCV conditions derived from O 1s XPS spectra under -1.5 and +2.0 V applied bias (~600 °C with 0.5 Torr of 1:20 CO/CO ₂ mixtures).....	106
Figure 4-8. Coverage of SiO ₂ on the CeO _{2-x} electrode surface under OCV, -1.5 V and +2.0 V (~600 °C with 0.5 Torr of 1:20 CO/CO ₂ mixtures).....	108
Figure 4-9. The relative concentrations of Ce ³⁺ measured <i>operando</i> at OCV, -1.5 and +2.0 V (~600 °C with 0.5 Torr of 1:20 CO/CO ₂ mixtures).....	110
Figure 4-10. Plot of cell current as a function of time under different applied biases (+1.5 V, -1.5 V, and +2.0 V).....	114
Figure 4-11. LSV polarization curves of SOC with 1000-nm-thick CeO _{2-x} film at ~600 °C with 0.5 Torr of 1:20 CO/CO ₂ mixture.....	114
Figure 5-1. Schematic illustrations of electrochemical reactions under bias conditions on the single-sided SOC composed of a 300 nm Pt CE, a 300 nm Au current collector on top of a 30 nm Al ₂ O ₃ film (not shown) and a 350 or 1000 nm CeO _{2-x} WE patterned onto the YSZ substrate.....	123
Figure 5-2. Coverages of graphitic carbon species extracted from C 1s under OCV, -1.5 and +2.0 V biases with 1:20 CO/CO ₂ gas mixtures at ~600 °C.....	125

Figure 5-3. The relative concentrations of Ce^{3+} measured *operando* under potentials of OCV, -1.5 V and +2.0 V with 1:20 CO/CO₂ mixtures at ~600 °C.....127

Figure 5-4. Plots of local surface potential calculated from the BE shifts in Si 2p photoelectrons relative to OCV conditions.....129

Figure 5-5. Plots of local surface potential extracted from the kinetic energy shifts in Pt 4f and Zr 3d photoelectrons relative to OCV condition.....131

List of Abbreviations

AFC	Alkaline fuel cell
AFM	Atomic force microscopy
ALS	Advanced Light Source
AP-XPS	Ambient pressure X-ray photoelectron spectroscopy
BE	Binding energy
CE	Counter electrode
DFT	Density functional theory
E	Nernst potential
EIS	Electrochemical impedance spectroscopy
EPOC	Electrochemical promotion of catalysis
ESCA	Electron spectroscopy for chemical analysis
EXAFS	Extended X-ray absorption fine structure
F	Faraday constant
FTIRES	Fourier transform infrared emission spectroscopy
GC	Gas chromatography
GDC	Gadolinium doped ceria
I	Current
IMFP	Inelastic mean free path
KE	Kinetic energy
LBNL	Lawrence Berkeley National Laboratory
LSCF	Lanthanum strontium cobalt ferrite

LSCM	Lanthanum strontium manganese chromite
LSGM	Lanthanum strontium gallate magnesite
LSM	Lanthanum strontium manganite
LSV	Linear sweep voltammetry
MCFC	Molten carbonate fuel cell
MIEC	Mixed-ionic-electronic-conducting
MS	Mass spectrometry
NASA	National Aeronautics and Space Administration
NEMCA	Non-Faradaic electrochemical modification of catalytic activity
NEXAFS	Near edge X-ray absorption fine structure
NIR	Near infrared
OCV	Open circuit voltage
PAFC	Phosphoric acid fuel cell
PEMFC	Polymer electrolyte membrane fuel cell
p_j	Partial pressure of species j
SEM	Scanning electron microscopy
SOC	Solid oxide electrochemical cell
SOEC	Solid oxide electrolysis cell
SOFC	Solid oxide fuel cell
STM	Scanning tunneling microscopy
T	Absolute temperature
TPB	Three-phase boundary

TWC	Three-way-catalyst
UHV	Ultrahigh vacuum
V_j	Local potential of species j
V_L	Local potential
V_O	Oxygen vacancy
WE	Working electrode
WGS	Water gas shift reaction
XAS	X-ray absorption spectroscopy
XPS	X-ray photoelectron spectroscopy
XRD	X-ray diffraction
YSZ	Yttria-stabilized zirconia
Z	Impedance
η	Overpotential
η_L	Local overpotential
ϕ	Work function
χ	Surface potential step
2D	Two-dimensional

Chapter 1

General Introduction

This dissertation presents the investigations of electrochemical reactions on solid oxide based electrochemical cells under operating conditions. *Operando* ambient pressure X-ray photoelectron spectroscopy (AP-XPS) is utilized to study the specially designed single-sided electrochemical cell and to extract detailed information of cell processes. These studies are inspired by the tremendous research interests in energy conversion devices such as batteries, fuel cells, and electrolyzers. Although much effort has been devoted to study these energy conversion devices to not only elucidate their fundamental properties but also to explore the practical industrial applications, the chemistry responsible for energy conversion and materials degradation in these devices is still not fully understood. This is mainly due to the lack of appropriate diagnostic techniques for direct observation of the chemistry processes at the places where and while they occur.

In this work the *operando* capability of AP-XPS is explored to study electrochemical reactions on a solid oxide based electrochemical cell. Simultaneous XPS and electrochemical measurements are collected on the solid oxide electrochemical cell (SOC). Mixed-ionic-electronic-conducting (MIEC) material of cerium oxide (CeO_{2-x}) is used as electrocatalyst due to its excellent catalytic properties. The SOC in this study has a planar cell geometry that places both the working electrode (WE) and the counter electrode (CE) on the same side of the solid oxide electrolyte for XPS measurements.

Through the use of *operando* AP-XPS, studies of water electrolysis and hydrogen electro-oxidation reactions on ceria electrocatalyst reveal fundamental properties of the electrochemical cell, including the local surface potential mapping and the detection of the electrochemically active region of the ceria electrocatalysts. The transient build-up of reaction intermediates allows for the determination of the rate-limiting charge transfer processes. A potential separation of the adsorbed OH⁻ species and lattice O²⁻ ions is observed at the gas-solid interface, which provides insights into the gas-solid interface chemistry.

Investigation into the carbon dioxide electrolysis and carbon monoxide electro-oxidation on ceria electrode also leads to knowledge of their surface kinetics and reaction mechanisms. Carbonates are identified as reaction intermediates in these electrochemical reactions. The steady-state concentration changes in CO₃²⁻ as electrochemistry occurs suggest the charge transfer process to/from CO₃²⁻ is a rate-limiting process. The electrochemically active region is found further extended by the graphitic carbon formed on the CeO_{2-x} electrode surfaces during CO₂ electrolysis. Measurements of overpotentials at the electrode-electrolyte interface reveal information about the charge transfer resistance at this interface in these environments. Details of the experimental approaches and results will be further given in this dissertation.

Although studies on these single-sided model electrochemical cells are not identical to those conducted on realistic fuel cells or electrolyzers, mechanistic information extracted from these investigations is still valuable and actually guiding to the development of fuel cells as their chemical processes are very similar.

This chapter gives a general introduction to fuel cells and XPS, with more specific introductions to solid oxide fuel cells (SOFCs) and the synchrotron radiation-based AP-XPS technique. The current knowledge of SOFCs and challenges in their further development are summarized to provide the technical background for this dissertation.

1.1 Fuel Cells

A fuel cell is an energy conversion device that produces electricity by electrochemically oxidizing a fuel and reducing an oxidant in separate compartments of a cell that are separated by an electrolyte. A fuel cell is similar to a battery in that they both convert chemical energy into electrical energy. However, a battery contains a fixed amount of energy within it and once this is used, the battery must be discarded or recharged by an external supply of electricity to drive the electrochemical reaction in the reverse direction. The fuel cell, on the other hand, uses an external supply of chemical energy and can run as long as it is supplied with a source of fuel and oxidant.

Fuel cells are currently attracting tremendous interest because of their huge potential for power generation in stationary, portable and transport applications.¹⁻³ These include primary power units, portable fuel cells for military application, small or large personal electronics, and power supplies for vehicles. Fuel cells have several benefits over conventional combustion-based power generation systems. They have higher energy conversion efficiency than combustion engines. Their high energy conversion efficiency comes from the fact that they convert chemical energy of the

fuel and oxidant directly into electrical energy without the intermediate formation of thermal energy, *i.e.*, the conversion efficiency is not subject to the Carnot limitation. Hydrogen fueled fuel cells are pollution free if the hydrogen comes from electrolysis of water driven by renewable energy. In addition, there are no moving parts in fuel cell stacks, making them more reliable and quieter than internal combustion engines.^{4,5}

The principle of fuel cell operation was first reported by William Grove in 1839.⁶ He used dilute sulfuric acid as the electrolyte and the fuel cell was operated at room temperature. **Figure 1-1** shows a schematic diagram of a generic fuel cell. It consists of two electrodes separated by an electronically insulating, but ionically conducting electrolyte.⁷ Fuel is fed to the anode, where it is oxidized, releasing electrons to the external circuit. Oxidant is reduced on the cathode, accepting electrons from the external circuit. Ions are carried from one electrode to the other, while the electrons flow through the external circuit producing electricity. The charge flow in the external circuit is balanced by ionic current flow within the electrolyte. Depending on the electrolyte material, the ions move from anode towards cathode or in the reverse direction.

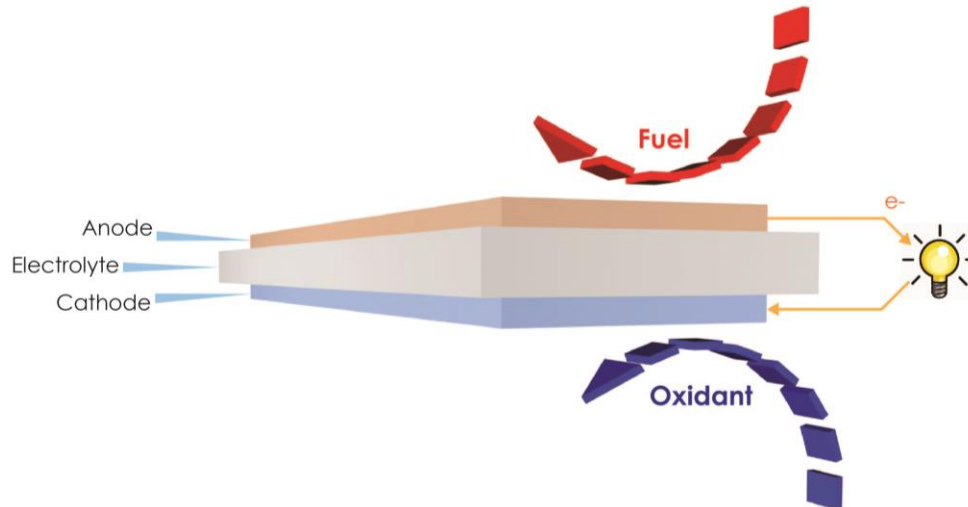


Figure 1-1. Schematic diagram of a generic fuel cell operation. Fuel oxidation on the anode and oxidant reduction on the cathode leads to generation of electricity flowing through the outer circuit.

Fuel cell types differ primarily in the type of electrolyte and mobile ion in the system. There are five main types of fuel cells that are under active development: alkaline fuel cells (AFCs), phosphoric acid fuel cells (PAFCs), polymer electrolyte membrane fuel cells (PEMFCs), molten carbonate fuel cells (MCFCs), and solid oxide fuel cells (SOFCs). **Figure 1-2**⁸ summarizes various fuel cell types and their typical operating characteristics.

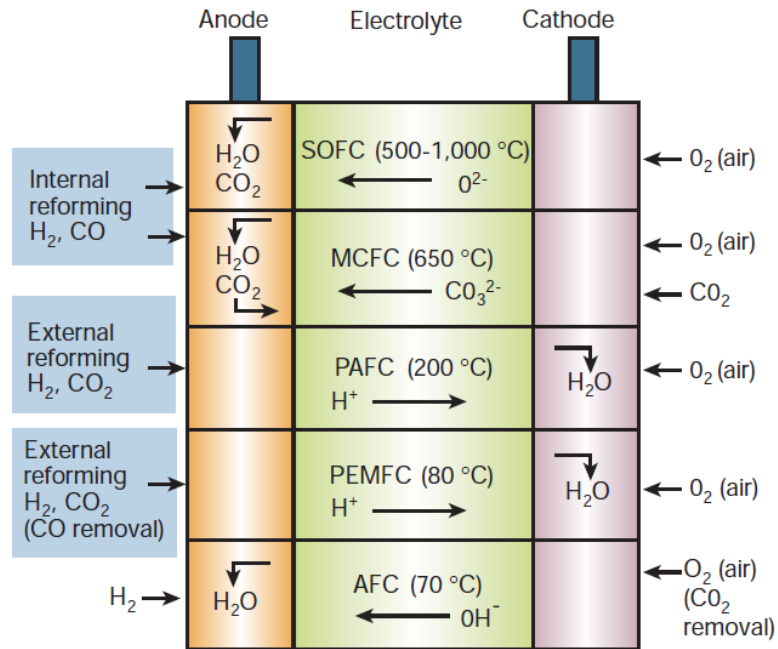


Figure 1-2. Summary of various fuel cell types.⁸ Reaction products are formed at the anode side for SOFC, MCFC, and AFC types, and at the cathode for PAFC and PEMFC types. The mobile ion and its direction of migration are indicated in the electrolyte region.

Each fuel cell type has its own operating characteristics, offering advantages to particular applications. As shown in **Figure 1-2**, AFCs, PEMFCs and PAFCs require pure H₂ supplied on the anode. Accordingly, if hydrocarbon fuels are used, an external reformer is needed to incorporate into the system, which increases the system complexity and the overall cost. In contrast, MCFCs and SOFCs operate at high temperatures and can accomplish fuel reforming within the stack. Moreover, CO and H₂ can be converted directly by electrochemical oxidation.

1.2 Solid Oxide Fuel Cells

Among the various types of fuel cells, SOFCs are currently attracting tremendous interest because of their high energy conversion efficiency, fuel

flexibility, high tolerance to impurities, and improved reaction kinetics.³ SOFCs have efficiencies of over 60% when converting fuel to electricity. If the heat produced is also harnessed, their overall efficiency in converting fuel to energy can be over 80%.^{1,4} Also, the direct electrochemical oxidation and internal reforming allowed by the high operating temperature environment of SOFCs are very attractive. Since all the cell components are solid, SOFCs can be configured into unique shapes and fabricated in very thin layers,^{1,4} which permits cell design with additional improvements.

1.2.1 Historical Background

The development of SOFC began with Nernst's discovery of solid oxide electrolytes in 1899.⁹ He reported that the conductivity of stabilized zirconium oxide (ZrO_2) increased with temperature: as an insulator at room temperature, stabilized- ZrO_2 starts to conduct ions between 600 °C and 1000 °C, and then becomes an electronic and ionic conductor at ~1500 °C.⁹ Since then, many mixed oxides exhibiting high conductivity at elevated temperatures were identified, including the most favorable Nernst mass¹⁰ composition of 85% ZrO_2 and 15% yttrium oxide (Y_2O_3).

In 1905, Haber filed the first patent on fuel cells with a solid electrolyte.⁴ In 1937, Baur and Preis operated a zirconia ceramic fuel cell for the first time at 1000 °C.¹¹ By using a tubular crucible made from stabilized zirconia as the electrolyte, the first SOFC stack of eight cells connected in series was made.¹¹

1.2.2 Operating Principles

Figure 1-3 shows a schematic diagram of the general operating principles of an SOFC. An SOFC unit consists of two porous electrodes separated by a dense, oxide-ion-conducting solid oxide electrolyte such as yttria-stabilized zirconia (YSZ). Fuels oxidized on the anode give up electrons to the external circuit while oxidants on the cathode side are reduced by incoming electrons from the external circuit. Between 600 and 1000 °C,^{1,2,8} the solid oxide electrolyte allows oxide ions transport through the ceramic body and the ionic current flow within the electrolyte is balanced by the charge flow in the external circuit.

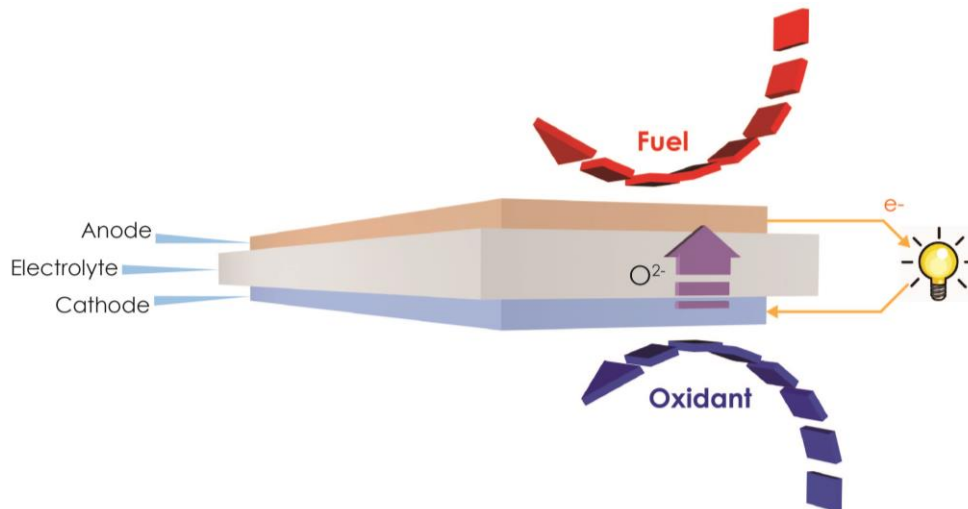


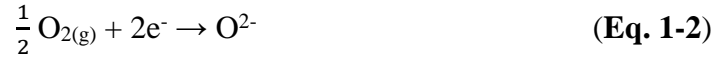
Figure 1-3. Schematic diagram of a solid oxide fuel cell (SOFC). In an SOFC, oxide ions move through the electrolyte from the cathode towards the anode.

1.2.3 Nernst Potential

In the case of H₂ fuel and O₂ oxidant, the oxidation reaction occurring on the anode produces H₂O:



On the cathode side, O_2 reacts with incoming electrons and O^{2-} ions are formed:



The O^{2-} ions migrate through the electrolyte and combine with H_2 on the anode side as depicted in **Figure 1-3**. Hence the overall reaction in an SOFC can be written as:



Under open circuit voltage (OCV), a voltage difference, the Nernst potential E , appears between the anode and the cathode. It is related to the net free energy change of **Eq. 1-3** via the following relation:

$$\Delta G = -nFE \quad (\text{Eq. 1-4})$$

where ΔG represents the net free energy change of the overall reaction, n the number of electrons participating in the reaction, F the Faraday constant.

The Nernst potential under non-standard states can be obtained by:

$$E = E^0 + \frac{RT}{2F} \ln \left(\frac{p_{O_2}^c p_{H_2}^a{}^2}{p_{H_2O}^a{}^2} \right) \quad (\text{Eq. 1-5})$$

where E^0 represents the Nernst potential under standard states, $p_{O_2}^c$ the partial pressure of oxygen in the cathode gas, $p_{H_2}^a$ and $p_{H_2O}^a$ the partial pressures of H_2 and H_2O in the anode gas, respectively, R the gas constant, and T the absolute temperature.

1.2.4 Polarization

Eq. 1-4 gives the maximum possible electrical work that can be derived from a fuel cell under given conditions of temperature and gas pressures. However, the voltage of an operating cell is always lower than the ideal value of OCV. Once the external load is connected, a finite, non-zero current is drawn from the fuel cell and

voltage losses exist, which are known as polarization losses or overpotentials (η). As shown in **Figure 1-4**, there are three dominant polarizations: a) activation polarization; b) ohmic polarization/loss; and c) concentration polarization.

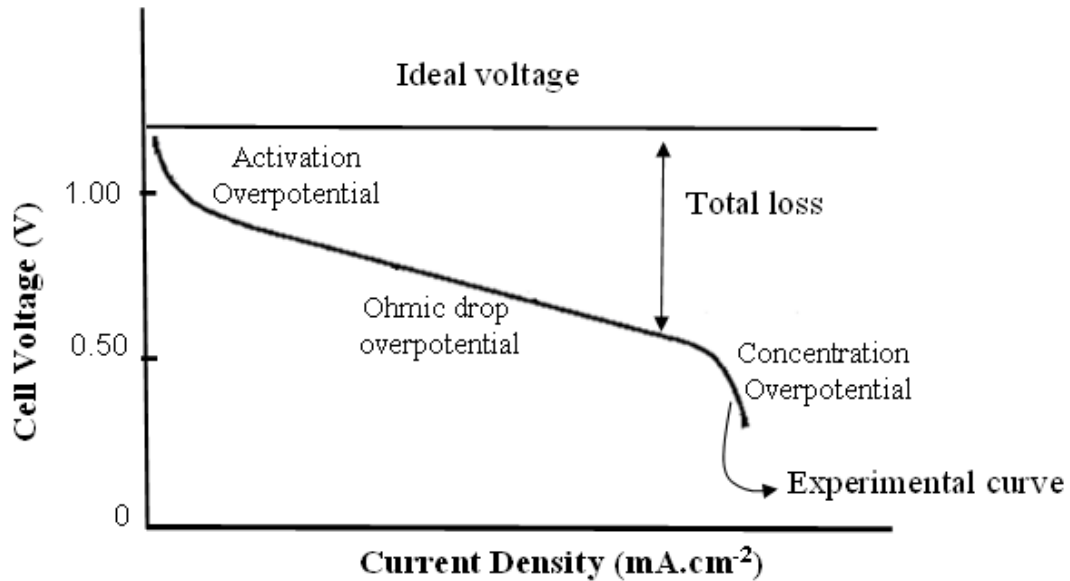


Figure 1-4. Typical fuel cell voltage-current characteristic at 800 °C with pure hydrogen as fuel.¹²

Activation polarization is the voltage drop due to the slowness of reactions occurring at the electrode-electrolyte interfaces. It is the voltage penalty paid for driving charge transfer reactions across the interface in the circuit. For example, at the cathode, electric energy is required to promote a charge transfer reaction for converting an oxygen molecule into an oxide ion. This activation polarization is related to the kinetics of the charge transfer processes and is governed not only by the electrocatalytic activity of the electrode but also by the microstructure of the electrode materials. Generally speaking, if the structure at the electrode-electrolyte interface is relatively fine the activation polarization is lower.

Ohmic polarization/loss stems from the bulk resistance of a material to electron and ion flows. In most SOFCs, the ionic resistance in the electrolyte presents the main contribution to ohmic polarization. The ionic resistivity of the electrolyte is much greater than electronic resistivity of the cathode and the anode.⁴

Concentration polarization is caused by the resistance to mass transport through the electrodes and interfaces. This voltage drop becomes large at high current densities because under such conditions gaseous species cannot diffuse fast enough through the porous interstices of electrodes, which results in the starvation of fuel or oxidant at the electrolyte-electrode interface. When low molecular weight H₂ is used on the anode, a low concentration polarization can be achieved due to the relatively rapid diffusion. Generally, coarse electrode structure with large amounts of porosity are preferred in minimizing concentration polarization.

1.2.5 SOFC Components

This section discusses the SOFC components: electrolyte, cathode, and anode materials and their characteristics.

1.2.5.1 Electrolytes

In an SOFC, the electrolyte is responsible for the conduction of ions between the electrodes, the separation of reacting gases into two compartments, and the push for electrons to flow through the external circuit by blocking the electronic conduction.⁴ Most of the high temperature fuel cells operate via oxygen ion conduction from the cathode (air feed) to the anode (fuel feed). This conduction happens by the presence of oxygen vacancies (V_O). The oxygen-ion conductivity is achieved by movement of O²⁻ via vacancies.

To achieve satisfactory performance, the electrolyte materials are required to show high oxide ion conductivity (greater than 10^{-2} S/cm at the operating temperature^{4,12}), negligible electronic conduction, high density, thermodynamic stability, and compatibility with other cell components. Stabilized zirconia, especially yttria stabilized zirconia (YSZ), has been the most investigated and developed electrolyte in SOFCs due to its adequate ionic conductivity above 800 °C, the low electronic conductivity, the desired stability under reducing and oxidizing atmospheres, and the low cost of starting materials and fabrication.^{1,2,7,13}

ZrO₂ exhibits monoclinic crystal structure at room temperature, changing to tetragonal above 1170 °C, and to cubic fluorite structure above 2370 °C.¹ The addition of an aliovalent (*i.e.*, divalent or trivalent) dopant such as yttrium oxide stabilizes the cubic fluorite structure of zirconia, and increases its oxygen vacancy concentration by charge compensation. Since the oxide ion mobility in stabilized zirconia is achieved by movement of oxide ions via oxygen vacancies, the increased oxygen vacancy concentration leads to an enhanced oxygen ion conduction.

Figure 1-5 shows the change of conductivity with dopant concentration for various doped zirconias.¹⁴ The conductivity depends on the dopant concentration. Although stabilization of ZrO₂ with Y₂O₃ does not yield the highest conductivity, YSZ is still the most frequently used SOFC electrolyte because of the sufficient ion conductivity, high stability under both oxidizing and reducing environments, and the low cost.

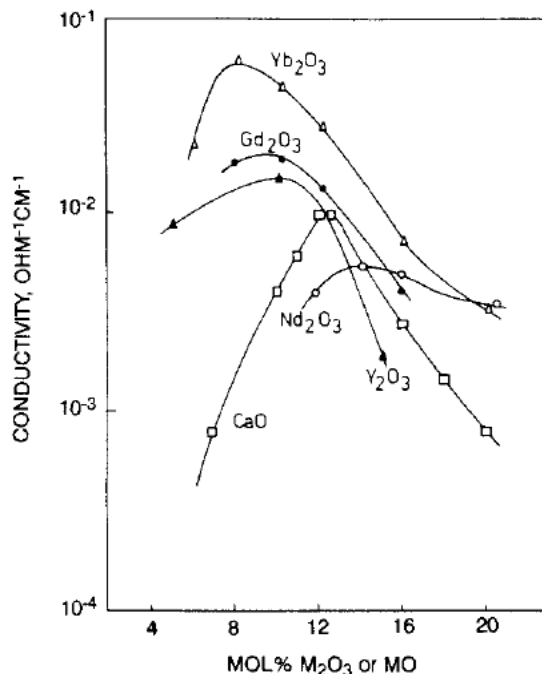


Figure 1-5. Variation of ionic conductivity of stabilized zirconia with dopant concentration ($T = 807\text{ }^{\circ}\text{C}$).¹⁴

Other fluorite structured oxide ion conductors, such as doped cerium oxide, have also been proposed as electrolyte materials for SOFCs.^{7,13} When compared to stabilized zirconia, doped ceria presents ionic conductivities approximately one order of magnitude greater under similar temperature conditions. This enhancement is due to the larger ionic radius of Ce^{4+} (0.87 \AA) versus Zr^{4+} (0.72 \AA), which produces the more open structure of doped ceria.¹⁵ Gadolinium (Gd^{3+}) is the most commonly used doping cations while Sm^{3+} and Y^{3+} are often studied as well. With the smallest ionic radius mismatch between Gd^{3+} and Ce^{4+} , gadolinium doped ceria (GDC) exhibits the lowest activation energy for O^{2-} ion conduction, *i.e.*, the highest ionic conductivity.⁵ However, the partial reduction of Ce^{4+} to Ce^{3+} at elevated temperatures in a reducing atmosphere leads to electronic conductivity, which reduces the open circuit voltage and consequently lowers the efficiency of SOFCs.

Perovskite materials, such as lanthanum gallate (LaGaO_3) and $\text{La}_{1-x}\text{Sr}_x\text{Ga}_{1-y}\text{Mg}_y\text{O}_{3-\delta}$ (LSGM), have also been found to possess good ionic conductivity.^{7,13} Perovskite-type oxides have the general formula of ABO_3 . **Figure 1-6**¹⁶ shows the perovskite structure in which A and B are cations with an overall charge of +6. The A cations (such as La, Sr, Ca, and Pb) have lower valences. They are larger in size and are coordinated to twelve oxygen anions. The B sites (such as Ti, Cr, Ni, Fe, Co, and Zr) occupy a smaller space and are octahedrally coordinated to six oxygens.⁴ The increased ionic conductivity of perovskite materials is obtained from the substitution of the trivalent cations with divalent cations.

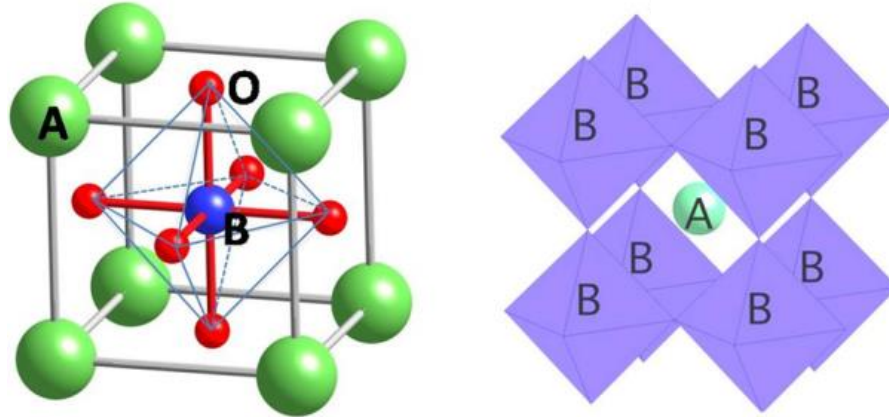


Figure 1-6. Schematic representation of lattice structure of perovskite, ABO_3 .¹⁶

Several doped perovskite materials have been identified as potential candidates for SOFC electrolytes. LaGaO_3 has attracted considerable attention in recent years. The substitution of La and Ga by Sr and Mg, respectively, gives the favored composition of $\text{La}_{0.9}\text{Sr}_{0.1}\text{Ga}_{0.8}\text{Mg}_{0.2}\text{O}_{2.85}$, which shows higher ionic conductivity than YSZ.⁸ However, these materials are unstable under reducing

environment, which poses potential problems for the long term durability of LSGM as an SOFC electrolyte.

1.2.5.2 Cathodes

The cathode is where the electrochemical reduction of the oxidant (mostly oxygen) occurs. As such, cathode materials of SOFCs require properties of high catalytic activity for oxygen reduction, high electrical conductivity, chemical and microstructure stability under an oxidizing atmospheres, and chemical compatibility with other cell components under operating conditions. Unlike the electrolyte, the electrodes must have a porous structure (approximately 30 - 40% porosity)¹² to optimize access to O₂ gas molecules.

The use of noble metals, such as platinum, palladium, or silver, as SOFC cathode materials is not practical due to the prohibitive costs of these elements. Since the 1960s doped lanthanum cobaltites and lanthanum manganites perovskite materials have been recognized as the most prominent candidates for SOFC cathode materials.¹⁷

LaMnO₃ possesses the perovskite structure with intrinsic p-type conductivity. Dopants with divalent cations (such as Mg²⁺, Ca²⁺, Sr²⁺, and Ba²⁺) substitute for La³⁺ and increases the content of Mn⁴⁺. The increased electron-hole concentration, therefore, improves the electrical conductivity of the electrode material. Typically, the composition of La_{0.8}Sr_{0.2}MnO₃ (LSM) gives a good combination of electronic conductivity and expansion coefficient matching⁴, and is now the most commonly used cathode material for high temperature SOFCs. The normal practice is to mix the LSM powder with YSZ powder, in roughly 1:1 ratio, to form the first layer of the

cathode material at the electrolyte surface. Since most of the electrochemical reactions occur at the three-phase boundary (TPB), where the gas phase meets the electrode and the electrolyte phase, the practice of mixing LSM and YSZ leads to a broadened TPB (*i.e.*, broadened active region). Also, it improves the thermal match of the cathode with the YSZ electrolyte, and leads to improved porosity.

Mn substitutions by Co or Fe on the B sites of a perovskite give promising cathode materials of $\text{La}_{1-x}\text{Sr}_x\text{Fe}_{1-y}\text{Co}_y\text{O}_{3-\delta}$ (LSCF). They exhibit high electronic and ionic conductivities and excellent catalytic activity for oxygen reduction.¹² However, La and Sr containing cathodes react with YSZ at elevated temperature and produce insulating phases such as $\text{La}_2\text{Zr}_2\text{O}_7$ and SrZrO_3 at the electrode-electrolyte interface.

1.2.5.3 Anodes

The anode provides reaction sites for the electrochemical oxidation of the fuel gas. Similar to the cathode, the anode must have high catalytic activity, electrical conductivity, porosity (20 - 40%), and chemical compatibility with the adjoining component.^{1,4,12} Stability under the reducing operating conditions is required as well.

A) Nickel/Yttria-Zirconia Cermets

Nickel metal is a very commonly used anode material for SOFCs due to its relatively low cost and the high catalytic activity of Ni to break the H-H bond.^{1,4,8}

Figure 1-7 shows a schematic drawing of the TPB (red solid line) in an SOFC with a metal anode. However, Ni aggregation at elevated temperatures inhibits the access of the fuel. This problem can be solved by mixing YSZ electrolyte powders with the Ni matrix to form a composite anode.⁴ Generally, the Ni/YSZ cermet is prepared by mixing NiO and YSZ powders in a slurry. The paste is then applied to the solid

electrolyte and fired in air at ~ 1300 °C. When the prepared electrode is exposed to the fuel, the active anode is formed by reducing the NiO to Ni metal *in situ*.⁴ In the Ni/YSZ cermet, the Ni metal particles are supported by the YSZ structure and, therefore, the coarsening of Ni at elevated temperatures becomes inhibited and the TPB length is optimized.

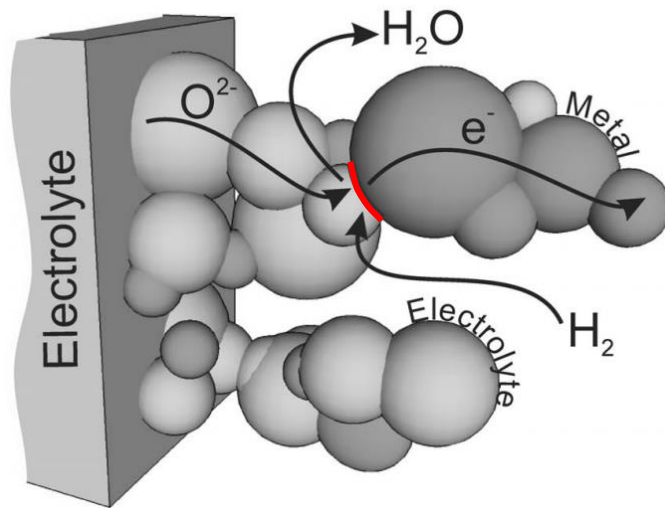


Figure 1-7. A schematic drawing of the triple phase boundary (red solid line) in the anode region of a solid oxide fuel cell.¹⁸

In a Ni/YSZ cermet, the electronic conduction path through the metallic Ni phase is accompanied by an ionic conduction path through the YSZ phase, which is facilitated by the presence of YSZ. It is found that the conductivity of Ni/YSZ cermets depend on the Ni concentrations. For example, the conductivity is predominantly ionic when the Ni concentration is below 30% in volume; whereas above 30% in volume, it is predominantly electronic.^{1,4,19} **Figure 1-8**¹⁹ shows the conductivity of the Ni/YSZ cermets as a function of Ni content.

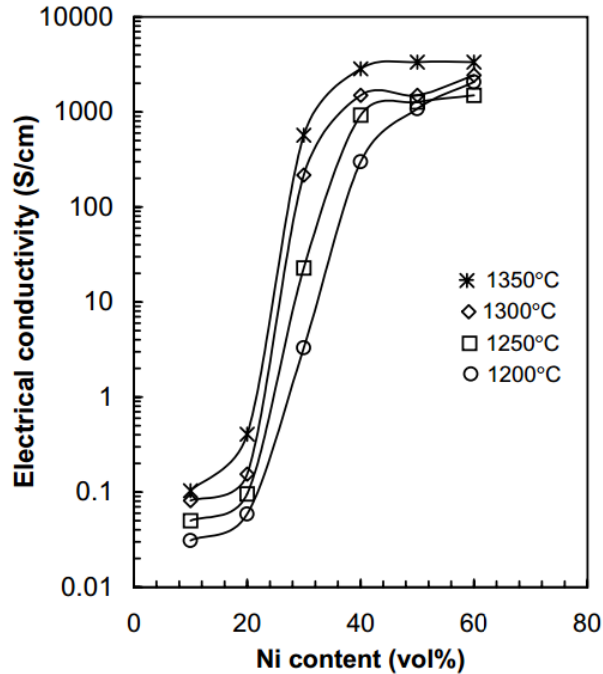


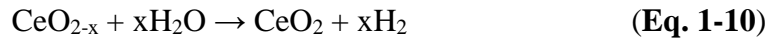
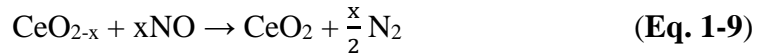
Figure 1-8. Electrical conductivity measured at 1000 °C as a function of Ni content of Ni/YSZ cermet fired at different temperatures from 1200 to 1350 °C.¹⁹

Ni/YSZ cermet anodes have been shown to provide adequate performance under certain conditions but do exhibit problems such as coking with hydrocarbon fuels.^{3,4,20} The carbon layer formed on the electrode surface can disrupt the electrode by physically separating the Ni particles from the electrode surface. Also, the barrier layer prevents access of gas reactions to the electrode. Therefore, Ni/YSZ composite electrodes are not an ideal choice for SOFCs intended to use ethanol, methanol, gasoline or natural gas as fuels.

B) Cerium Oxide Based Materials

Cerium oxide and its doped relatives have been investigated as alternative materials for SOFC anodes since 1964²¹ due to their redox stability, high resistance to coking, and potential higher activity than metal catalysts.²²⁻²⁷ Ceria is a technologically important material with many interesting catalytic properties. Its

ability to convert and remove the poisonous CO to CO₂ via the water gas shift (WGS) reaction in the presence of water (CO + H₂O → CO₂ + H₂) has been attracting a great deal of interest.^{28–30} This reaction is also critical in the production of hydrogen. Ceria is known to have good oxygen storage capacity and it has been used widely in three-way-catalyst (TWC) for automobile exhaust gas treatment since early 1990s.³¹ The main role of ceria in TWC is to provide oxygen buffering capacity during the oscillation of exhaust gases (deficient O₂ and excess O₂).³¹ During the oxygen deficient portion of the cycle, ceria donates its oxygen for the oxidation of CO and hydrocarbons (HC) (**Eq. 1-6**, **Eq. 1-7**, and **Eq. 1-8**). While in the oxygen excess cycle, ceria adsorbs and store oxygen from oxidant of NO, H₂O and O₂ (**Eq. 1-9**, **Eq. 1-10**, and **Eq. 1-11**).^{31,32}



Pure stoichiometric CeO₂ has the cubic fluorite structure (**Figure 1-9**) with space group Fm $\bar{3}$ m from room temperature to the melting point (*i.e.*, 2750 K).²¹ As mentioned above, ceria can tolerate considerable reduction without a phase change. When CeO₂ is reduced to CeO_{2-x}, Ce⁴⁺ is converted to Ce³⁺, which is accompanied by the formation of oxide ion vacancies (V_O). The process of ceria reduction can be written as:

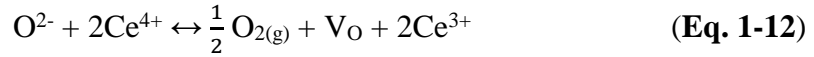


Figure 1-10²¹ shows the oxygen deficiency (in CeO_{2-x}) as a function of the oxygen equilibrium pressure and temperature.

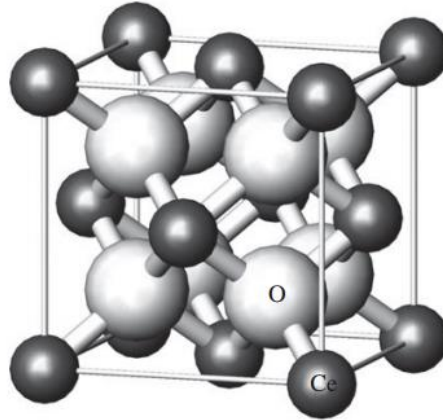


Figure 1-9. Crystal structure of cerium oxide.³³

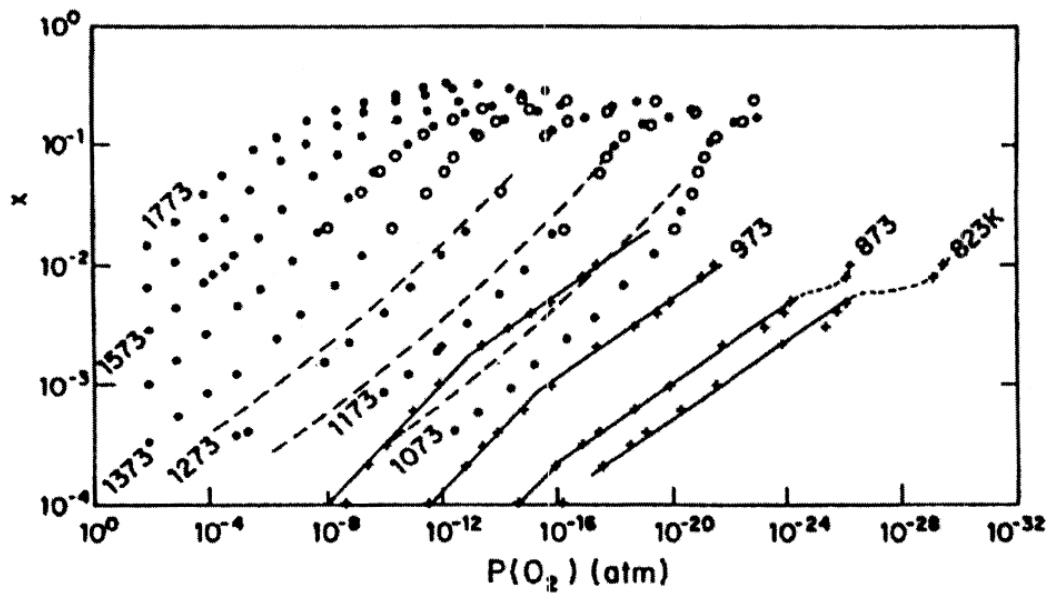


Figure 1-10. Oxygen deficiency x in CeO_{2-x} as a function of oxygen equilibrium pressure and temperature.²¹

CeO_{2-x} between 200 °C and 1300 °C is an n-type semiconductor.^{21,34} It is generally agreed that the n-type conductivity takes place by small polaron

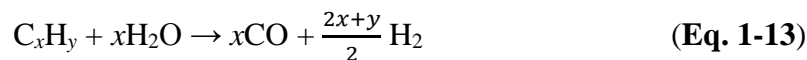
conduction.^{15,35} A polaron (*i.e.*, an e^- or a hole) is a defect created when an electronic carrier becomes trapped at a given site as a consequence of the displacement of adjacent atoms or ions.¹⁵ The small polaron conduction takes place by a hopping motion of the entire defect, *i.e.*, the electron (or electron hole) and distortion.^{15,21} This is the so-called “polaron hopping mechanism”. The small polaron in CeO_{2-x} can be identified as Ce^{3+} . Electrical conductivity measurements of single crystal ceria and polycrystalline samples suggest that the grain boundaries do not form many barrier to the electron migration.^{21,36}

Ceria is a mixed-ionic-electronic conductive (MIEC) material. Its ionic conduction is achieved by hopping the oxide ions to vacant sites. It has been found that the total ionic conductivity consists of contributions from both the bulk of the grains and the grain boundaries.²¹ The grain boundary is often very badly conducting and these two contributions are in series. Unlike cermet electrodes, where ionic conductivity and electron conductivity occur in separate materials, the MIEC behavior of CeO_{2-x} allows for the extension of electrochemically active region over the entire anode-gas interfacial area.^{4,21,31} This extension of the active region can lead to a significant drop in the activation barrier and an improvement in electrical efficiency.

1.2.6 Internal Reforming

One of the advantages of SOFC system is the flexibility in fuel choices. Methane, natural gas and hydrocarbons can be readily converted upon direct introduction by a reforming reaction on the anode.^{1,4} As such, a wide range of practical hydrocarbon fuels can be used without an external fuel reformer, which not

only decreases the costs but also simplifies the fuel cell set-up. The steam reforming process involves the catalytic conversion of hydrocarbon fuels to carbon monoxide and hydrogen:



The CO and H₂ are then electrochemically oxidized to CO₂ and H₂O on the anode. Compared with lower temperature fuel cells, internal reforming SOFCs offer significantly higher system efficiencies and reduced complexity. Together with the increased tolerance to impurities in the fuel, *e.g.*, sulfur, SOFCs represent significant advantages.

Each reaction process described in **Eq. 1-1**, **Eq. 1-2**, and **Eq. 1-13** involves a series of bulk and surface processes, including gas diffusion to the electrode surface, adsorption and dissociation of gas reactants on the electrode surface, and charge transfer across the electrode-electrolyte interface. So far, insights into these electrochemical processes are largely obtained from electrochemical measurements such as voltammetry and electrochemical impedance spectroscopy, which provides macroscopic thermodynamic and kinetic information. However, special experimental designs and complicated analysis are required to isolate and study individual electrochemical processes through these methods. This limitation hinders the development and validation of microscopic and molecular theories,³⁷ and constrains the rational design of next generation SOFCs. To obtain a thorough understanding of surface chemistry and charge transfer reaction processes of electrochemical devices *in situ* and *operando* characterization tools are required for observing the related physical and chemical processes directly at the places where and while they occur.

Since *ex situ* and electrochemical bulk measurements cannot provide direct or specific information for surface reaction kinetics or electrochemical active species, this dissertation is intended to demonstrate the capabilities of *operando* AP-XPS in explicitly unraveling the complex surface chemistry that are associated with high temperature solid oxide electrochemical devices. Next section is giving an introduction to XPS as well as the synchrotron radiation based AP-XPS technique.

1.3 X-ray Photoelectron Spectroscopy

1.3.1 Historic Background

X-ray Photoelectron Spectroscopy (XPS) originates from the discovery of the photo-electric effect by Einstein in 1905.³⁸ After World War II, Steinhardt and Serfass conceived the idea of developing XPS as an analytical tool for studying surface chemical phenomena.³⁸ The first X-ray photo-electron spectrum from cleaved sodium chloride was obtained by Kai Siegbahn and his research group in 1954. From the spectrum peak maximum (kinetic energy values), the electron binding energy could be determined accurately and the goal of using XPS for atomic structure investigation had been realized. Subsequently, Siegbahn's group observed the chemical shift effect on core-level binding energies. To underline that both photo and Auger electron peaks appear in the XPS spectrum the acronym of ESCA (electron spectroscopy for chemical analysis) had been used for a while.³⁸

1.3.2 Surface Analysis by X-ray Photoelectron Spectroscopy

When an atom or molecule absorbs an X-ray photon, an electron can be ejected (**Figure 1-11**). The kinetic energy (KE) of the emitted photo-electrons depends on the energy of incident X-ray ($h\nu$) and the electron binding energy (BE) as described by the basic equation of XPS:

$$KE = h\nu - BE \quad (\text{Eq. 1-14})$$

where the BE represents the energy required to remove the electron from the surface, and, therefore, is characteristic of the specific atom and specific orbital.

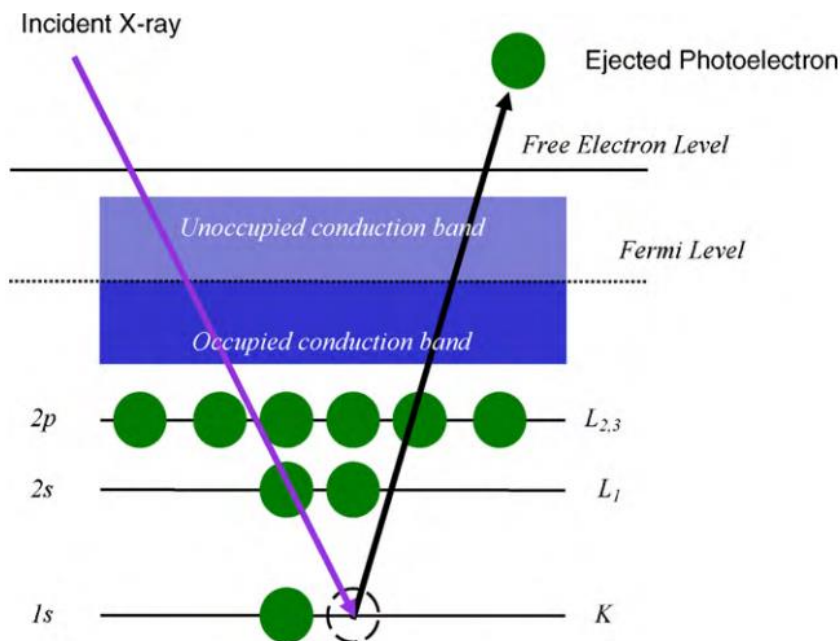


Figure 1-11. A schematic view of the photoemission process.³⁹ An incident X-ray photon is absorbed and a photoelectron is emitted. Measurement of the kinetic energy of the photo-emitted electron allows for the determination of the binding energy of the ionized electron.

As described in **Eq. 1-14**, by measuring the KE of the emitted electrons using an energy analyzer, one can determine the elements present (except hydrogen and helium) and their chemical and electronic states. **Figure 1-12** depicts a representative

wide scan XPS spectrum of platinum spontaneously deposited on rhodium.³⁹ A series of peaks are observed including Pt 4f, Rh 3d, Rh 3p, and Rh 3s peaks. Since the BE value is strongly related to the chemical environment of the atom from which the electron is emitted, XPS is able to measure specific local chemical and electrical environments of adsorbed species.^{38,40}

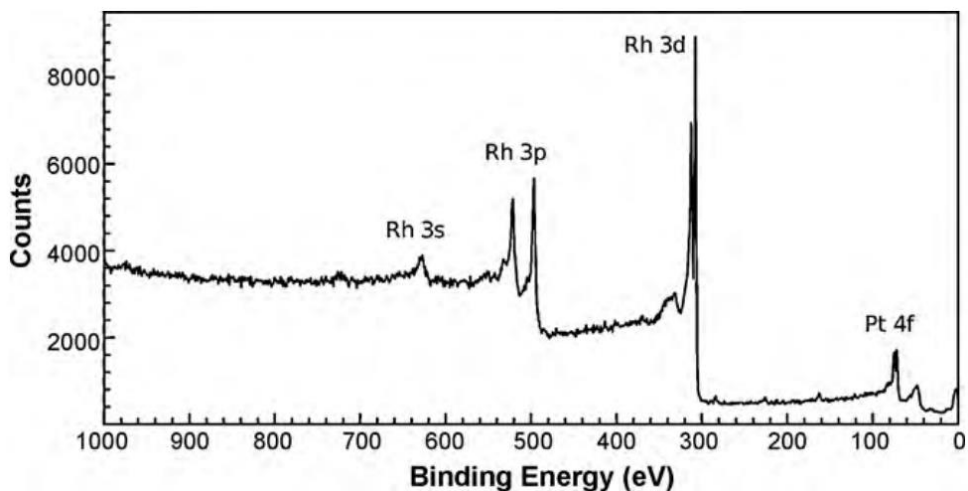


Figure 1-12. A representative wide-range XPS scan of platinum spontaneously deposited on rhodium.³⁹

In reality, the determination of the KE is more complicated than the case described in **Eq. 1-14** because the work function (ϕ) of the analyzer (and the sample) has to be taken into account. The work function is defined as the minimum energy needed to remove an electron from a solid surface to vacuum. **Figure 1-13** shows the energy level diagram of an atom in the solid state.⁴¹ The KE of the sample (KE_{samp}) measured through an electron energy analyzer is referenced to the vacuum level of the analyzer whereas the BE of the sample (BE_{samp}) is referenced to the Fermi level of the sample, **Eq. 1-14** becomes:

$$KE_{\text{samp}} = h\nu - BE_{\text{samp}} - \phi_{\text{ana}} \quad (\text{Eq. 1-15})$$

where ϕ_{ana} is the work function of the electron energy analyzer.

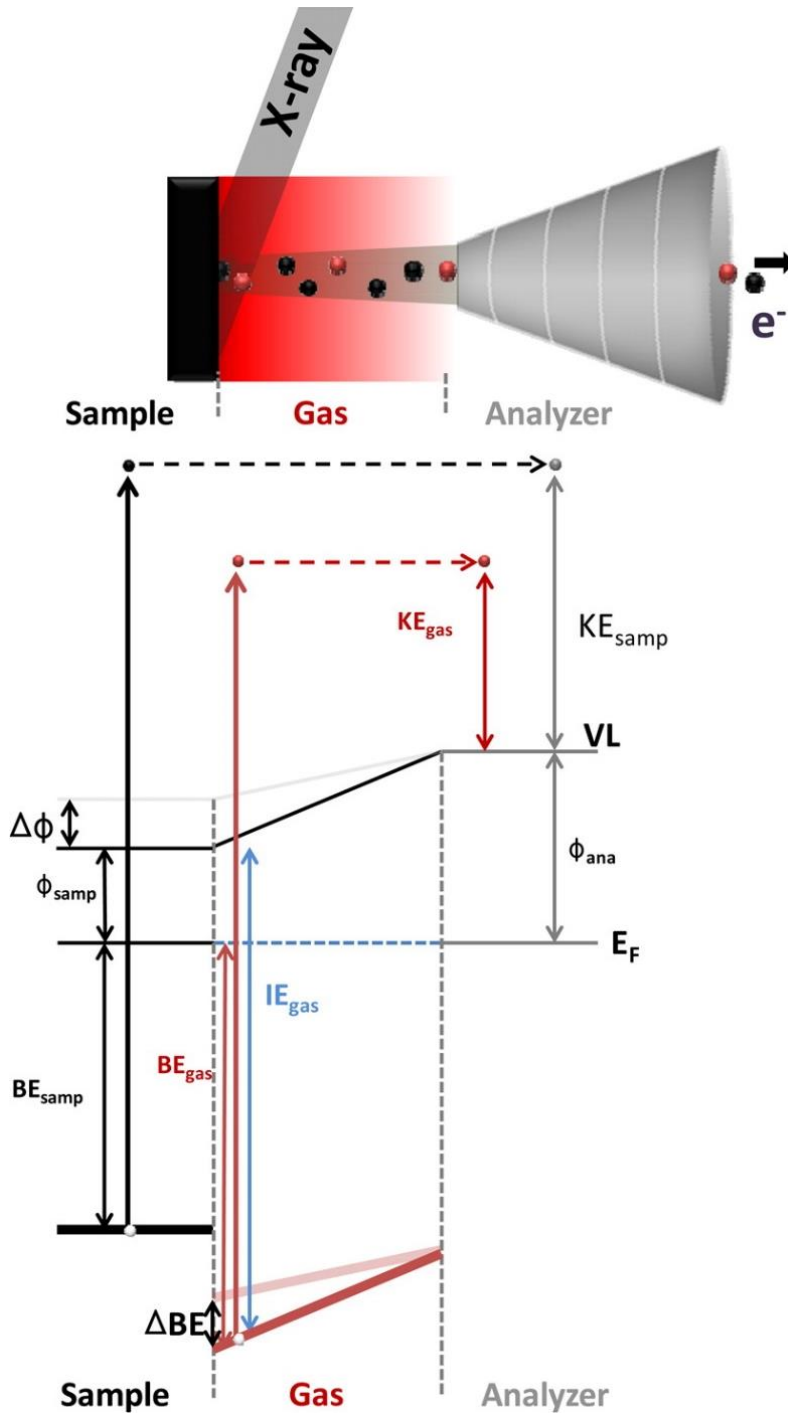


Figure 1-13. The schematic drawing of the energy level diagram of core level photoelectron spectroscopy.⁴¹ KE is the kinetic energy of the photo-emitted electron, VL the vacuum level, ϕ the work function, E_F the Fermi level, BE the electron binding energy of and IE the ionization energy.

In the routine analysis of XPS, the complications suggested in **Eq. 1-15** are eliminated through calibration with standards. Essentially:

$$KE' = h\nu - BE \quad (\text{Eq. 1-16})$$

where KE' is the kinetic energy value after calibration with the work function of the analyzer. Assumptions involved in **Eq. 1-16** are that the Fermi levels of the sample surface and the analyzer are equilibrated, the relaxation energy is a constant for an element, and that the analyzer work function is a constant. If the sample is charged due to the ejection of photoelectrons, or it is intentionally biased, the Fermi levels of the sample and the analyzer may not be in equilibrium. Thus:

$$KE' = h\nu - BE - \psi \quad (\text{Eq. 1-17})$$

where ψ represents the local electric environment.

In practical XPS measurements, the BE calibration is simplified by using the C 1s peak in the spectrum. Any sample that has been exposed to the ambient atmosphere forms surface contaminants of adventitious carbon, of which the binding energy is assigned 284.8 eV.⁴² This referencing approach is valid because the referencing point only affects the absolute BE values. The BE difference of any two XPS peaks and the relative chemical shifts of a certain XPS peak are not affected by this choice of zero point. Since surface potentials influence all of the electrons uniformly, calibration using the C 1s XPS peak for charged samples is also valid.

This rationale is applied to the XPS measurements discussed in this dissertation. Since only the energy *difference* between different XPS peaks and the relative shifts between biased and non-biased condition of certain peaks are of the primary interest, the absolute BE values can be obtained through the use of references

(*i.e.*, Au). Generally, the BE values here are ~ 2 eV less than those found in most literature reports, which are typically referenced to the Fermi level. More detailed discussions of referencing and standards are given in Chapter 2 and Chapter 3.

Although photons can penetrate several microns into the solid samples, photoelectrons that are created deep within the material have a great probability of being scattered before they escape and are detected by the spectrometer.³⁸ The distance an electron can travel through a solid before losing energy is defined as the inelastic mean free path (IMFP). This important parameter determines the probing depth of XPS. **Figure 1-14**³⁹ displays the experimental mean free path of electrons as a function of the kinetic energy. Surface sensitivity of XPS stems from the small IMFP values of electrons. The useful photoemission signal comes from the first few atomic layers of the material.^{38,43} **Figure 1-14** indicates that the mean free path of electron is not strongly dependent on materials, but on the electron kinetic energy. Therefore, surface sensitivity can be further achieved by conducting XPS measurements with the KE of electrons in the range of 50 - 100 eV. The surface sensitivity of XPS results in the requirement that the sample surface to be clean and free of contaminations.

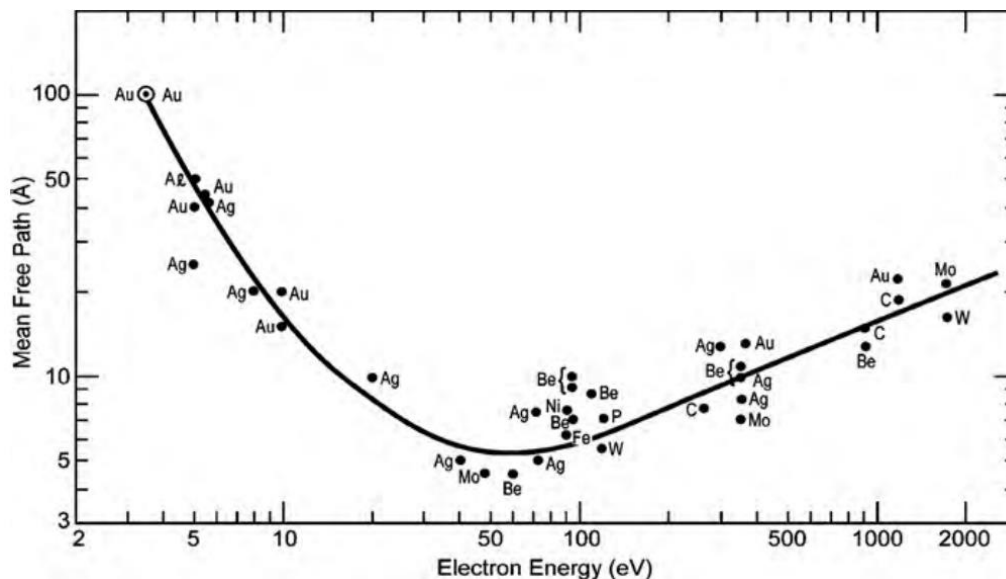


Figure 1-14. Mean free path of electron in solid as a function of electron kinetic energy.³⁹

As the electrons emitted by the sample travel through the gas phase they experience elastic and inelastic collisions with gas molecules. For electrons of 400 eV kinetic energy the IMFP is ~4 mm when the pressure is 1 mbar. This value decreases to ~30 μm at 100 mbar since it is inversely proportional to pressure.^{44,45} As such, conventional XPS is normally limited to ultrahigh vacuum (UHV) ($<10^{-8}$ Torr) conditions to avoid the elastic and inelastic scattering of the emitted photoelectrons by gas molecules.

1.3.3 Synchrotron Radiation Sources

The most typical laboratory-scale X-ray sources are aluminum $K\alpha$ X-rays and magnesium $K\alpha$ X-rays. X-rays are produced by bombarding a metal target (*e.g.*, Al and Mg) in an X-ray tube with high speed electrons which have been accelerated by 10 - 100 kV of potential.³⁸ The bombarding electrons eject electrons from the inner shells of the atoms of the metal target. Those vacancies are quickly filled by electrons

dropping down from higher atomic energy levels, emitting X-rays with defined frequencies associated with the difference between the atomic energy levels of the target atoms. The X-rays produced by transitions from atomic level of $n = 2$ to $n = 1$ are called $K\alpha$ X-rays, and those for $n = 3$ to $n = 1$ transition are called $K\beta$ X-rays.³⁸

Synchrotron radiation is another source of photons for photo-electron spectroscopy. It is well known that when charged particles are accelerated radially, synchrotron radiation is emitted. Since the discovery of synchrotron radiation in 1947^{46,47}, synchrotron light has been recognized as an ideal tool for various types of research and industrial applications due to its unique properties of high brilliance, high level of polarization, wide tunability in wavelength (*i.e.*, energy), and pulsed light emission. In the first generation, the synchrotron radiation was generated by using bending electromagnets in the accelerators. In 1968 the first storage ring was built as synchrotron light source (the second generation).⁴⁷ As the accelerator synchrotron radiation became more intense and the applications more promising, insertion devices (*e.g.*, undulators and wigglers) were employed to enhance the intensity of synchrotron radiation. The third generation synchrotron radiation sources are designed to produce brilliant X-rays and are typically heavily based on these insertion devices.⁴⁷ Currently, the major applications of synchrotron light are in condensed matter physics, materials science, biology and medicine.

Typically, a synchrotron radiation source has a radius of many meters and the electron beam has an energy of several GeV and current up to 1 A. **Figure 1-15** displays a scheme of the Advanced Light Source (ALS) at Lawrence Berkeley National Laboratory (LBNL) as an example of a synchrotron source. The ALS

complex consists of four main parts: an electron source, a short linear accelerator, the booster ring, and the main storage ring. Electrons are produced in the electron gun by heating up a tungsten grid. They are then accelerated in the linear accelerator (linac) and transferred to the booster ring. In the booster, they are accelerated to their final energy (1.9 GeV). After that, they are injected into the main storage ring where they circulate for many hours producing synchrotron radiation. Finally, the synchrotron radiation is captured by beamlines, which may originate at bending magnets or insertion devices. Designs of the beamlines vary with the applications. At the end of the beamline is the experimental endstation, where samples are positioned in the line of the radiation, and measurements are obtained.

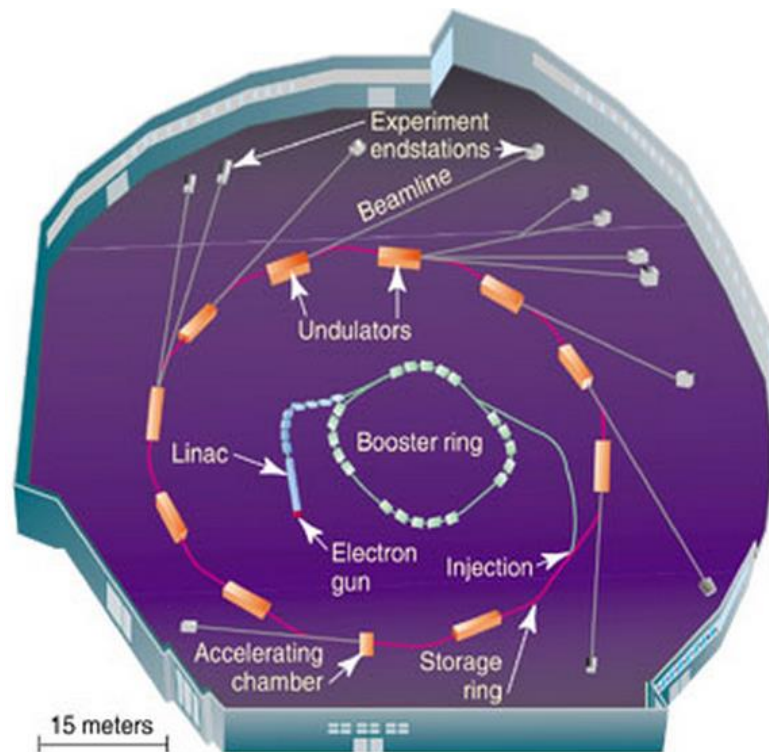


Figure 1-15. A scheme of the Advanced Light Source (ALS) at Lawrence Berkeley National Laboratory (LBNL). The synchrotron radiation source at ALS consists of four main parts: an electron source, a short linear accelerator, the booster ring, and the main storage ring.

Since synchrotron radiation produces a continuous spectrum of photons with energies from a few electronvolts to several kiloelectronvolts,⁴⁸⁻⁵⁰ the tunability of the photon energy allows for depth dependent chemical analysis of samples and maximizing the photoionization cross-section of elements of interest. In addition, by changing the photon energy of the incident X-ray beam, X-ray absorption spectroscopy (XAS) measurements can be performed using the electron analyzer as a partial yield detector. The high photon flux also significantly reduces the data acquisition time.

1.3.4 Ambient Pressure X-ray Photoelectron Spectroscopy

As mentioned in the Section 1.3.2 that conventional XPS is limited to UHV conditions due to the small electron mean free path, there is a fundamental question whether the information obtained under UHV can be used to describe the realistic situations at ambient pressure conditions. To close this “pressure gap”, Hans and Kai Siegbahn made the first attempt and successfully realized AP-XPS in 1970s.⁵¹⁻⁵³ Due to the short IMFP of electrons (see Section 1.3.2), they minimized the path length of the photo-emitted electrons through gas environment by placing the sample surface close to the differentially pumped aperture. This procedure has now become a general approach in all high-pressure XPS instruments.^{54,55} After four decades of development, AP-XPS has come to the stage of commercially available AP-XPS analyzers with synchrotron-based or lab-based X-ray sources. Differentially pumped electrostatic lenses are used in most of these analyzers.

The AP-XPS end-stations of 9.3.2 and 11.0.2 at ALS feature a high-brightness third-generation synchrotron source coupled with a differentially pumped electrostatic lens system.⁵⁶ **Figure 1-16** shows a schematic drawing of the AP-XPS endstation following the ALS architecture. The differentially-pumped electrostatic lens system separates the ambient pressure chamber from the hemispherical electron analyzer, therefore, allows for XPS measurements in the presence of reactive gases while maintaining the high-vacuum condition for photoelectron detection. **Figure 1-17** shows the principle of the differentially pumped electrostatic lens system. The sample is mounted in a high pressure chamber close to the differentially pumped aperture (**Figure 1-17 (a)**). The X-ray source is kept under vacuum by the use of X-ray transparent windows, such as silicon nitride, aluminum, or polymer membranes of 50 or 100 nm.⁴⁴ In the differentially pumped electrostatic lens system (**Figure 1-17 (c)**), the electrons are refocused onto the apertures between the differential pumping stages, which increases the transmission of electrons through the stages and allows for reduced aperture sizes for improved differential pumping. The radius of the aperture between the analysis chamber and the first pumping section is the key parameter and typically in the range of 0.1 - 1.0 mm (**Figure 1-18**). The size of the first aperture determines the minimum distance between the sample and aperture, which in turn determines the upper pressure limit in the experiment. Due to the high brilliance of third generation synchrotrons, the X-rays can be tightly focused and thus a smaller first aperture diameter and higher pressures can be used.

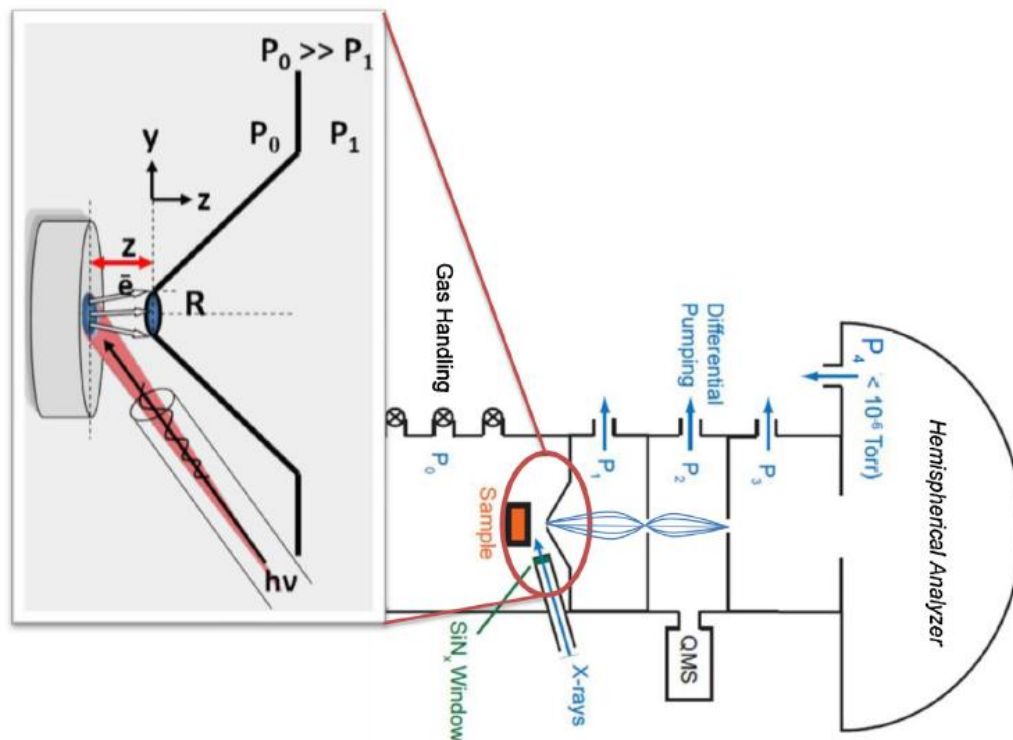


Figure 1-16. A schematic drawing of the ALS endstation.⁴⁵ The inset shows the sample and first aperture region.

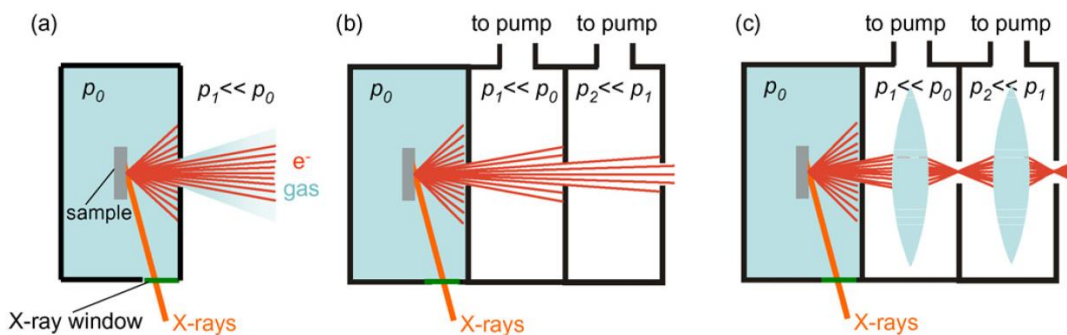


Figure 1-17. Principle of AP-XPS differentially pumped system.⁴⁴ (a) The sample is mounted in a high pressure chamber close to the differentially pumped aperture. (b) Electrons pass through the differentially pumped stages in a traditional differential pumping system. (c) In a differentially pumped electrostatic lens system electrons are refocused onto the apertures.

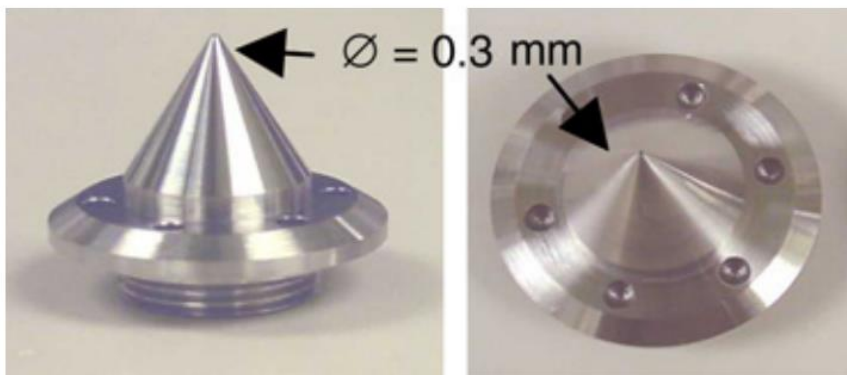


Figure 1-18. Exchangeable conic aperture separating the first pumping stage from the high pressure chamber.⁵⁷

As mentioned in previous sections, *in situ* and *operando* characterization tools are required for direct observations of the physical and chemical processes in electrochemical devices. The terms “*in situ*” and “*operando*” derive from the field of heterogeneous catalysis, in which “*in situ*” studies refer to techniques and measurements for studying catalysts under reaction conditions or conditions relevant to reaction conditions.⁵⁸ The term “*operando*” was introduced recently to describe techniques that are able to characterize a *working* catalyst.⁵⁸ The *operando* techniques combine *in situ* investigations with simultaneous monitoring of the catalytic performance. An *operando* experiment can be viewed as a step towards a “perfect”⁵⁹ or “true”⁶⁰ *in situ* experiment. However, the difference between *in situ* and *operando* studies is not well defined⁵⁸ although it has been discussed over the past few years. This dissertation is not attempting to address this issue but to give a brief overview of the current *in situ* and *operando* studies on SOFCs and SOCs, and more importantly, to present the *operando* AP-XPS studies of electrochemical reactions on solid oxide electrochemical devices.

In this work, simultaneous electrochemical and XPS measurements are collected on the specially designed single-sided solid oxide electrochemical cell, which exposes all cell components for XPS studies. Cerium oxide is used as the electrocatalyst on working electrodes due to its excellent catalytic property, mixed-ionic-electronic-conductivity, high oxygen storage capability, and the kinetically facile changes between Ce^{3+} and Ce^{4+} states in a reducing environment.

Since the emitted photoelectron not only provides information on the elemental and chemical composition of the sample's surface region, but also carries information on both the local chemistry and electrical potentials, it provides a non-contact local probe to measure the local surface potential losses and individual overpotentials across interfaces of an electrochemical cell. Fundamental properties that have been resolved in these studies include redox state changes, electrochemically active region, reaction intermediates, surface kinetics, rate-limiting charge transfer process and reaction mechanisms.

These AP-XPS experiments demonstrate that model thin film electrochemical devices provide valuable information about the electrochemical surfaces/interfaces of interest and can be optimized for applications using different soft X-ray techniques.

1.4 Field of Research

A common strategy used to deduce the chemistry occurring in SOFCs is to carry out extensive *ex situ* analysis following SOFC operation under well-defined conditions. Once the cell is cooled to room temperature and disassembled, many analytical techniques can be used to characterize changes in SOFC components.

Examples of such studies include examination of the SOFC cathodes with X-ray diffraction (XRD),⁶¹ analyses of carbon deposits from unreacted hydrocarbon fuels by gas chromatography-mass spectrometry (GC-MS),⁶² and analysis of cell structure changes after long-term use by scanning electron microscopy (SEM) and XRD.⁶³ However, these techniques do not necessarily provide specific information about the chemistry that occurs on the SOFC. It is not clear whether the information obtained under the post facto ideal conditions can be extrapolated to realistic conditions. The surface structures and surface chemical compositions in far-from-equilibrium conditions and in the pressure of ambient pressure gas environments can be very different from those in UHV. Moreover, kinetics of chemical reactions with high activation barrier can be hindered at low temperatures. These important issues are often referred to as the “pressure gap” and “temperature gap”^{3,45}.

The high temperatures required by SOFCs and SOCs in general restricts *in situ* characterizing techniques to mainly electrochemical methods, such as voltammetry and electrochemical impedance spectroscopy (EIS).^{3,64} For example, the analysis of impedances and overpotentials in electrochemical devices are usually conducted by EIS. This technique has proved successful in resolving the overall electrochemical overpotentials for symmetric cell geometries with uniform current flows and equi-potential lines. Impedance associated with interfacial charge transfers and related processes can be determined by careful circuit simulations. However, this technique is insensitive to asymmetric variations of activities and charge transport, which is the case of a real fuel cell. In addition, EIS provides no chemical information regarding surface chemical species.

One of SOFCs advantages is their ability to utilize various fuels, but this feature also leads to more complex anode chemistry that is difficult to quantify. Multiple reaction pathways including incomplete oxidation as well as non-electrochemical processes are available to the reactants. As *ex situ* and electrochemistry bulk measurements cannot provide direct information for surface kinetics or mechanistic understanding, *in situ* and *operando* diagnostics have been explicitly identified by several review articles^{65,66} as critical tools in unraveling the complex surface chemistry associated with solid oxide electrochemical cells. Specifically, the development of redox stable electrodes, impurity tolerant materials, and further improvements in fuel flexibility all depend on developing mechanistic insight from *in situ* and *operando* studies. The detection and quantification of surface intermediates, redox changes, and microstructure changes during cell operation are essential for validating reaction mechanisms and discovering new materials for next generation devices.⁵⁶

1.5 Scope of the Dissertation

Investigations of electrochemical reactions on solid oxide based electrochemical cells are described in this dissertation. *Operando* AP-XPS are utilized to study the specially designed single-sided electrochemical cell and to extract detailed information of cell processes. MIEC materials of cerium oxide are used as electrocatalysts. Fundamental properties and chemistries have been studied and quantified, which include local surface potentials, redox state changes,

electrochemically active region of MIEC electrodes, reaction intermediates, surface kinetics, and rate-limiting process.

Studies on these single-sided model electrochemical cells are not identical to those conducted on a realistic fuel cell that separates the fuel and the oxidant into two compartments and operates under practical gas pressures. However, their chemistry responsible for energy conversion and materials degradation are closely related. Mechanistic information extracted from investigating the SOCs is valuable and actually guiding to the development of SOFCs due to their similar chemical processes.

The work described here involves close collaboration with Dr. Chunjuan Zhang, Professor Zhi Liu and his research team at ALS. Results from these studies have been published as follows:

1. “Multielement Activity Mapping and Potential Mapping in Solid Oxide Electrochemical cells through the use of operando XPS” Zhang, C.; Grass, M. E.; Yu, Y.; Gaskell, K. J.; DeCaluwe, S. C.; Chang, R.; Jackson, G. S.; Hussain, Z.; Bluhm, H.; Eichhorn, B. W.; Liu, Z. *ACS Catalysis* 2012, 2, 2297
2. “Mechanistic Studies of Water Electrolysis and Hydrogen Electro-Oxidation on High Temperature Ceria-Based Solid Oxide Electrochemical Cells” Zhang, C.; Yu, Y.; Grass, M. E.; Dejoie, C.; Ding, W.; Gaskell, K.; Jabeen, N.; Hong, Y. P.; Shavorskiy, A.; Bluhm, H.; Li, W.-X.; Jackson, G. S.; Hussain, Z.; Liu, Z.; Eichhorn, B. W. *J. Am. Chem. Soc.* 2013, 135, 11572
3. “CO₂ Activation and Carbonate Intermediates: An *Operando* AP-XPS Study of CO₂ Electrolysis Reactions on Solid Oxide Electrochemical Cells” Yu, Y.;

Mao, B.; Geller, A. I.; Chang, R.; Gaskell, K.; Liu, Z.; Eichhorn, B. W. *Phys. Chem. Chem. Phys.* 2014, 16, 11633

4. “Carbon Deposits and Pt/YSZ Overpotentials in CO/CO₂ Solid Oxide Electrochemical Cells” Yu, Y.; Geller, A. I.; Mao, B.; Chang, R.; Liu, Z.; Eichhorn, B. W. *ECS Trans.* 2013, 57(1), 3119

This chapter gives a general introduction of SOFC and AP-XPS, including their basic principles, developments, and challenges. The remainder of this dissertation is arranged as follows:

Chapter 2 describes the *operando* capabilities of the AP-XPS system for mapping local surface potential and detecting the electrochemically active region of thin film ceria electrocatalysts. Electrochemically active region is shown extended 150 - 200 μm away from current collectors. The foreign elements of silicon and carbon on the SOC electrode are found as excellent trace markers of surface potentials and active region.

Chapter 3 presents the observations of transient intermediates accumulating in the active region of an operating CeO_{2-x} SOC through the use of *operando* AP-XPS. The rate-limiting charge transfer process in both H₂O electrolysis and H₂ electro-oxidation reactions are identified. The observed potential separation of the adsorbed OH⁻ and incorporated O²⁻ ions is interpreted using the effective double layer model and the surface potential step model⁶⁷, which provides insights into the gas-solid interface chemistry.

Chapter 4 and 5 gives emphasis on electrolysis of CO₂ and electro-oxidation of CO over CeO_{2-x}-based SOCs. Carbonate species are identified as reaction

intermediates in the two electrochemical reactions. Their steady-state concentration increase during CO₂ electrolysis and the slight decrease during CO electro-oxidation on the ceria electrode surface suggest that the charge transfer process to/from CO₃²⁻ is rate-limiting in the electrochemical processes. The graphitic carbon formation on the ceria electrode surfaces during CO₂ electrolysis extends the electrochemically active region by enhancing the electronic conductivity of the electrode. Also, measurements of overpotentials at the Pt-YSZ edge reveal very high charge transfer resistance at the electrode-electrolyte interface for CO₂ electrolysis that dominated the cell losses in these environments.

Finally, Chapter 6 presents a summary of the major contributions of this work, along with recommendations for future studies in the field.

Chapter 2

Activity Mapping and Potential Mapping on Solid Oxide Electrochemical Cell by *Operando* XPS

2.1 Introduction

Solid oxide fuel cells (SOFCs) are energy conversion devices that convert fuels and oxygen to electric power. The successful development of commercial SOFCs leads to tremendous research interest in solid oxide electrochemical cells (SOCs) in general. SOCs are a general class of solid oxide electrochemical devices that encompass SOFCs and solid oxide electrolysis cells (SOECs), which generate fuel from electricity.

Although SOCs and SOFCs already have limited commercial success, there are still many issues that must be resolved before they become significant contributor to the alternative energy infrastructure. The lack of direct knowledge regarding the surface chemistry and electrochemical processes that govern these systems impedes the advancement of designs of membrane electrode assemblies in SOCs. More specifically, the gaseous reactant environment and high operating temperatures (>600 °C) precludes the use of most surface science analytical tools such as atomic force microscopy (AFM), scanning tunneling microscopy (STM), and traditional ultrahigh vacuum (UHV) X-ray photoelectron spectroscopy (XPS).

Recently, new *in situ* and *operando* methods have been developed to address these issues and are beginning to provide fundamental insight into SOC processes.

These methods include *in situ* Raman,^{20,68,69} ambient pressure X-ray photoelectron spectroscopy (AP-XPS),^{56,70} X-ray diffraction (XRD),⁷¹ X-ray adsorption spectroscopy (XAS),⁷² and thermal imaging and vibrational spectroscopy³.

In this chapter, the use of AP-XPS to spatially resolve local surface potentials, electrochemically active region and shifts in surface oxidation states in operating SOCs is demonstrated.

2.1.1 Kinetic Energy Shift of Photoelectrons

As mentioned in Chapter 1, Section 1.3.2, the emitted photoelectrons not only provide information on the elemental identities and chemical composition of the sample surface, but also carry information on both the local chemistry and electrical potentials. When the sample surface is charged, the photoelectron spectra show shifts in the apparent binding energy (BE) values (*i.e.*, electron kinetic energy (KE) values).⁷³ This binding energy shift originates for the change in the local Fermi level (see **Figure 1-13**).^{56,73-76} Since the Fermi level changes with the local electric potential, the magnitude of binding energy shift (ΔBE in electron volts) is related to the local potential (V_L) as:

$$\Delta BE = - e \cdot V_L \quad (\text{Eq. 2-1})$$

where e is the elementary charge and has a negative sign ($e = -1.602 \times 10^{-19}$ C).

Specifically, a positive charge on an atom lowers the Fermi level and consequently the kinetic energy level of the emitted electron. However, measurement of the photoelectron KE is relative to the vacuum level of the spectrometer, which is not changing with the positive charge on the sample (**Figure 1-13**). Therefore, the measured KE value is reduced, which leads to an increase in the apparent BE value

according to **Eq. 1-16** ($BE = h\nu - KE'$, where KE' is the measured kinetic energy value after calibration with the spectrometer work function, see Chapter 1, Section 1.3.2 for more details).

Similarly, a negative potential bias raises the Fermi level, resulting in an increase in the measured KE value, and a decrease in apparent BE relative to the unbiased condition. In sum, a positive potential bias leads to an increase in the apparent BE while a negative potential shifts the BE to a decreased value, as described in **Eq. 2-1**.

Therefore, by measuring ΔBE of photoelectrons of selected elements at various positions on a biased SOC surface, the local surface potential information at that position can be directly measured.⁷³⁻⁷⁶ This correlation between the apparent binding energy shifts ΔBE and V_L allows for a direct and contactless measure of local surface potentials in SOCs.

2.1.2 Scope of the Chapter

In this chapter, the *operando* capabilities of the AP-XPS system are explored for mapping local surface potential and detecting the electrochemically active region of thin film ceria electrocatalysts. High resolution mapping of local surface potentials and overpotentials in an operating SOC through the use of AP-XPS are demonstrated.

The AP-XPS studies are performed on specially designed single-sided SOCs. These ceria-based SOCs have a planar architecture that places all the cell components on the same side of the electrolyte for XPS studies. As such, all cell components are exposed to both the fuel and the oxidant gas. Binding energies of the surface species

and the shifts in their BE values are measured *operando* (~720 °C, 0.5 Torr of 1:1 H₂/H₂O, ±1.2 V).

Trace foreign elements, such as Si, are found as convenient markers of local potential across the entire SOC surface, and volatile elements, such as carbon, are irreversibly oxidized on the ceria surface to demarcate regions of electrochemical activity. Also, the surface Ce³⁺/Ce⁴⁺ ratios, that is, surface oxygen vacancy density, are shown to be readily modified by different bias voltages and gas environments, which demonstrates the electrochemical approach to adjust the surface vacancy of CeO_{2-x}.

The work described here has involved close collaboration with Dr. Chunjuan Zhang, Professor Zhi Liu, and his research team at ALS. My contribution includes fabricating a series of zirconia-based SOCs having dense ceria working electrodes, performing the XPS measurements at ALS, analyzing XPS spectra by using the CasaXPS software, and further interpreting the results.

2.2 Experimental

2.2.1 Solid Oxide Electrochemical Cell Preparation

Yttria-stabilized zirconia (YSZ) powder of 8 mol% was purchased from Tosoh Inc. and was pressed in a coaxial stainless steel die-press. The as-pressed YSZ pellets were cut into square supports, heated to 1450 °C (1 °C/min), and sintered for 3 h. The final YSZ supporting electrolytes had dimensions of 10 mm × 10 mm × 1 mm. They were sequentially cleaned in acetone, ethanol, and deionized water and thoroughly

dried before sputtering electrode thin films. Aluminum oxide (Al_2O_3), Au, and Pt electrodes were sputter-deposited using an AJA International, ATC 1800 V sputtering unit with patterned stainless steel shielding masks (FotoFab). The thicknesses of the sputtered Al_2O_3 , Au, and Pt films were 30, 300, and 300 nm, respectively. Ceria films were sputtered-deposited under 5 mTorr of O_2/Ar gas mixture containing 10% O_2 using a PVD 75 sputter deposition unit from Kurt J. Lesker Co. Two thicknesses (50 and 250 nm) of CeO_{2-x} films were prepared for this study. All samples were pre-annealed at 800 °C for 3 h before electrochemical and XPS measurements.

The structural integrity and film thicknesses were evaluated through XRD and SEM analyses. **Figure 2-1** shows the cross-sectional SEM image of the 50-nm-thick ceria electrode. Typical grain sizes of ceria films are approximately 20 nm, and their structure is superimposed over the $\sim 1 \mu\text{m}$ grains of the underlying YSZ support.

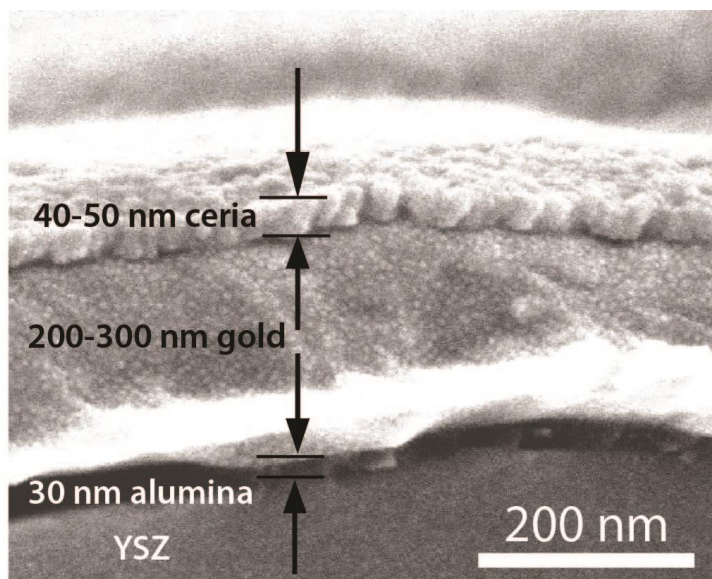


Figure 2-1. SEM image of the cross-section structure for a fractured 50 nm thick CeO_{2-x} cell.

2.2.2 Electrochemical Measurements

Electrochemical characterization of two-probe linear sweep voltammetry (LSV) and electrochemical impedance spectroscopy (EIS) measurements were conducted by using a Bio-Logic potentiostat.

The single-chamber cells were clamped onto a ceramic heater and loaded into the AP-XPS end-stations⁷⁷ at beamline 9.3.2 of the Advanced Light Source (ALS) at Lawrence Berkeley National Laboratory (LBNL). The spring-loaded probes of the cell mounting platen served as both clamps and electrical contacts/current collectors for electrodes (**Figure 2-2**).⁷⁸ In the experiments, H₂ and H₂O were sequentially leaked into the XPS chamber with a partial pressure of ~0.25 Torr each. Once the gas mixture stabilized at the target pressure, the cell was heated to approximately 720 °C. Temperatures were normalized to external pyrometer measurements by the bulk resistance values from impedance data. **Figure 2-2** shows the operating cell inside the AP-XPS end-station at ~720 °C.

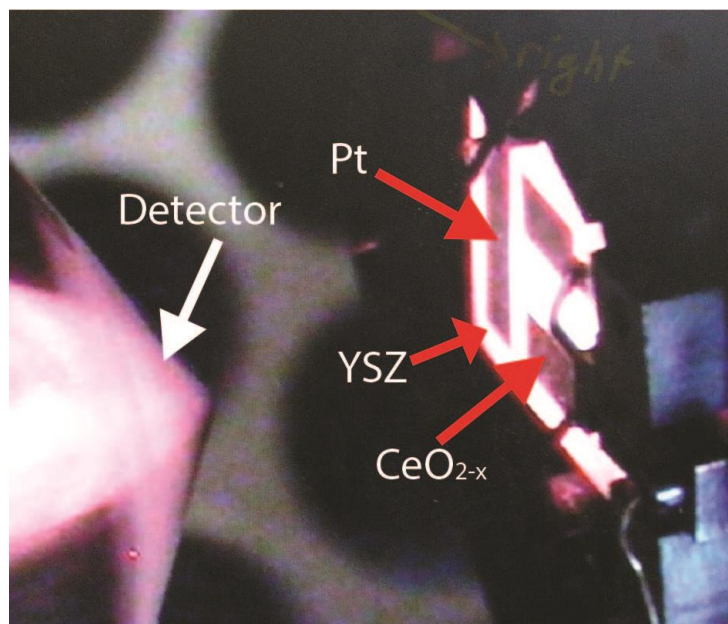


Figure 2-2. A photograph of an operating cell with the XPS electron detector (the cone) and three electrical contact probes (bent wires).

In each experiment the Au current collector of the working electrode (WE) was always grounded to the XPS chamber ($V_{\text{Au}} = 0.0 \text{ V}$) and the Pt counter electrode (CE) was biased by the potentiostat.^{56,79} Hence, the overall cell bias V_{Cell} is defined as the potential difference between the Pt electrode and the Au current collector: $V_{\text{Cell}} \equiv V_{\text{Pt}} - V_{\text{Au}}$, which simplifies to $V_{\text{Cell}} = V_{\text{Pt}}$ in this study.

2.2.3 *Operando* Ambient Pressure X-ray Photoelectron Spectroscopy Measurement

Operando AP-XPS measurements were conducted simultaneously with the electrochemical characterizations at $\sim 720 \text{ }^\circ\text{C}$ with 0.5 Torr of 1:1 $\text{H}_2/\text{H}_2\text{O}$ gas mixtures. Two-dimensional (2D) AP-XPS spectral maps (binding energy versus position) were obtained by using the differentially pumped electron analyzer^{77,78} installed at beamline 9.3.2 of the ALS at LBNL.⁷⁷

The sample was oriented such that the X-ray beam incident angle was 75° and the electron emission angle was 0° with respect to the sample normal. The photon energy used for C 1s, Ce 4d, Pt 4f and Zr 3d spectra was 490 eV and for O 1s was 650 eV. The binding energies calibrations of C 1s and Ce 4d were made by referencing against the bulk Au $4f_{7/2}$ peak (BE = 84.0 eV⁴²) collected with 490 eV photon energy.

Analysis of the 2D XPS intensity maps was obtained by slicing the XPS intensity maps into 20- μm segments against the axis of position.^{30,56,80} CasaXPS software (Version 2.3.15) was used for data analysis. After subtracting a Shirley background, each slice was fitted using a nonlinear, least squares routine with mixed Gauss-Lorentz function of 70% Gaussian and 30% Lorentzian.

2.3 Results & Discussions

The single-sided polycrystalline YSZ cell contains one 300-nm-thick Pt counter electrode (CE) and two CeO_{2-x} working electrodes (WEs) with 300-nm-thick Au current collectors. The alumina films underneath each of the Au films block ionic transport between YSZ and Au.⁸¹ By blocking the O^{2-} transport into the Au pad, the electrochemical side reactions on the Au current collector are precluded. Dense thin ceria films (50 or 250-nm-thick) are patterned on top of the Au leaving elongated Au pads exposed for electric connections (**Figure 2-3**). Approximately 350 μm regions of the ceria film has direct contact with the supporting YSZ electrolyte, allowing O^{2-} ions move across the CeO_{2-x} -YSZ interface. Approximately 250 μm of uncovered YSZ separates the ceria edge and the nearest Pt edge. This cell geometry with the

CeO_{2-x} WE and Pt CE deposited on the same side of the YSZ electrolyte support allows full access to all cell component surfaces for XPS studies.

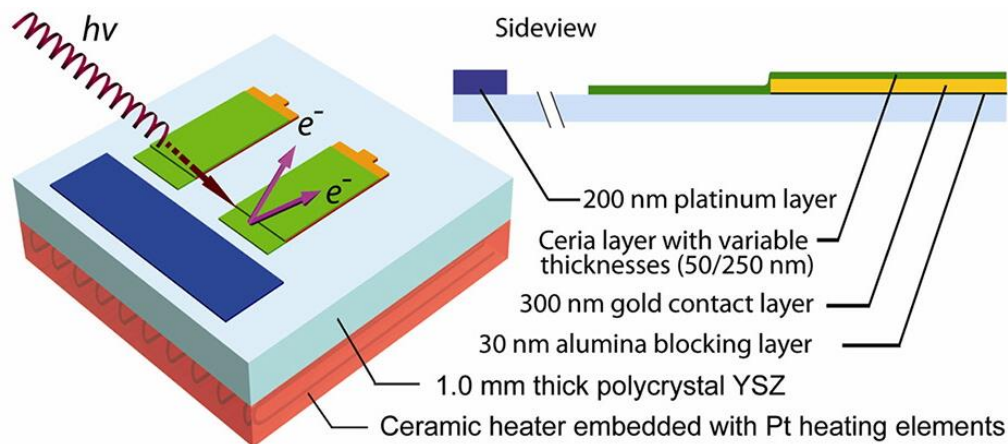


Figure 2-3. Schematic illustration of cell geometry. The single-chamber polycrystalline YSZ cell has one Pt CE (blue) and two ceria WEs (green) with Au current collectors (gold). Underneath the Au films, 30 nm thick alumina films (black) are deposited to block the ionic transport between YSZ and Au. Only one ceria edge has direct contact with the YSZ electrolyte to obtain defined current flow region.

Since both the CeO_{2-x} WE and the Pt CE are exposed to the same gas environment of 0.5 Torr of 1:1 H₂/H₂O at ~720 °C, no thermodynamic driving force exists when the electrochemical reactions on both electrodes reach equilibrium with the gas phase. This situation results in a near-zero open-circuit voltage (OCV). At OCV, the cell surfaces reach thermal equilibrium with the H₂ and H₂O gases as described by the following equation:



On the ceria electrode electrons locate at Ce sites and reduce Ce⁴⁺ to Ce³⁺ as described by the polaron hopping mechanism (see Chapter 1, Section 1.2.5). When Ce^{3+/4+} species and oxygen vacancy sites (V_O) on the ceria electrode are taken into consideration, the above equation can be written as:



As discussed in Chapter 1, Section 1.2.5, ceria shows mixed-ionic-electronic-conducting (MIEC) behavior under low oxygen partial pressure conditions due to the presence of oxygen vacancy and partial reduction of Ce^{4+} to Ce^{3+} . The low gas pressure in this study satisfies this situation. Therefore, under positive or negative bias, ceria allows electric current pass across the SOC by exchanging electrons with the Au current collector and O^{2-} with the YSZ electrolyte support. Specifically, at positive bias ceria functions as a cathode and promotes H_2O electrolysis reactions, while Pt acts as an anode and promotes H_2 electro-oxidation. At negative bias, the roles of the electrodes are reversed such that H_2O electrolysis occurs on Pt and H_2 electro-oxidation occurs on CeO_{2-x} . **Figure 2-4** shows a schematic illustration of the electrochemical reactions occurring on the single-sided ceria-based SOC under positive and negative biases.

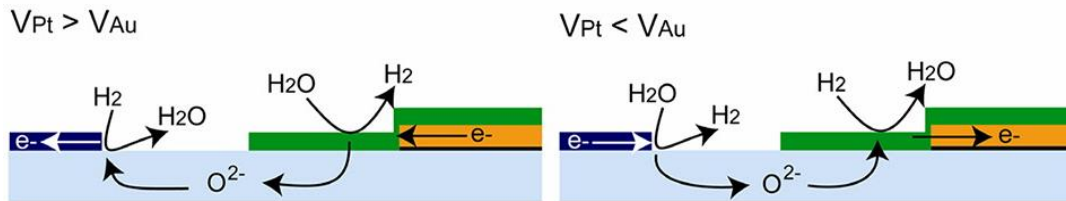


Figure 2-4. Schematic illustrations of cell cross sections illustrating current flow directions and surface reactions under different biases. The following color code identifies the cell components: dark blue, Pt; light blue, YSZ; black, alumina; orange, Au; green, ceria (not drawn to scale).

A positive potential applied on the Pt electrode drives electrons from the Au current collector to ceria, and moves O^{2-} from the ceria surface down to the YSZ and out to the Pt electrode (**Figure 2-4**). Under such conditions, **Eq. 2-3** is driven away from the equilibrium value, and is favored in the forward directions on CeO_{2-x} .

Therefore, the positive bias promotes H₂O electrolysis on the CeO_{2-x} electrode surface and H₂ electro-oxidation is promoted at the Pt-YSZ three phase boundary (TPB).

When the bias is reversed (negative bias on Pt), the surface reactions occur in the opposite direction to give H₂ electro-oxidation on CeO_{2-x} and H₂O electrolysis at the Pt-YSZ edge.

2.3.1 Electrochemistry Characterization

As shown in **Figure 2-4**, the SOC geometry requires a lateral movement of electrons and a vertical transport of O²⁻ in ceria thin-film electrodes because of the lack of an ionic source/drain at Au and an electronic source/drain at YSZ, respectively. To verify O²⁻ ion transport pathways, a control cell without a ceria film was fabricated. In this cell, there is no O²⁻ pathway between the Au electrode and the Pt electrode due to the alumina blocking layer beneath the Au film. **Figure 2-5** shows the electrochemical characterization of linear sweep voltammetry (LSV) from -1.2 V to +1.2 V. The control cell (*i.e.*, no ceria) shows negligible currents under bias, which verifies the current-blocking function of the alumina layer and confirms the O²⁻ ionic transport pathway in this cell geometry.

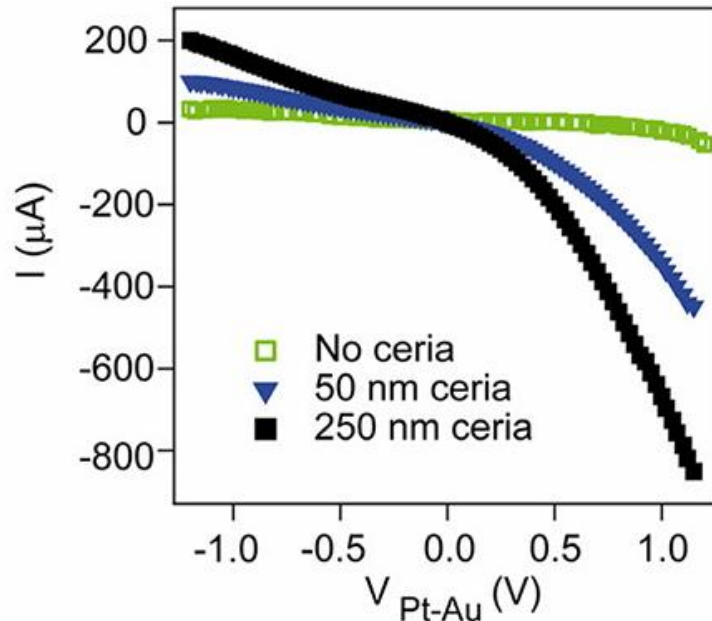


Figure 2-5. Linear sweep voltammetry (LSV) polarization curves of cells with different CeO_{2-x} film thicknesses (0, 50, and 250 nm) measured at ~ 720 °C with 0.5 Torr of 1:1 $\text{H}_2/\text{H}_2\text{O}$ mixture.

When H_2O electrolysis occurs on CeO_{2-x} ($V_{\text{Pt}} > V_{\text{Au}}$), the cell currents are significantly higher than those when CeO_{2-x} promotes H_2 electro-oxidation ($V_{\text{Pt}} < V_{\text{Au}}$). In the LSV curves (**Figure 2-5**), both the 50 and the 250-nm cells show larger currents at positive biases than negative biases. While some of the increase in current is due to the higher activity of Pt for H_2 oxidation than H_2O electrolysis,^{70,82} a high overpotential (η) is shown required on ceria to promote H_2 electro-oxidation for a given current magnitude than that for H_2O electrolysis. (Further discussion is given in Section 2.3.3, Section 2.3.4, and Section 2.3.5) The higher overpotential associated with the H_2 oxidation on the ceria surface indicates the reduced catalytic activity of ceria for H_2 electro-oxidation versus H_2O electrolysis. The lower electronic conductivity of CeO_{2-x} at negative bias can also be responsible for the lower currents at these conditions. However, the CeO_{2-x} maintains MIEC character at negative bias

as evidenced by the extended electrochemically active region beyond the Au current collector, which is further discussed in Section 2.3.4.

In addition to the different behaviors at positive and negative bias, the results in **Figure 2-5** also reveal that the thicker ceria films show larger currents for both reaction directions relative to thinner films.

Results of EIS measurement under various applied biases is shown in **Figure 2-6**. The electrolyte bulk resistance is obtained from the high frequency intercepts of EIS Nyquist plots. Typically, the electrolyte bulk resistance at 720 °C is within the range of 350 - 400 Ω. Total polarization resistances under negative biases (-0.3 V and -1.0 V) are significantly larger than those at positive bias (+0.3 V and +1.0 V), which is also consistent with the LSV data.

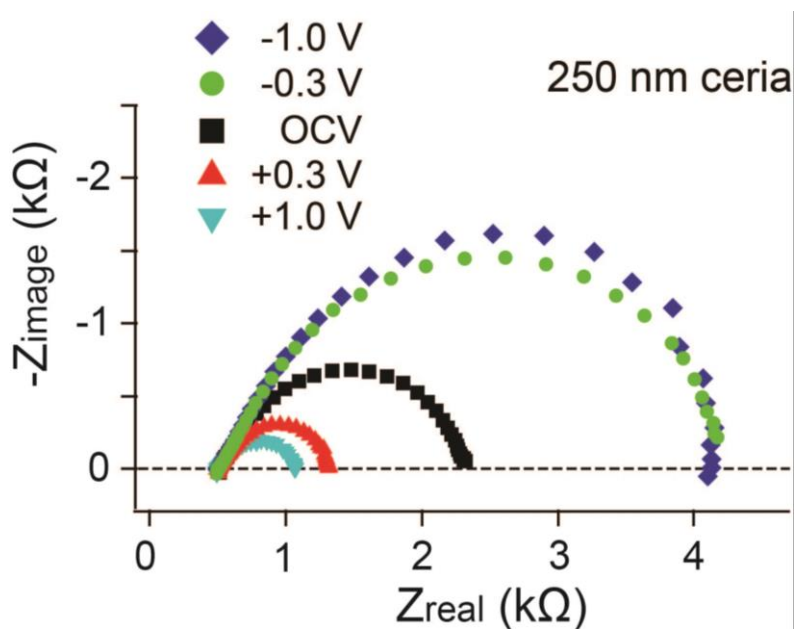


Figure 2-6. Electrochemical impedance spectroscopy (EIS) of a 250-nm-thick CeO_{2-x} cell under varied applied biases (-1.0, -0.3, OCV, +0.3, and +1.0 V) at ~720 °C with 0.5 Torr of 1:1 H₂/H₂O mixture.

2.3.2 Two-Dimensional X-ray Photoelectron Spectroscopy Mapping

Through the use of AP-XPS at ALS beamline 9.3.2, the surface potential and oxidation state changes that occurred with applied electrochemical biases are investigated. As depicted in **Figure 2-7**, the two-dimensional detector system installed at the end-station of beamline 9.3.2 can obtain 2D XPS intensity maps as a function of position with a spatial resolution up to 20 μm . **Figure 2-7** shows the C 1s, Si 2p, Ce 4d, and Zr 3d XPS spectra for a 600- μm -long linear window on a 250-nm-thick ceria electrode. XPS photoelectron BE values (abscissa) are plotted against the cell position (ordinate) with the photoelectron intensities denoted by the color intensities. A schematic cell drawing and the color scale notation are given on the left and right of the figure, respectively. The data in **Figure 2-7** are collected with incident photon energy of 490 eV at +1.2 V cell potential, which promotes H_2O electrolysis on the ceria electrocatalyst.

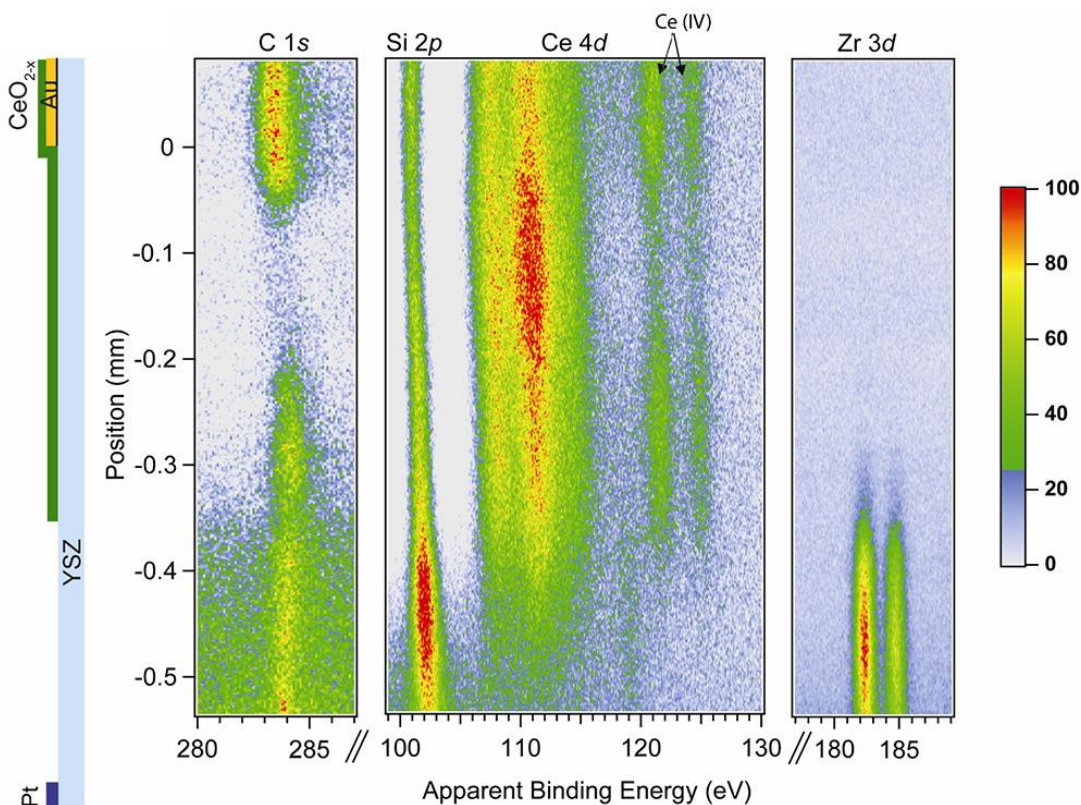


Figure 2-7. Spatially resolved XPS spectra of the C 1s, Si 2p, Ce 4d, and Zr 3d spectra obtained with a two-dimensional (2D) area detector on a 250-nm-thick CeO_{2-x} cell at +1.2 V applied potential ($\sim 720^\circ\text{C}$ with 0.5 Torr of 1:1 $\text{H}_2/\text{H}_2\text{O}$ mixtures). The peaks labeled “ Ce^{4+} ” are associated only with Ce^{4+} species. The peak intensity is indicated with a color annotation of the intensity percentage on the right. The sideview of schematic cell drawing shows the correlation of the cell position with the XPS spectra.

Spatially resolved XPS spectra (**Figure 2-7**) of the cell reveal the electrode edges and the different materials on the surface. The XPS spectrum images are aligned with the cell schematic on the left. At the CeO_{2-x} electrode edge, the Ce 4d peaks start to fade as the Zr 3d peaks start to appear. The lack of sharp edges at interfaces is likely due to material tailing associated with the deposition techniques. Since the Au current collector is buried underneath the CeO_{2-x} electrode, there is no Au signal in the XPS spectra. As a result, the Au edge is determined by careful calibration of the distance between the Au and the Pt pads in the cell photo.

2.3.3 Local Surface Potential Mapping

As discussed in Section 2.1.1, the magnitude of binding energy shift is related to the local potential as: $\Delta BE = -e \cdot V_L$. By measuring ΔBE of photoelectrons of selected elements at various positions on the cell surface, the V_L information at a certain position can be directly assessed,⁷³⁻⁷⁶ which allows for a direct, contactless measure of local surface potentials in SOCs. By horizontally slicing the 2D XPS maps in **Figure 2-7**, the XPS spectra of given elements at given positions can be plotted and fitted. Mapping local surface potentials across the cell can be accomplished by calculating the shifts of XPS peak positions of different elements (Pt, Zr, and Ce) at varied positions. **Figure 2-8** plots the V_L values across the SOC from Pt to Au.

Alternatively, monitoring the V_L values of inert foreign elements that are present in trace amounts, such as silicon, provides a convenient, continuous probe of V_L information (**Figure 2-8**). The impurities might come from thin film sputtering, annealing, or sample transfer processes. At elevated temperatures and low gas pressures, these trace elements tended to migrate to the sample surface under certain conditions and are easily detected in the XPS. The local potentials in the active region extracted from the Si 2p data are virtually identical to the potential maps obtained from the sliced Ce and Zr data shown in **Figure 2-8** and the Ce 4d spectra reported previously.⁵⁶ But more conveniently, the ΔBE of the Si 2p photoionizations probe the entire surface potential from Pt to Au without any uncertainties associated with changes in materials at interfaces.

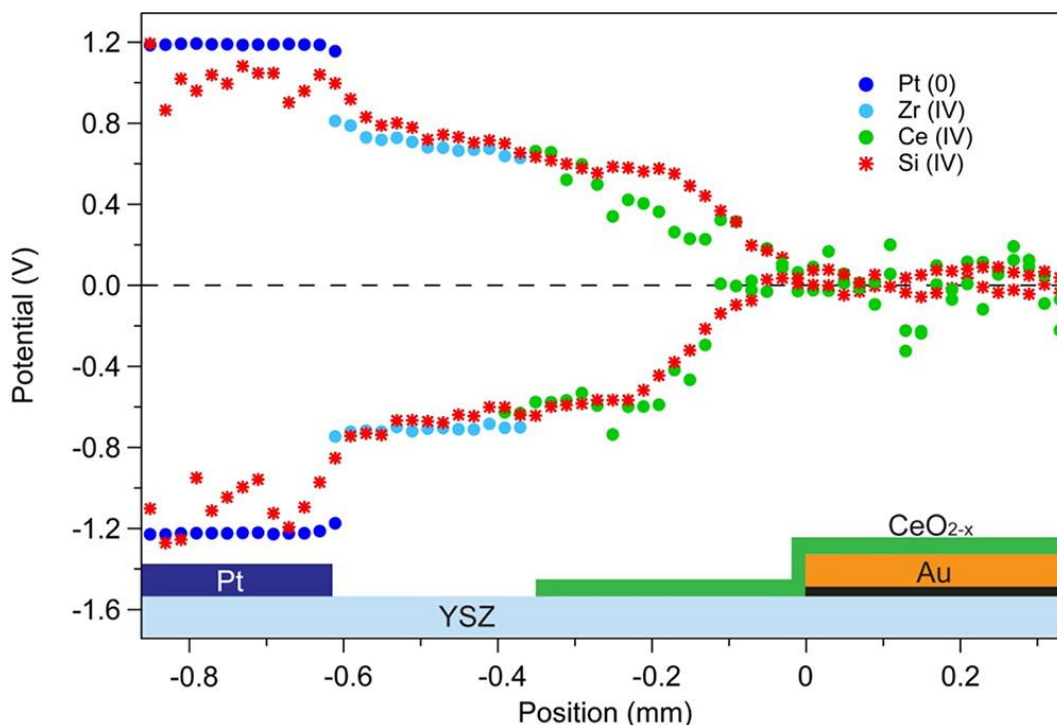


Figure 2-8. Plots of the local surface potentials calculated from shifts in photoelectron kinetic energy away from OCV condition. The data shown are collected at +1.2 V (-600 μ A) and -1.2 V (+130 μ A) applied bias (\sim 720 $^{\circ}$ C with 0.5 Torr of 1:1 H_2/H_2O mixtures). The V_L values of Pt^0 , Zr^{4+} , and Ce^{4+} are labeled in dark blue, light blue, and green dots, respectively. The red dots show the V_L values of Si^{4+} across the entire cell. The data are extracted from two windows of the XPS area detector that covered the entire cell surface: -0.85 to -0.25 mm for window 1 and -0.25 to +0.35 mm for window 2. Data in window 2 at negative bias are corrected by 0.12 V for beam drift by aligning the Si local potential values at the edges of the two windows.

2.3.4 Electrochemically Active Region

Figure 2-9 shows a narrow region of the potential map calculated from ΔKE in Si 2p spectra for both the 50 and 250 nm ceria cells from the CeO_{2-x} -YSZ edge to \sim 200 μ m on top of the Au current collector. The ΔBE of Si 2p spectra reveal the local surface potentials values and delineate the electrochemically active region. The active region is associated with large potential drops on the ceria surface⁵⁶ and large shifts in Ce^{3+}/Ce^{4+} ratios (**Figure 2-10**) that occur close to the Au edge.

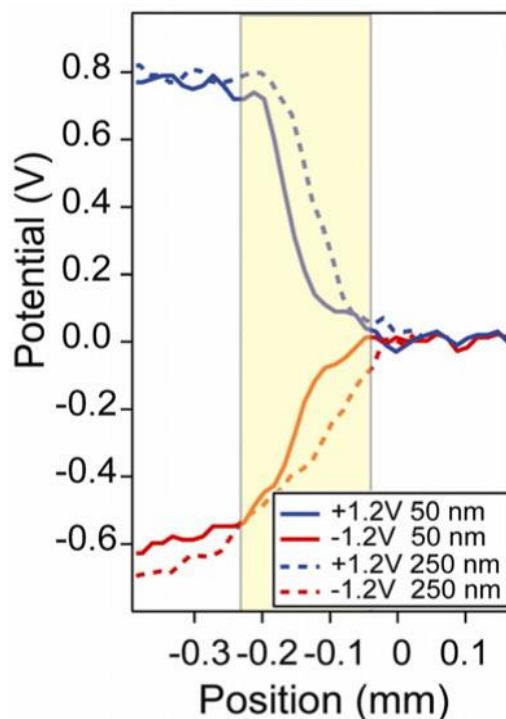


Figure 2-9. Signatures of the electrochemically active region (yellow boxes) on the 50-nm and 250-nm thick CeO_{2-x} electrodes under applied biases (± 1.2 V) at ~ 720 °C with 0.5 Torr of 1:1 $\text{H}_2/\text{H}_2\text{O}$ mixture. The cell surface potentials calculated from the ΔKE of Si 2p spectra show significant potential drops close to the Au current collectors located at 0 mm.

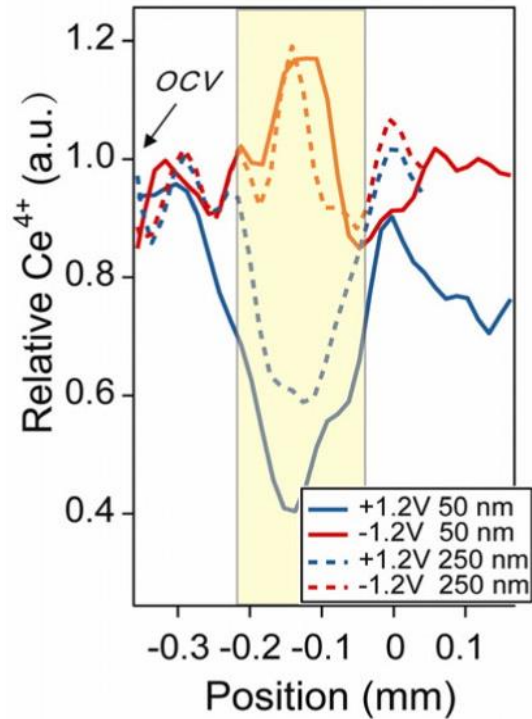


Figure 2-10. The relative concentrations of Ce^{4+} measured *operando* under +1.2 V and -1.2 V at ~ 720 °C with 0.5 Torr of 1:1 $\text{H}_2/\text{H}_2\text{O}$ mixture. The concentrations are determined from the ratio of the high BE Ce^{4+} peaks to the total fitted Ce area.⁵⁶ The concentration values are normalized to the equilibrium OCV value, which is defined as 1.0.

Analysis of volatile elements such as carbon also reveal regions of electrocatalytic activity. The C 1s spectra in **Figure 2-7** shows the spatially resolved carbon coverage over the sample surface. **Figure 2-11** presents the C 1s peak intensity (*i.e.*, the relative carbon concentration) as a function of position on both 50-nm and 250-nm-thick ceria electrocatalysts. Carbon initially appear over the entire cell, but after running the cells at ± 1.2 V for a few cycles the electrochemical excitation completely remove surface carbon from the active region of the ceria surfaces (**Figure 2-7**).

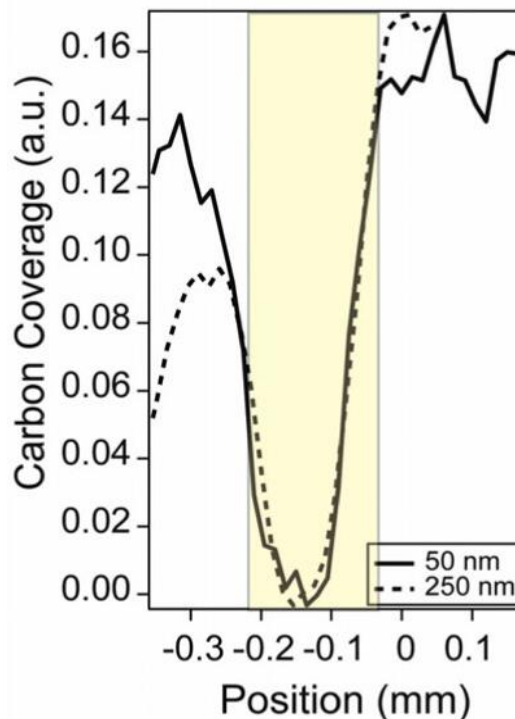


Figure 2-11. The relative carbon concentration on the CeO_{2-x} surface after running the cells at ± 1.2 V with 0.5 Torr of 1:1 $\text{H}_2/\text{H}_2\text{O}$ mixtures for a few cycles. The absence of carbon delineate the electrochemically active region.

Specifically, at negative bias, the disappearance of carbon in the active region is due to the half-cell reactions of carbon electro-oxidation, *i.e.*, $\text{C} + \text{O}^{2-} \rightarrow \text{CO} + 2\text{e}^-$ or $\text{C} + 2\text{O}^{2-} \rightarrow \text{CO}_2 + 4\text{e}^-$, on the electrocatalytic CeO_{2-x} surface. At positive bias, surface carbon oxidation in the electrochemically active region might also be facilitated by catalyzed reactions with the high-temperature steam: $\text{C} + \text{H}_2\text{O} \rightarrow \text{CO} + \text{H}_2$.^{83–85} To quantify more precisely the mechanism of carbon oxidation further studies are necessary; however, the carbon oxidation happens primarily in the electrochemically active region that involves electrocatalytic oxidation, and, therefore, carbon depletion serve as an excellent spatial indicator of electrocatalysis.

Because the carbon oxidation reaction is irreversible, there is a slightly larger area of carbon depletion (**Figure 2-11**) relative to the regions of surface potential

drops (**Figure 2-9**) and Ce oxidation state changes (**Figure 2-10**). The surface carbon that is present on virtually the entire cell can be used as an additional signature of surface electrochemical activity due to its irreversible oxidation. The use of carbon markers of electrocatalytic activity are potentially very useful for optical probes that can easily detect carbon build-up/depletion in functional solid oxide fuel cells.³

2.3.5 Overpotential at the Electrode-Electrolyte Interface

The use of shielding masks for the thin film electrode deposition creates a porous region of Pt at the Pt-YSZ interface. As a result, the Pt electrode changes from a dense nonporous film to a porous film and eventually to islands of Pt particles on YSZ as one traverses across the Pt-YSZ interface (**Figure 2-12**).

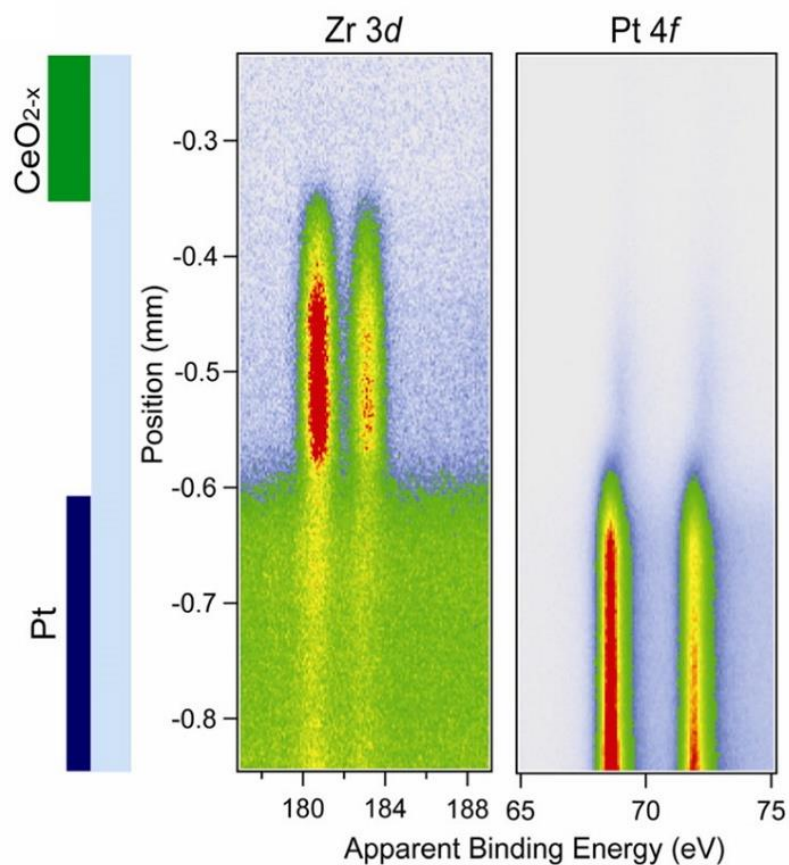


Figure 2-12. Spatially resolved Pt 4f and Zr 3d spectra of the 250-nm-thick CeO_{2-x} cell at -1.2 V applied potential ($\sim 720^\circ\text{C}$ with 0.5 Torr of 1:1 $\text{H}_2/\text{H}_2\text{O}$ mixtures). A schematic drawing of the cell is aligned to position on the left.

As shown in **Figure 2-12**, the local potential of the contiguous Pt film remains constant and the shift is equal to the applied cell bias of -1.2 V. However, the local potentials of the isolated Pt particles on the YSZ electrolyte are shifted relative to the Pt dense film and are equivalent to those of the YSZ support. The porous nature of the Pt edge at the Pt-YSZ interface provides the possibility to measure local surface potentials of Pt and YSZ at the same location.

The ability to obtain local surface potential measurement of two different materials at the same location allows for a direct measure of the local charge transfer

overpotential, η_L . Overpotential is the potential difference between the electrochemically biased and thermodynamically determined non-biased conditions. Since the single-sided SOC used in this study gives the equilibrium OCV condition as 0 V, the potential difference between Pt and YSZ across the interface under OCV condition is zero:

$$\Delta V_{L(\text{Pt-YSZ})}^{\text{eq}} = V_{\text{Pt}}^{\text{eq}} - V_{\text{YSZ}}^{\text{eq}} = 0 \text{ V} \quad (\text{Eq. 2-4})$$

Hence the overpotential at the Pt-YSZ interface can be simplified to:

$$\eta_{L(\text{Pt-YSZ})} = \Delta V_{L(\text{Pt-YSZ})} - \Delta V_{L(\text{Pt-YSZ})}^{\text{eq}} = \Delta V_{L(\text{Pt-YSZ})} \quad (\text{Eq. 2-5})$$

Therefore, the overpotentials at the interface, $\eta_{L(\text{Pt-YSZ})}$, could be directly described as the difference in local potentials of Pt and YSZ under bias condition at the same location:

$$\eta_{L(\text{Pt-YSZ})} = \Delta V_{L(\text{Pt-YSZ})} = V_{L(\text{Pt})} - V_{L(\text{YSZ})} \quad (\text{Eq. 2-6})$$

Figure 2-13 shows the Pt-YSZ local overpotentials as the difference in Pt and Zr local potentials under biases. At the edge of contiguous Pt film and the YSZ electrolyte interface (position -0.62 mm), the η_L values reach a maximum at both positive and negative biases. Under +1.2 V, the maximum $\eta_L = 0.4$ V at $I = -618 \mu\text{A}$, whereas at -1.2 V applied bias, a slightly larger $\eta_L = -0.5$ V at a much lower current ($I = +148 \mu\text{A}$). The substantially larger ratio of $\eta_{L(\text{Pt-YSZ})}$ to I at negative bias reveals the higher charge transfer resistance that is associated with H_2O electrolysis at the Pt-YSZ interface. This difference may result from a lower affinity of H_2O gas on Pt than H_2 . Also, at +2.0 V bias the spillover effect of oxygen^{73,86} from YSZ electrolyte to the Pt electrode and the simultaneous spillover of hydrogen from Pt to YSZ facilitate H_2

electro-oxidation at the Pt-YSZ interface, which further contributes to the relatively lower charge transfer resistance associated with the reaction.

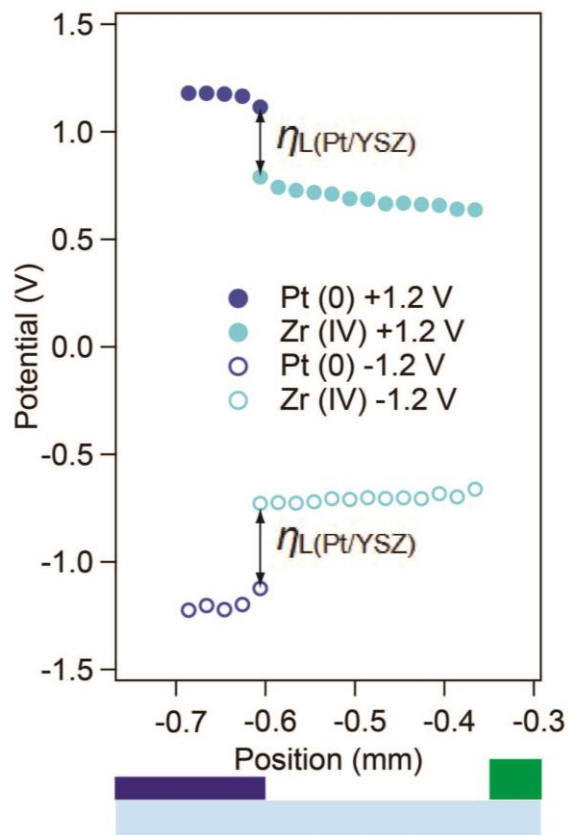


Figure 2-13. The Pt⁰ and Zr⁴⁺ surface potentials across the Pt-YSZ interface. Data are calculated from the kinetic energy shifts of Pt 4f and Zr 3d spectra under +1.2 V and -1.2 V applied biases (~720 °C with 0.5 Torr of 1:1 H₂/H₂O mixtures). The Pt in the contiguous Pt electrode (≤ -0.60 mm) has local potentials equal to the applied bias. The interfacial potential difference between Pt and YSZ ($\Delta V_{L(\text{Pt-YSZ})}$) is equal to the local Pt-YSZ charge transfer overpotential, η_L .

By isolating the individual overpotentials and measuring bulk ohmic losses through electrochemical measurements, a complete picture of voltage drops across the entire SOC is obtained. As illustrated above, the charge transfer overpotentials on Pt (and ceria) are very condition dependent and provided significant insight into the electrochemical processes.

2.4 Summary

The spatially resolved XPS spectra presented here illustrate the *operando* capabilities of the AP-XPS system for mapping local surface potential and detecting the electrochemically active region of thin film ceria electrocatalysts. All of the ceria-based SOCs with this geometry show similar ranges of electrochemically active region that extends 150-200 μm away from current collectors. The foreign elements of silicon and carbon present on the SOC electrode serve as trace markers of surface potentials and active region. The AP-XPS studies on operating SOCs provide fundamental information and parameters governing electrochemical reactions of the cells, which could be of significant value to practical cell design and material selection.

At the same time, such model SOCs can be used to control the surface oxygen vacancies of CeO_{2-x} electrode. Such an approach can create different non-equilibrium CeO_{2-x} surfaces that are expected to have different catalytic properties as catalysts and supporting materials. This approach could potentially have significant implications on the fields of SOECs and tunable catalysts.

Compared with conventional electrochemical measurements, the AP-XPS method described here is free of complications associated with the introduction of reference electrodes into solid oxide devices. More importantly, this technique provides specific local overpotential information without the requirements of symmetric cell design or complicated circuit simulations.

Chapter 3

Water Electrolysis and Hydrogen Electro-Oxidation on Ceria-Based Solid Oxide Electrochemical Cells

3.1 Introduction

Understanding the mechanisms of charge separation and charge transfer at electrochemical interfaces is essential for the rational development of electrochemical devices, such as batteries, fuel cells, electrolyzers, and chemical capacitors.^{87,88} The close alignment of charge donor and acceptor states is required for efficient charge exchanges.⁸⁸ Surface science techniques can be ideal tools to address these questions. However, most surface science studies are currently conducted on model cells under ultrahigh vacuum (UHV) and equilibrium conditions. This situation leads to the concern that whether the knowledge obtained from these ideal conditions can be employed in the materials and operating conditions for real world applications, which is usually referred to as the “pressure and materials gap”^{89–91}. This disconnect is particularly problematic with high temperature electrochemical energy conversion devices with multicomponent materials (*e.g.*, solid oxide fuel cells, electrolyzers, and electrocatalytic fuel processors)⁹² for which *in situ* or *operando* surface experiments at cell operating temperatures (typically >500 °C) are challenging.⁹³

Because of the experimental constraints of most surface science experiments, the knowledge and understanding of the surface processes at relevant conditions are limited and rely on extrapolations from UHV conditions and modeling studies.⁹⁴ As a

result, the electrochemical surface processes are not well understood. For example, the non-Faradaic electrochemical modification of catalytic activity (NEMCA or EPOC)⁸⁶ can significantly enhance the rates of catalytic transformation of over 100 reactions,^{89,95} yet the origins of this enhancement are not fully understood.⁸⁹ Even the mechanism of simple hydrogen electro-oxidation and water electrolysis on oxide surfaces of solid oxide electrochemical cells remains controversial with regard to the presence or absence of a double layer (dipole layer) at the gas-solid interface and the rate limiting processes on the oxide surfaces.⁹⁶

Mixed-ionic-electronic-conducting (MIEC) materials such as cerium oxide^{31,92,97} are the focus in these investigations because of their well-documented catalytic and electrocatalytic properties as well as their ability to extend the electrochemically active region beyond the three-phase boundary (TPB)^{56,80}. The catalytic behavior of ceria is directly linked to its accessible mixed valence $\text{Ce}^{3+}/\text{Ce}^{4+}$ redox states, its oxygen storage capacity⁹², and the surface vacancy concentrations⁹⁸. Recent *in situ* studies on ceria and doped ceria have shown that surface oxygen vacancies are either linked to underlying Ce^{3+} ions or clustered around Ce^{3+} ions when vacancy concentrations are high.^{98,99} While the oxygen mobility and catalytic behavior of ceria have been directly linked to the surface oxygen vacancy concentration,⁹⁸ the mechanisms of catalysis and electrocatalysis remain largely unknown.

Chapter 2 has described how ambient pressure X-ray photoelectron spectroscopy (AP-XPS) can be utilized to monitor changes in Ce oxidation states in cerium oxide electrodes, measure local surface potentials across an entire solid oxide

electrochemical cell (SOC), and measure local overpotentials on operating SOC devices in far-from-equilibrium conditions.^{56,80} These studies laid the groundwork for performing *in situ* or *operando* mechanistic studies designed to “observe” changes in chemical intermediates involved in the electrochemical process.

This chapter presents the observations of transient intermediates accumulating in the active region of an operating ceria SOC as a result of rate-limiting charge transfer processes. In both water electrolysis and hydrogen electro-oxidation reactions the same electrochemical step, $\text{H}_2\text{O} + \text{Ce}^{3+} \leftrightarrow \text{Ce}^{4+} + \text{OH}^- + \text{H}^+$, appears to be rate limiting. This mechanistic insight is obtained from monitoring the build-up of Ce^{3+} and hydroxyl (OH^-) at positive and negative biases, respectively. In addition, a separation of local surface potentials of the adsorbed OH^- and incorporated O^{2-} ions is observed due to the change in surface Ce^{3+} coverage. The chemical origin of the potential separation of $\text{OH}^-/\text{O}^{2-}$ resides in the reduced polarization of the Ce-OH bond due to the Ce^{3+} build-up. This charge separation can be viewed as the effective double layer at an electrochemical gas-solid interface^{67,95} and interpreted in the context of Fleig’s description of surface potential steps on MIEC electrodes⁶⁷. These results provide insight into the high temperature surface chemistry on MIEC ceria electrodes.^{21,22,31,100,101}

The work described here has involved close collaboration with Dr. Chunjuan Zhang, Professor Zhi Liu, and his research team at ALS. My contribution includes fabricating a series of zirconia-based SOCs having dense ceria working electrodes, performing the XPS measurements at ALS, analyzing XPS spectra by using the CasaXPS software, and further interpreting the results.

3.2 Experimental

3.2.1 Solid Oxide Electrochemical Cell Preparation

A detailed description of cell fabrication and characterization methods is provided in Chapter 2. A brief overview is given here. Ytria-stabilized zirconia (YSZ) powder of 8 mol% was purchased from Tosoh Inc. and was pressed in a coaxial stainless steel die-press. The as-pressed YSZ pellets were cut into square supports, heated to 1450 °C (1 °C/min), and sintered for 3 h. Aluminum oxide (Al₂O₃), Au, and Pt electrodes were sputter-deposited with patterned stainless steel shielding masks (FotoFab). The thicknesses of the sputtered Al₂O₃, Au, and Pt films were 30, 300, and 300 nm, respectively. Ceria films were sputter-deposited under 5 mTorr of O₂/Ar gas mixture containing 10% O₂. The ceria film was prepared as 800-nm-thick for this study. All samples were pre-annealed at 800 °C for 3 h before electrochemical and XPS measurements.

The film thicknesses were evaluated using a Hitachi SU-70 analytical ultrahigh resolution scanning electron microscope (SEM). **Figure 3-1** shows the cross-sectional SEM image of the 800-nm-thick ceria electrode.

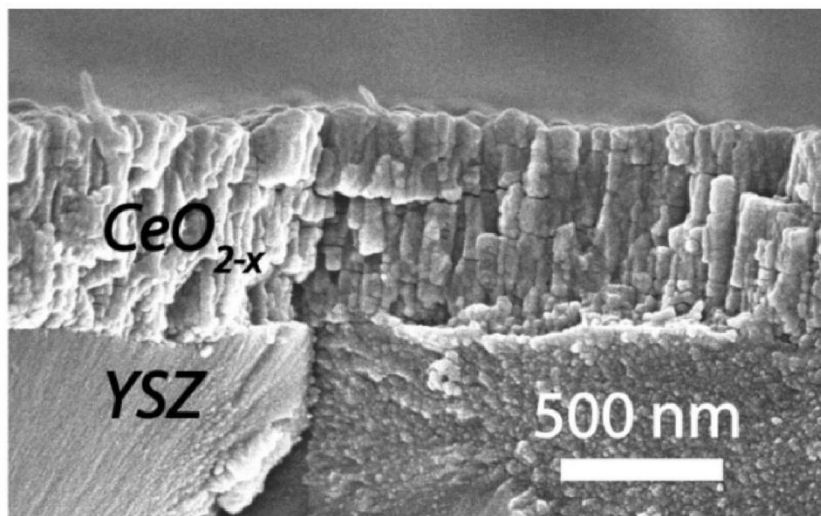


Figure 3-1. Cross-sectional SEM image of a fractured cell showing the ~800 nm CeO_{2-x} film deposited on the YSZ electrolyte.

3.2.2 Electrochemical Measurements

Electrochemical characterization of two-probe linear sweep voltammetry (LSV) and electrochemical impedance spectroscopy (EIS) measurements were conducted by using a Bio-Logic potentiostat. The single-chamber cells were clamped onto a ceramic heater and loaded into the AP-XPS end-stations⁷⁷ at beamline 9.3.2 and 11.0.2 of the Advanced Light Source (ALS) at Lawrence Berkeley National Laboratory (LBNL). The spring-loaded probes of the cell mounting platen served as both clamps and electrical contacts/current collectors for electrodes (**Figure 2-2**).⁷⁸ In the experiments, H₂ and H₂O were sequentially leaked into the XPS chamber with a total pressure of 0.5 Torr. Once the gas mixture stabilized at the target pressure, the cell was heated to approximately ~720 °C. Temperatures were normalized to external pyrometer measurements by the bulk resistance values from impedance data.

In each experiment the Au current collector of the working electrode (WE) was always grounded to the XPS chamber ($V_{Au} = 0.0$ V) and the Pt counter electrode

(CE) was biased by the potentiostat.^{56,79} Hence, the overall cell bias V_{Cell} is defined as the potential difference between the Pt CE and the WE Au current collector: $V_{\text{Cell}} \equiv V_{\text{Pt}} - V_{\text{Au}}$, which simplifies to $V_{\text{Cell}} = V_{\text{Pt}}$ in this study.

3.2.3 *Operando* Ambient Pressure X-ray Photoelectron Spectroscopy

Measurement

Detailed descriptions of the AP-XPS measurements can be found in Chapter 2. A brief overview is given here. *Operando* AP-XPS measurements were conducted simultaneously with the electrochemical characterizations at ~ 700 °C with 0.5 Torr of 1:1 H₂/H₂O gas mixtures. Two-dimensional (2D) AP-XPS spectral maps (binding energy versus position) were obtained by using the differentially pumped electron analyzer^{77,78} installed at beamline 9.3.2 of the ALS at LBNL.⁷⁷ The sample was oriented such that the X-ray incident angle was 75 ° and the electron emission angle was 0 ° with respect to the sample normal. The photon energy used for Ce 4d was 490 eV and for O 1s was 650 eV. The binding energy values (BE) calibrations of Ce 4d were made by referencing against the bulk Au 4f_{7/2} peak (BE = 84.0 eV⁴²) collected with 490 eV photon energy.

Analysis of the 2D XPS intensity maps was obtained by slicing the XPS intensity maps into 20- μm segments against the axis of position.^{30,56,80} CasaXPS software (Version 2.3.15) was used for data analysis. After subtracting a Shirley background, each slice was fitted using a nonlinear, least squares routine with mixed Gauss-Lorentz function of 70% Gaussian and 30% Lorentzian.

3.3 Results & Discussions

The single-sided polycrystalline YSZ cell contains one 300-nm-thick Pt counter electrode (CE) and two CeO_{2-x} working electrodes (WEs) with 300-nm-thick Au current collectors. The Al_2O_3 films underneath each of the Au films block ionic transport between YSZ and Au.⁸¹ By blocking the O^{2-} transport into the Au pad, the electrochemical side reactions on the Au current collector are precluded. Dense thin ceria films of 800-nm-thick are patterned on top of the Au leaving elongated Au pads exposed for electric connections (**Figure 3-2**). Approximately 500 μm regions of the ceria film has direct contact with the supporting YSZ electrolyte, allowing O^{2-} ions move across the CeO_{2-x} -YSZ interface. This cell geometry with the ceria WE and Pt CE deposited on the same side of the YSZ electrolyte support allows full access to all cell component surfaces for XPS studies.

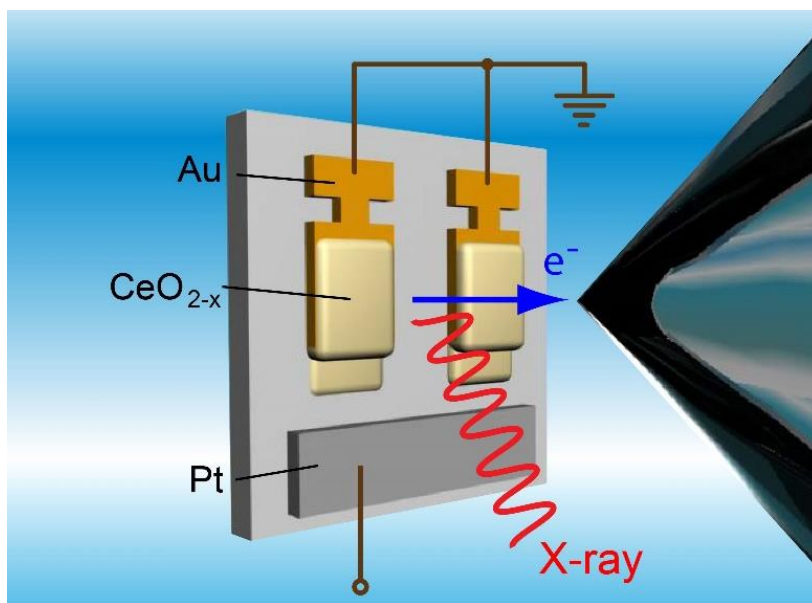


Figure 3-2. Schematic drawing (not to scale) of the solid oxide electrochemical cell (SOC) assembly. An Al_2O_3 blocking layer is sputtered underneath the entire Au pad (not shown) to block the ionic transport pathway between YSZ and Au.

Since both the CeO_{2-x} WE and the Pt CE are exposed to the same gas environment of 0.5 Torr of 1:1 H₂/H₂O ~700 °C, no thermodynamic driving force exists when the electrochemical reactions on both electrodes reach equilibrium with the gas phase. This situation results in a near-zero open-circuit voltage (OCV). At OCV, the cell surfaces reach thermal equilibrium with the H₂ and H₂O gases as described by the following reactions:



On the ceria electrode electrons locate at Ce sites and reduce Ce⁴⁺ to Ce³⁺ as described by the polaron hopping mechanism (see Chapter 1, Section 1.2.5). When Ce^{3+/4+} species and oxygen vacancy sites (V_O) on the ceria electrode are taken into consideration, the above equation can be written as:



As discussed in Chapter 1, Section 1.2.5, that ceria behaves as a mixed-ionic-electronic-conducting (MIEC) material under low oxygen partial pressure conditions due to the presence of oxygen vacancy and partial reduction of Ce⁴⁺ to Ce³⁺. The low gas pressure of 0.5 Torr in this study satisfies this situation. Therefore, under positive or negative bias, ceria allows electric current pass across the SOC by exchanging electrons with the Au current collector and O²⁻ with the YSZ electrolyte support. Specifically, at positive bias ceria functions as a cathode and promotes H₂O electrolysis reactions, while Pt acts as an anode and promotes H₂ electro-oxidation. At negative bias, the roles of the electrodes are reversed such that H₂O electrolysis occurs on Pt and H₂ electro-oxidation occurs on ceria (**Figure 2-4**).

Figure 2-4 shows a schematic illustration of the electrochemistry reactions occurring on the specially designed single-sided ceria-based SOC under positive and negative biases. A positive potential applied on the Pt electrode drives electrons from the Au pad to ceria, and moves O^{2-} from the ceria surface down to the YSZ and out to the Pt electrode. Under such conditions, **Eq. 3-2** is driven away from the equilibrium, and is favored in the forward directions. As such, the positive bias promotes H_2O electrolysis on the ceria electrode surface and H_2 electro-oxidation reactions are promoted at the Pt-YSZ interface. The H_2O electrolysis process on CeO_{2-x} is illustrated in **Figure 3-3**. When the bias is reversed (negative bias on Pt), the surface reactions occur in the opposite direction to give H_2 electro-oxidation over ceria and H_2O electrolysis at the Pt-YSZ edge.

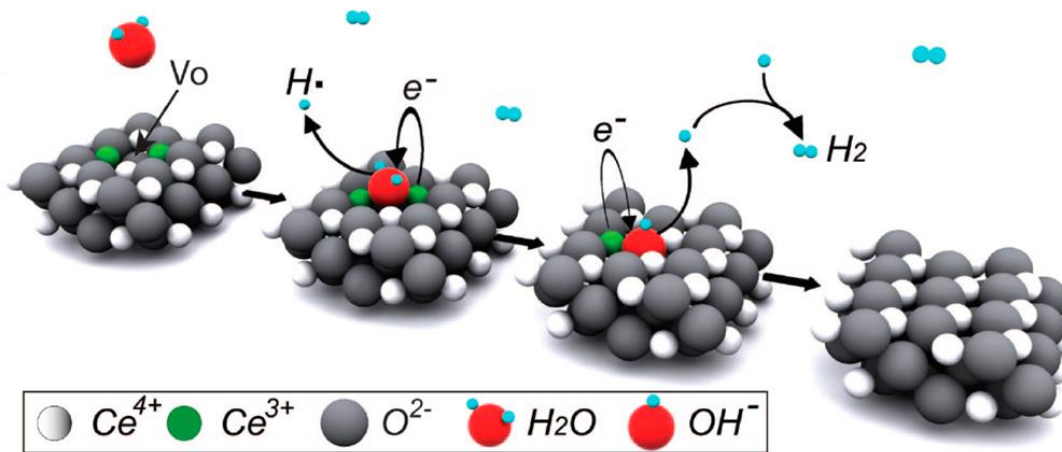


Figure 3-3. Proposed surface electrochemical reaction mechanism under positive applied bias. H_2O splitting reactions occur on CeO_{2-x} electrodes. V_O is an oxide vacancy on the CeO_{2-x} surface. For clarity, the surface H atoms were drawn above the electrode surface.

3.3.1 Electrochemistry Characterization

Figure 3-4 shows the electrochemical characterization of linear sweep voltammetry (LSV) from -1.2 V to +1.2 V on the 800-nm-thick ceria-based SOC. The cell currents that correspond to H₂O electrolysis on ceria ($V_{\text{Pt}} > V_{\text{Au}}$) are significantly higher than those of H₂ electro-oxidation ($V_{\text{Pt}} < V_{\text{Au}}$). As discussed in Chapter 2, this higher cell current at positive bias is due to, on one hand, the smaller overpotential associated with H₂O electrolysis (versus H₂ electro-oxidation) on ceria, and on the other hand the higher affinity of H₂ on Pt as well as the simultaneous oxygen spillover and hydrogen spillover effect (see Chapter 2, Section 2.3 for more details). Also, the lower electronic conductivity of ceria at negative bias can also be responsible for the lower currents at these conditions.

EIS measurement under OCV condition is shown in **Figure 3-5**. The electrolyte bulk resistances is obtained from the high frequency intercepts of EIS Nyquist plots. Typically, the electrolyte bulk resistance at 700 °C is within the range of 350 - 400 Ω.

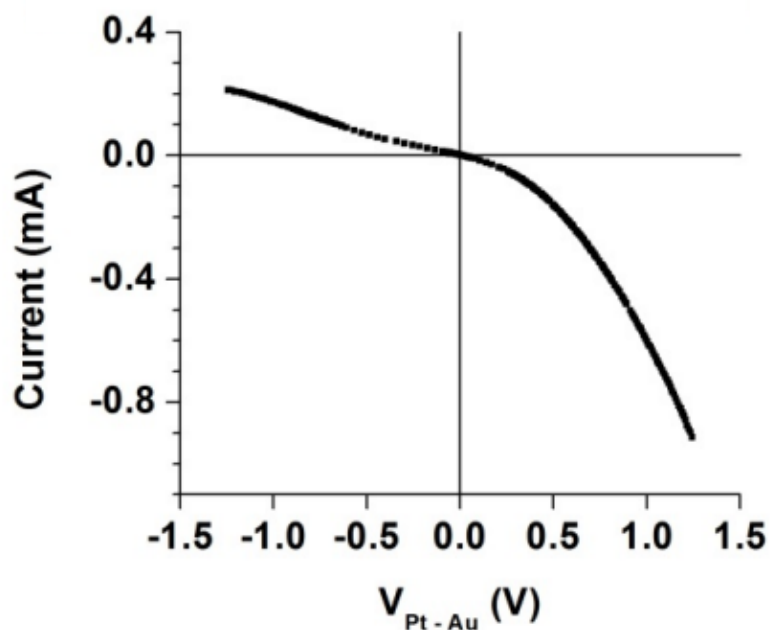


Figure 3-4. Electrochemical linear sweep voltammetry (LSV) collected on the SOC with an 800-nm-thick ceria electrode under conditions of ~ 700 °C, 0.5 Torr 1:1 H₂/H₂O mixture.

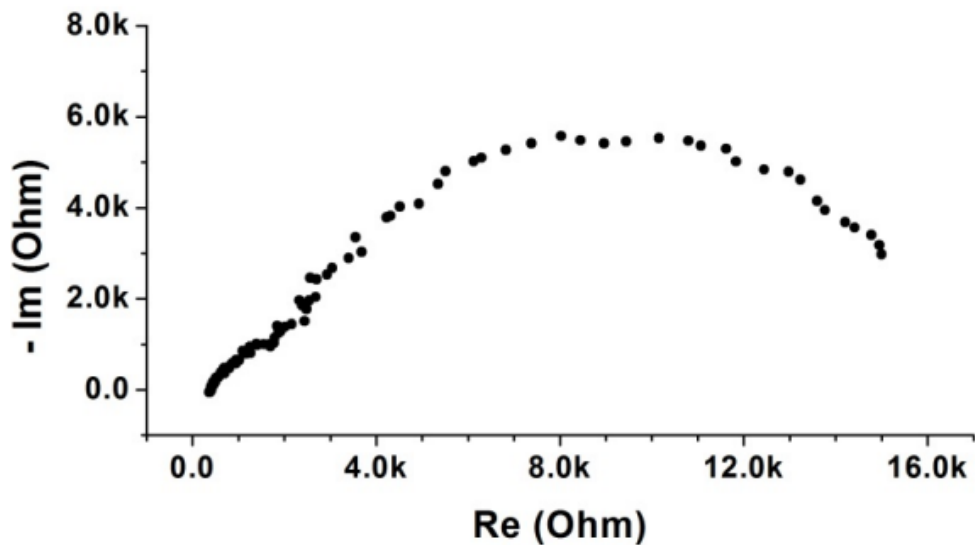


Figure 3-5. Electrochemical impedance spectroscopy (with 10 mV AC oscillating amplitude at zero DC applied bias) recorded on the SOC with an 800-nm-thick ceria electrode under conditions of ~ 700 °C, 0.5 Torr 1:1 H₂/H₂O mixture.

3.3.2 Surface Hydroxyl Intermediates

The surface bias and surface concentrations of OH^- and O^{2-} on an 800-nm-thick ceria electrode are determined through *operando* measurements of the O 1s XPS spectra. **Figure 3-6** shows the second derivative of two-dimensional (2D) O 1s XPS intensity spectral maps in the active region of ceria electrode at +1.2 V applied bias. The three observed peaks are attributed to lattice O^{2-} in the CeO_{2-x} electrode (~ 528 eV), the surface OH^- (~ 529.7 eV)¹⁰², and gas phase H_2O (533.8 eV) in front of the aperture⁴⁴. Depth profile studies³⁰ of the O 1s spectra confirm that the OH^- species (BE ≈ 529.7 eV) are present on the surface of the CeO_{2-x} electrode while the O^{2-} signal represents an average of the O^{2-} ions in the solid electrode phase at the near surface region.

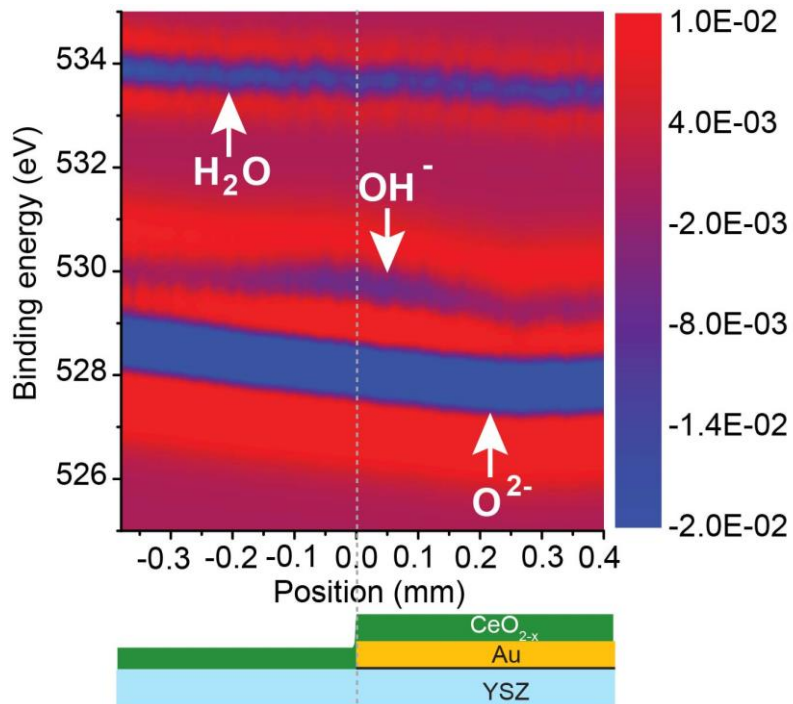


Figure 3-6. Spatially resolved second derivative of the two-dimensional O 1s spectra collected under +1.2 V applied bias (~ 700 °C with 0.5 Torr of 1:1 $\text{H}_2/\text{H}_2\text{O}$ mixtures). The horizontal axis is the position on the cell surface.

The BE values of O 1s spectra presented here are referenced to the valence band maximum, which is ~ 2 eV below the Fermi level. Since only the relative BE shifts between different O 1s peaks are of interest, the absolute BE values of different O 1s peaks are not important in this study. Generally, the O 1s BEs of OH⁻, O²⁻, and gas phase H₂O here are 2 eV less than the BE values found in literature^{44,102}, which are typically referenced to the Fermi level (see Chapter 1, Section 1.3.2 for more detailed discussion).

The spatially resolved individual XPS spectra is obtained by taking one-dimensional slices from the 2D intensity spectral maps. The peak fitting of a typical O 1s spectrum is shown in **Figure 3-7**.

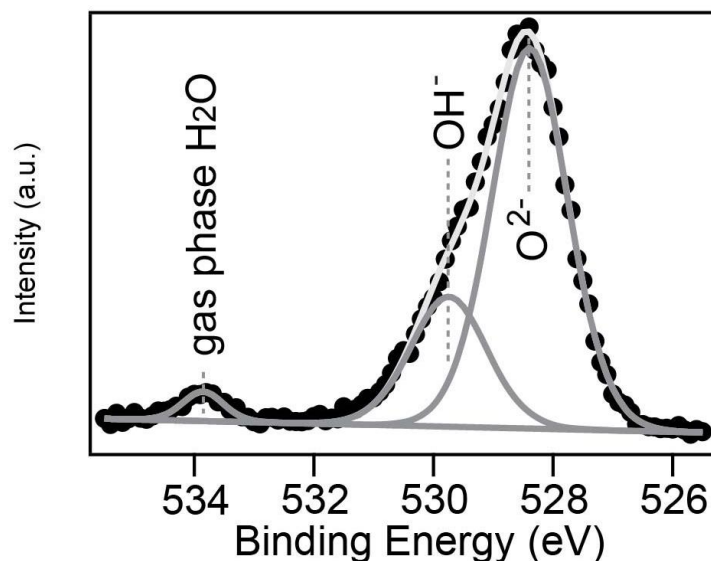


Figure 3-7. One representative 20- μm slice of O 1s spectra at $x = -0.155$ nm under +1.2 V (~ 700 °C with 0.5 Torr of 1:1 H₂/H₂O mixtures), fitted with gas-phase H₂O, OH⁻ surface adsorbates, and solid-phase O²⁻ species.

3.3.3 Local Surface Potential Shifts of Hydroxyl and Oxide Ion

As discussed in Chapter 2 (Section 2.1.1), the magnitude of binding energy shift under biased and non-biased conditions is related to the local surface potential (V_L) as: $\Delta BE = -e \cdot V_L$. This binding energy shift stems from the change in the local Fermi level (see **Figure 1-13**).^{56,73-76} Thus by measuring ΔBE of photoelectrons of selected elements on the cell surface, the local surface potential information at that position can be directly assessed,⁷³⁻⁷⁶ which provides a direct and contactless measure of local surface potentials in SOCs. (See Section 2.1.1 for more detailed discussion.)

Analysis of the 2D XPS data collected under an applied bias can give a map of the spatially resolved V_L data of all atoms on the SOC surface. **Figure 3-8** shows how the local surface potentials of OH^- and O^{2-} shift under applied biases across the electrochemically active region of the ceria electrode.

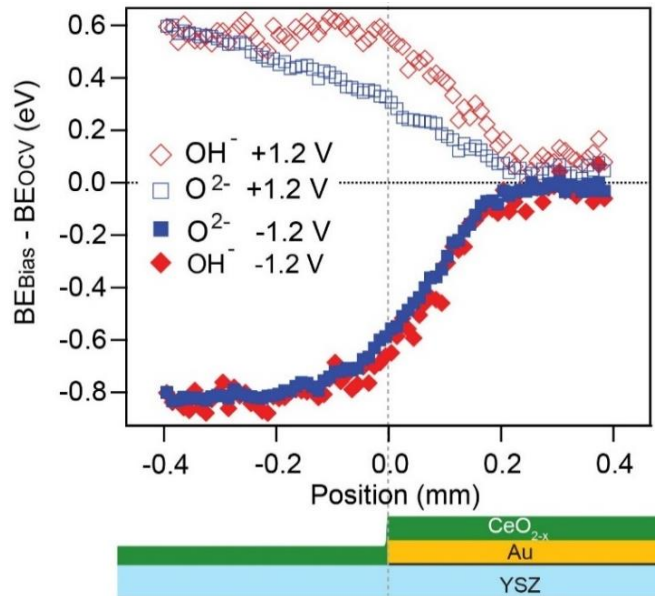


Figure 3-8. Relative shifts in apparent BE under applied bias (± 1.2 V) away from OCV for OH^- and O^{2-} peaks (~ 700 °C with 0.5 Torr of 1:1 $\text{H}_2/\text{H}_2\text{O}$ mixtures). The local potential difference between OH^- and O^{2-} represents the difference of surface potential steps ($\Delta\chi$).

As demonstrated in Chapter 2 (**Figure 2-8**), the local surface potential values for all of the surface species (*i.e.*, OH⁻, O²⁻, Ce³⁺, Zr⁴⁺) shift by the same amount across the SOC surface if they locate outside of the electrochemically active region of ceria. However, when H₂O splitting reactions are promoted on ceria (+1.2 V bias) the local surface potential values for OH⁻ and O²⁻ within the electrochemically active region are significantly different on the CeO_{2-x} surface (**Figure 3-8**). At the same time, the Ce³⁺/Ce⁴⁺ ratios are also driven away from equilibrium, showing a large increase in surface Ce³⁺ concentration in the same region (Ce 4d XPS spectra shown below, **Figure 3-11**). Outside the active region, the V_L values for OH⁻ and O²⁻ once again become equivalent and the Ce³⁺/Ce⁴⁺ ratios maintain their equilibrium values.

At negative bias when H₂ electro-oxidation is promoted on ceria, the V_L values for OH⁻ and O²⁻ show a very small but discernible divergence in the opposite direction (**Figures 3-8**).

This difference in the V_L values of OH⁻ and O²⁻ (V_{L(OH)} – V_{L(O)}) in the active region represent the local potential difference between the surface adsorbates and the ceria electrode. It is the build-up of surface Ce³⁺ in the active region that drives the separation of the potentials of OH⁻ and O²⁻.

3.3.4 Dipole Model

The divergence of the OH⁻ and O²⁻ surface potentials in the active region of the SOC can be illustrated by the dipole model¹⁰³⁻¹⁰⁵ at gas-solid interfaces^{106,107}. The chemisorbed OH⁻ ions are bonded to CeO_{2-x} on the SOC surface with natural bond dipoles, with the negative end pointing to OH⁻ oxygen and the positive end to the

$\text{Ce}^{3+}/\text{Ce}^{4+}$ ions (**Figure 3-9**). Under applied bias, **Eq. 3-2** shifts the concentrations of the charged surface species on either side of the dipole layer end, therefore, modifies the magnitude of the surface dipole.

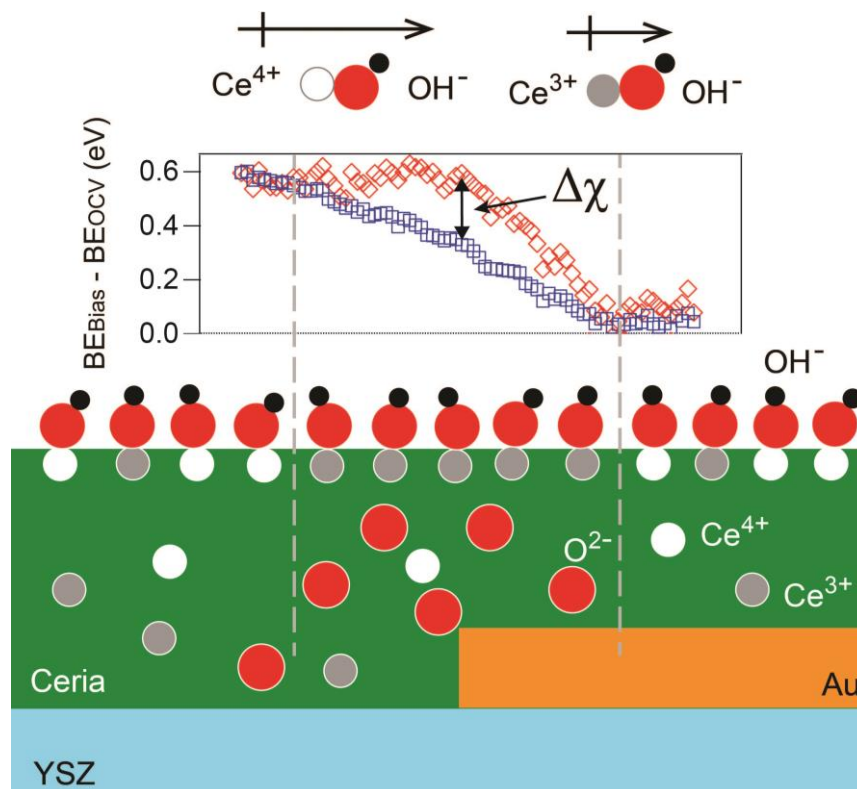


Figure 3-9. Schematic representation of bond dipoles for the Ce^{3+} -OH and Ce^{4+} -OH interactions on the CeO_{2-x} surface. The electrochemically induced build-up in Ce^{3+} concentrations results in a divergence in the local surface potentials of OH^- (red) and O^{2-} (blue) within the active region denoted by the dashed lines.

At +1.2 V applied bias, the $\text{OH}^-/\text{O}^{2-}$ concentration ratio show no change in the active region relative to the OCV equilibrium conditions (**Figure 3-10**). However, the large increase of surface Ce^{3+} ions (*i.e.*, polarons) in the active region (**Figure 3-11**) significantly reduce the magnitude of the dipole moment between the surface OH^- adsorbate and the electrode. This electrochemically driven reduction in bond polarization effectively decrease the local surface potentials values on the two sides

of the dipole layer. Specifically, the OH^- adsorbate, $V_{\text{L}(\text{OH})}$, is driven to a higher local potential than that of the CeO_{2-x} electrode surface directly beneath it (*i.e.*, the oxide potential, $V_{\text{L}(\text{O})}$, **Figure 3-8**). Consequently, the BE difference between OH^- adsorbates and electrode O^{2-} become larger than that of the OCV condition within the electrochemically active region (**Figure 3-12**). The correlation of surface Ce^{3+} build-up with divergence of $V_{\text{L}(\text{OH})}$ and $V_{\text{L}(\text{O})}$ values (**Figure 3-13**) further confirms the origin of this potential separation.

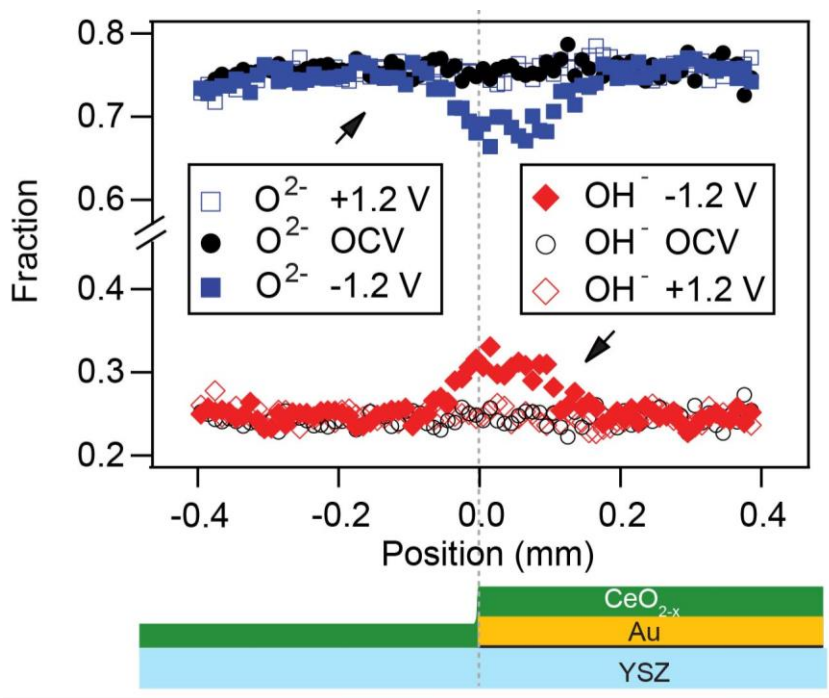


Figure 3-10. Fraction of OH^- and O^{2-} under OCV and +1.2 V applied biases extracted from O 1s XPS spectra ($\sim 700^\circ\text{C}$ with 0.5 Torr of 1:1 $\text{H}_2/\text{H}_2\text{O}$ mixtures).

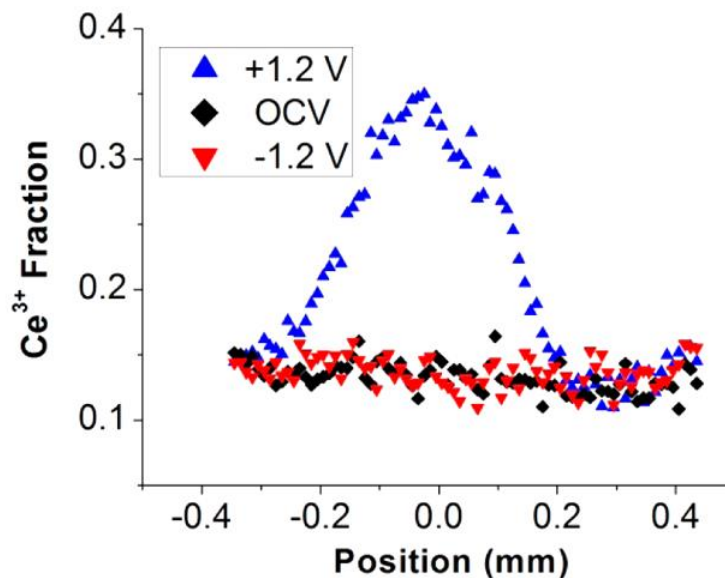


Figure 3-11. Spatially resolved Ce redox changes (Ce^{3+} fraction) calculated from fitted Ce 4d spectra under OCV and ± 1.2 V applied biases (~ 700 °C with 0.5 Torr of 1:1 $\text{H}_2/\text{H}_2\text{O}$ mixtures).

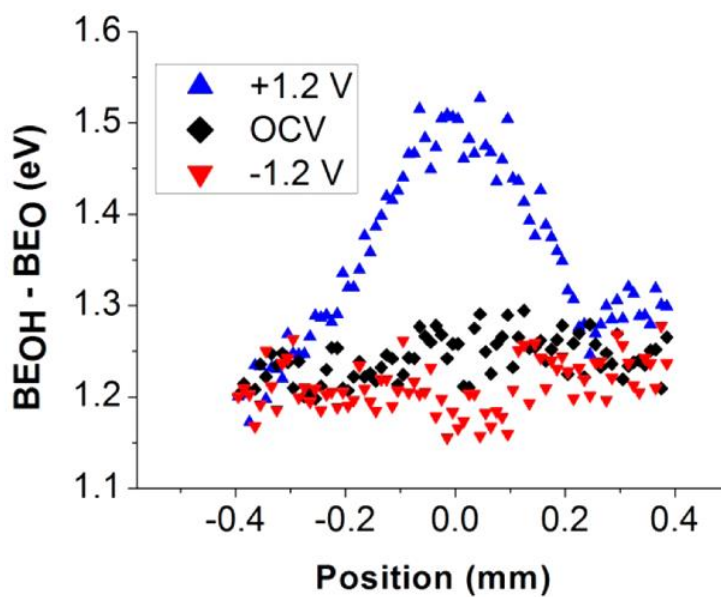


Figure 3-12. Spatially resolved BE separations (*i.e.*, surface potential steps) between surface OH^- adsorbates and solid phase of O^{2-} derived from O 1s spectra under OCV and ± 1.2 V applied biases (~ 700 °C with 0.5 Torr of 1:1 $\text{H}_2/\text{H}_2\text{O}$ mixtures).

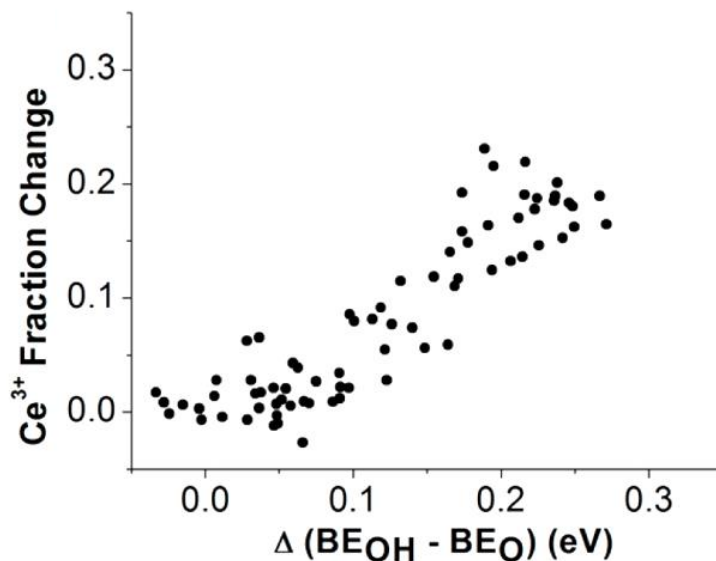
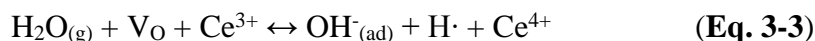


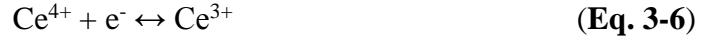
Figure 3-13. Correlation between Ce^{3+} fraction changes and surface potential step changes under +1.2 V applied bias relative to OCV ($\sim 700^\circ\text{C}$ with 0.5 Torr of 1:1 $\text{H}_2/\text{H}_2\text{O}$ mixtures).

The situation is substantially different at -1.2 V applied bias (H_2 electro-oxidation on ceria). Under negative bias, the ceria surface shows little change in $\text{Ce}^{3+}/\text{Ce}^{4+}$ ratios (**Figure 3-11**), but there is a small but significant increase in the OH^- adsorbate concentration in the active region with an accompanying decrease in surface O^{2-} concentration (**Figure 3-10**).

3.3.5 Rate-Limiting Process

Ce^{3+} and OH^- are both identified as surface intermediates in the ceria-catalyzed H_2 electro-oxidation and H_2O electrolysis reactions. Shifts in their steady-state concentrations provide insights into rate-limiting surface processes. At OCV condition, the CeO_{2-x} surface reach thermal equilibrium with the H_2 and H_2O gases as described by the following four basic exchange equilibria:





These four exchange reactions represent the interactions between H₂O and OH⁻ (Eq. 3-3), OH⁻ and O²⁻ (Eq. 3-4), and surface hydrogen atoms H[·] and H₂ (Eq. 3-5) and electron transport by way of polaron hopping (Eq. 3-6). Since there is no net current flow in the cell at OCV, the surface Ce redox states and the surface OH⁻ coverage adopt equilibrium concentrations dictated by the cell temperature and the gas partial pressures.

At -1.2 V, the accumulation of OH⁻ adsorbates in the active region indicate that OH⁻ consumption process is rate-limiting, *i.e.*, the reverse reaction of (Eq. 3-3) is a slow, rate-limiting process. At +1.2 V, the OH⁻ maintains its equilibrium concentration while the Ce³⁺ concentration increases significantly. The build-up of surface Ce³⁺ and the lack of changes in OH⁻/O²⁻ concentration ratio are also consistent with (Eq. 3-3) being a rate-limiting process. As such, these results suggest that the first step in H₂O electrolysis (H₂O + Ce³⁺ → Ce⁴⁺ + OH⁻ + H[·]) and the last step in H₂ electro-oxidation (Ce⁴⁺ + OH⁻ + H[·] → H₂O + Ce³⁺) are rate-limiting steps on the ceria-based SOC electrocatalysts described here. Increases in OH⁻ concentrations has also been observed in a related study¹⁰⁸ on YSZ electrolyte surfaces near the three-phase boundary (TPB) regions in polarized Pt-YSZ-Pt symmetrical electrolysis cells.

3.3.6 Surface Potential Step

The potential separation between OH⁻ and O²⁻ could also be described by the Fleig model⁶⁷ for SOC surface reactions associated with MIEC materials such as ceria

(Figure 3-14). This model highlights the differences between liquid-solid electrochemical interfaces described by classical Butler-Volmer kinetics and gas-solid electrochemical interfaces where double layers involved as reactant species. Central to the model is the existence of equilibrium surface potential step (χ^{eq}) describing the effective resistance to charge separation of reaction intermediates at a metal oxide electrode surface (e.g., $\text{OH}^-(\text{ad}) + \text{Ce}^{3+} \leftrightarrow \text{O}^{2-} + \text{H}\cdot + \text{Ce}^{4+}$). Physically, this resistance is equal to the difference between the local surface potentials of the adsorbates and the electrode under equilibrium conditions, described as the equilibrium surface potential step:

$$\chi^{eq} = V_{L(\text{ode})}^{eq} - V_{L(\text{ads})}^{eq} \quad (\text{Eq. 3-7})$$

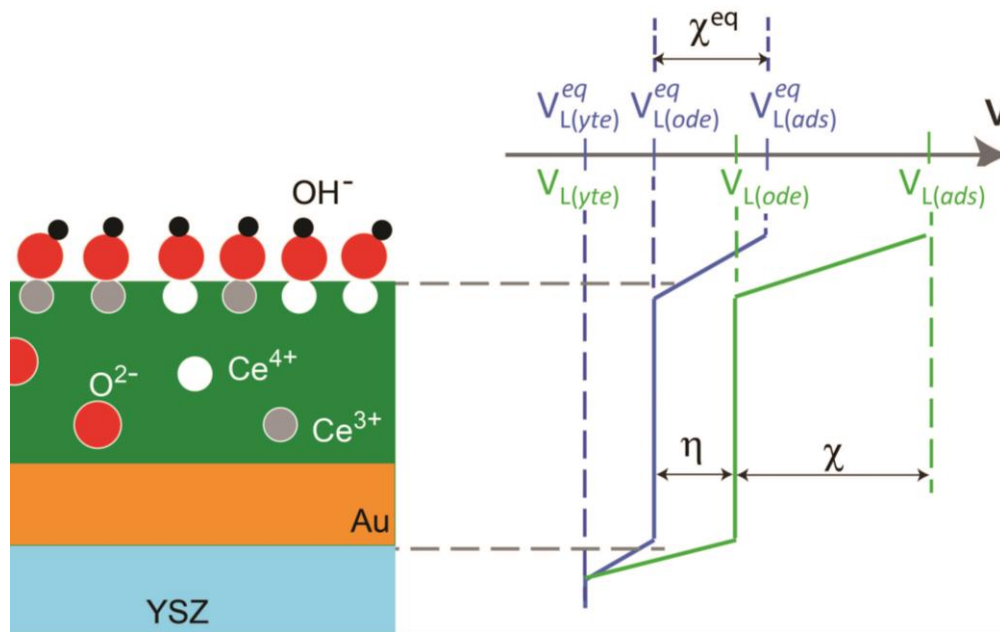


Figure 3-14. Interpretation of the potential losses across the gas-solid interface and CeO_{2-x} -YSZ interface showing the surface potential steps (χ) and the charge transfer overpotential (η). In the scheme, the local equilibrium potentials of the YSZ electrolyte, the ceria electrode, and hydroxyl adsorbate layers are shown in blue and are labeled $V_{L(\text{yte})}^{eq}$, $V_{L(\text{ode})}^{eq}$, $V_{L(\text{ads})}^{eq}$, respectively. The local potentials observed at an applied cell bias of +1.2 V are shown in green and denoted by $V_{L(\text{yte})}$, $V_{L(\text{ode})}$, $V_{L(\text{ads})}$, respectively. For simplicity, all of the local potentials are normalized to the equilibrium YSZ electrolyte potential.

In this study, **Eq. 3-7** can be written specifically as:

$$\chi^{\text{eq}} = V_{\text{L(O)}}^{\text{eq}} - V_{\text{L(OH)}}^{\text{eq}} \quad (\text{Eq. 3-8})$$

where $V_{\text{L(O)}}^{\text{eq}}$ and $V_{\text{L(OH)}}^{\text{eq}}$ are the local surface potentials of O^{2-} and OH^- under equilibrium OCV conditions, respectively. When the electrode is biased, a modified surface potential step (χ) is obtained that represents a shift from equilibrium conditions (**Figure 3-14**). The new χ is equal to the potential difference between the surface adsorbates and the electrode under applied bias:

$$\chi = V_{\text{L(ODE)}} - V_{\text{L(ads)}} = V_{\text{L(O)}} - V_{\text{L(OH)}} \quad (\text{Eq. 3-9})$$

As the difference between the potential step at equilibrium and that at bias is defined as $\Delta\chi = \chi - \chi^{\text{eq}}$:

$$\Delta\chi = (V_{\text{L(O)}} - V_{\text{L(OH)}}) - (V_{\text{L(O)}}^{\text{eq}} - V_{\text{L(OH)}}^{\text{eq}}) \quad (\text{Eq. 3-10})$$

Since the SOC in this study possesses a planar geometry that expose all cell components to both the fuel and the oxidant, there is no electric driving force under OCV equilibrium. The relationship of $V_{\text{L(O)}}^{\text{eq}} = V_{\text{L(OH)}}^{\text{eq}}$ is always valid over the ceria surface (as well as the YSZ surface). **Eq. 3-10** can be simplified to:

$$\Delta\chi = V_{\text{L(O)}} - V_{\text{L(OH)}} \quad (\text{Eq. 3-11})$$

Therefore, the measurement of the divergent V_{L} values for the OH^- and O^{2-} at +1.2 V, which represent the potential drop between the adsorbate ($V_{\text{L(OH)}}$) and the underlying CeO_{2-x} surface ($V_{\text{L(O)}}$), is a direct measurement of the surface potential step shift $\Delta\chi$. This shift in surface potential step drives the net electrochemical reactions and generates electric current.⁶⁷ $\Delta\chi$ is also a direct measure of the electrochemical double layer at the gas-solid interface.⁶⁷

In a traditional fuel cell, such as that described by Fleig (**Figure 3-14**), there is a finite equilibrium potential step (χ^{eq}) that describes the inherent resistance to surface charge separation resulting from the electrochemical potential of the cell. In this investigation, all equilibrium potentials are zero because OCV is 0.0 V in a single-sided cell, and as a result, $\Delta\chi = \chi$ in these experiments. The value of $\Delta\chi$ reaches a maximum of 0.25 V in the center of the active region (**Figure 3-8**). The correlation between surface Ce^{3+} concentrations and the magnitudes of $\Delta\chi$ (**Figure 3-13**) confirms that this surface potential step is related to the relative rates of oxygen supply and removal at the surface.

3.3.7 Surface Potential Step versus Activation Overpotential

The surface potential steps are different from activation overpotentials. Overpotentials describe barriers to net charge transfer across a double layer,^{109,110} whereas there is no net charge transfer associated with surface potential steps across the gas-solid interface. However, the changes in bond polarities and the resulting dipoles between surface adsorbates and the electrode surface form an effective double layer at the gas-solid interface, which modifies surface reactions involving charged species. The inherent coupling of reaction intermediate concentration shifts (*i.e.*, OH^- and Ce^{3+}) and surface potential steps must be included in an accurate kinetic description of gas-solid interfacial reactions involving charge exchange with the underlying surface, as described in Fleig's model.⁶⁷ For high-temperature SOC systems, *operando* surface studies are the only means of extracting such information, and the results described here provide a significant advance in these endeavors.

3.4 Summary

Investigations of water electrolysis and hydrogen electro-oxidation reactions on an operating CeO_{2-x}-based SOC are presented in this chapter. Transient intermediates are observed accumulating in the electrochemically active region as a result of rate-limiting charge transfer processes. In both H₂O electrolysis and H₂ electro-oxidation reactions over ceria electrocatalysts the same electrochemical step, $\text{H}_2\text{O} + \text{Ce}^{3+} \leftrightarrow \text{Ce}^{4+} + \text{OH}^- + \text{H}^\cdot$, appears to be rate limiting. Also, a separation of local surface potentials of the adsorbed OH⁻ and incorporated O²⁻ ions is observed due to the change in surface Ce³⁺ coverage.

These experiments provide a detailed picture of charge separation at a gas-solid interface of an operating electrochemical device. Similar to electrical double layers between the electrode and the electrolyte, the charge separation leads to an enormous electric field ($\sim 10^8$ V/m) within a small interface region that greatly affects surface reaction kinetics in electrochemically active materials and in particular oxides. The interplay between this enormous electric field and the chemical reactions at the interface is the essence of high-temperature solid-gas electrochemistry.¹¹¹

Chapter 4

Carbon Dioxide Activation and Carbonate Intermediates on Solid Oxide Electrochemical Cells

4.1 Introduction

4.1.1 Carbon Dioxide Reduction

The use of carbon dioxide as a chemical feedstock by way of chemical and electrochemical conversion has become an attractive area of research for the production of hydrocarbon compounds such as methane, methanol and carbon monoxide. For example, synthetic gas produced from CO₂ and natural gas (CO₂ + CH₄ ↔ 2CO + 2H₂) can be used as building blocks to yield hydrocarbon fuel via the Fischer-Tropsch synthesis process (nCO + (2n+1)H₂ → C_nH_(2n+2) + nH₂O).

However, CO₂ is an extremely stable molecule. Activating and reducing it to useful states require significant energy input and appropriate catalysts. For example, the reduction of CO₂ to CO (CO₂ → CO + $\frac{1}{2}$ O₂) is associated with a large positive enthalpy of 282.98 kJ/mol.¹¹² Recent reviews^{65,113,114} have examined the diverse approaches being pursued for CO₂ conversion. Direct use of heat can drive the dissociation of CO₂, but it requires extremely high temperatures since the thermolysis does not fully occur until 3000 - 4000 °C.⁶⁵ Thermochemical cycles, as another approach, allow splitting CO₂ at lower temperatures (< 2000 °C) than thermolysis. These cycles usually consist of two (or more) thermally driven chemical reaction

steps. The first step involves reducing a metal oxide and evolving oxygen gas ($\text{MO}_x \rightarrow \text{MO}_{x-\delta} + \frac{\delta}{2}\text{O}_2$), while the second step is oxidizing the metal or lower-valence metal oxide by reaction with CO_2 to produce CO ($\text{MO}_{x-\delta} + \delta\text{CO}_2 \rightarrow \delta\text{CO} + \text{MO}_x$). Although such high temperatures can be supplied by concentrated solar furnaces and a variety of electric furnaces, the extremely high temperature environment poses difficulty in these processes by requiring expensive materials that are stable at such high temperatures.⁶⁵ Also, difficult separations of the chemical intermediates and energy losses across multiple steps present challenges for these thermal processes.^{65,115}

Electrical energy can be used to dissociate CO_2 via electrolysis. Solution-based electrochemical reduction of CO_2 has been studied for decades and is still an active area of research.^{115,116} Aqueous and non-aqueous processes have been developed that utilize both bare electrodes and molecularly catalyzed approaches.^{115,116} Hori *et al.* summarized the structurally simple electrodes and classified them into four groups depending on the types of main products (*e.g.* hydrocarbon, CO, HCOO^- , or H_2).^{117,118} Recent advances in homogeneous electrocatalyst has been reviewed by Benson¹¹⁵, which cover metal catalysts with macrocyclic ligands, metal catalysts with bipyridine ligands, and metal catalysts with phosphine ligands. These methods are attractive in that reaction pathways can be tuned through catalyst design and a variety of products can be obtained. However, the high overpotential required to drive the reaction, the consequent slow kinetics (especially at low temperatures), and the complexity of the reactions in solution often lead to very complicated analysis.⁶⁵

The use of solid oxide CO₂ electrolysis cells was first pursued by the National Aeronautics and Space Administration (NASA) for oxygen production from the CO₂-rich Martian atmosphere.¹¹⁹ A solid oxide electrolysis cell of non-porous yttria-stabilized zirconia (YSZ) electrolyte in conjunction with Pt electrodes was described in their study.¹¹⁹ More recent systems analysis suggests that high temperature molten carbonates and solid oxide electrolysis are promising approaches for CO₂ reduction.^{65,120} A smaller portion of electricity is needed to dissociate CO₂ due to the thermodynamic advantages provided by the elevated temperature environment. Also, the faster reaction kinetics at high temperatures reduces the need for using expensive catalyst.^{65,120}

Electrode development is one of the current interests in solid oxide electrolysis cells for high temperature CO₂ reduction. In addition to advances in the original Pt/YSZ electrode NASA design¹¹⁹, new cathode materials have been investigated such as Ni and Cu-based YSZ systems^{120–122}, lanthanum strontium chromium manganite (LSCM)^{122,123}, and more recently doped ceria-based systems^{124,125}. Zhan *et al.* described the investigation of CO₂ electrolysis carried out on Ni-YSZ electrode-supported solid oxide fuel cells (SOFCs).¹²¹ Their results indicated that Ni-YSZ electrodes were highly effective for the electrochemical reduction of CO₂ to CO. Electrochemical measurements by Yue *et al.* revealed the cathode of LSCM/gadolinium doped ceria (GDC) exhibited good durability in CO₂ electrolysis operation and enhanced cathode activity due to the reduction of GDC.¹²² Green *et al.* showed that GDC systems have significantly lower polarization resistances relative to the Pt-YSZ based cathode systems and also outperformed the

Ni-YSZ systems.¹²⁴ While there has been a marked increase in performance of the past decade, the mechanistic origins of these enhancements and the basic surface chemistry are still not fully understood.

4.1.2 Ceria-Based Solid Oxide Electrolysis Cells

Cerium oxide is an excellent catalyst for three-way conversion reactions, water-gas shift reactions and steam reforming of methane due to its high oxygen storage capacity and kinetically facile changes between Ce^{3+} and Ce^{4+} states at low effective O_2 partial pressure (Chapter 1, Section 1.2.5). As a mixed ionic and electronic conducting (MIEC) material under low $P_{\text{O}_2, \text{eff}}$, ceria-based materials have been extensively studied for solar thermochemical cycles^{126–129}, SOFCs^{22,23,130} and solid oxide electrochemical cells (SOCs)^{21,30,56,80}.

In non-electrochemical thermal studies, the activation of CO_2 on ceria-based catalysts has been reported to require the formation of carbonate species as the first reaction step.^{131,132} Density functional theory (DFT) studies for CO_2 activation on oxidized and reduced ceria (110) surfaces suggested that CO_2 conversion to CO on reduced CeO_{2-x} was favored on a split oxygen vacancy through the formation of a unidentate carbonate intermediate.¹³³ This reaction pathway showed subtle differences in activation energies from other pathways.¹³³ However, photoelectron spectroscopic studies by Staudt *et al.* suggested that a surface carboxylate (defined as $\text{Ce-CO}_2^{\delta-}$ with a Ce-C bond) was the actual reaction intermediate during CO_2 -induced re-oxidation of CeO_{2-x} , while the relatively more stable surface CO_3^{2-} suppressed the formation of the active carboxylates.¹³⁴ By examining CO oxidation over ceria nanocrystals through oxygen isotopic exchange and *in situ* infrared and Raman

spectroscopy, Wu *et al.* concluded that the majority of the CO_3^{2-} species under steady state CO oxidation were reaction spectators, with only a fraction of the CO_3^{2-} species functioning as reaction intermediates.¹³⁵

4.1.3 Scope of the Chapter

Due to the lack of *in situ* and *operando* probing techniques at elevated temperatures and high pressures, and the complexity of the redox reactions that comprise several elementary steps, it is challenging to obtain a detailed mechanistic understanding of the ceria-based reactions with CO_2/CO reactants. Ambient pressure X-ray photoelectron spectroscopy (AP-XPS) has already been demonstrated as an effective approach in providing insights into reaction kinetics and mechanisms on operating SOCs in these challenging conditions in previous chapters (Chapter 2 and Chapter 3) and publications.^{30,56,80,136} In this chapter, a mechanistic, *operando* AP-XPS investigation of CO_2 electro-reduction and CO electro-oxidation on a single-sided ceria catalyzed SOC is described. Although studies on these specially designed SOCs are not identical to those on real SOFCs and solid oxide electrolysis cells (SOECs) that separate the fuel and the oxidant into two compartments, mechanistic information obtained from investigations of the SOCs is directly related to the chemical processes in SOFCs and SOECs.

From simultaneous electrochemical measurements and XPS studies on the ceria-based SOCs, an increase in steady-state concentration of the carbonate intermediates is observed during CO_2 electrolysis within a 400- μm active region, accompanied by Ce redox changes. In the case of CO electro-oxidation, a small decrease in CO_3^{2-} concentration is detected. These results, combined with kinetic

analysis, provide mechanistic insight into the ceria catalyzed CO/CO₂ electrochemical reactions. In sum, the reaction intermediate species of CO₃²⁻ is identified in CO₂ electrolysis and CO electro-oxidation reactions on ceria electrode surfaces, and the charge transfer step to/from CO₃²⁻ is revealed as a rate-limiting process in both reaction directions. The work described here involves close collaboration with Professor Zhi Liu and his research team at ALS.

4.2 Experimental

4.2.1 Solid Oxide Electrochemical Cell Preparation

Detailed descriptions of cell fabrication and characterization methods are provided in Chapter 2. A brief overview is given here. 8 mol% YSZ powder from Tosoh Inc was pressed and cut into square pellets and fired at 1450 °C for 3 h. Aluminum oxide (Al₂O₃), Au, and Pt electrodes were sputter-deposited using patterned shielding masks. Thicknesses of the Al₂O₃, Au, and Pt films were 30, 300, and 300 nm, respectively. Ceria films were sputtered-deposited under 5 mTorr of O₂/Ar gas mixture containing 10% O₂. Approximately 1000-nm-thick ceria films were sputtered for this study. Samples were pre-annealed at 800 °C for 3 h before electrochemistry or XPS testing.

4.2.2 Electrochemical Measurements

Details describing the electrochemical measurements can be found in Chapter 2. A brief overview is given here. Electrochemical characterization of two-probe linear sweep voltammetry (LSV) and electrochemical impedance spectroscopy (EIS)

measurements were conducted by using a Bio-Logic potentiostat. The single-sided cells were clamped onto a ceramic heater. The spring-loaded probes of the cell mounting platen served as both clamps and electrical contacts/current collectors for electrodes (**Figure 2-2**).⁷⁸ In the experiments, 1:20 mixture of CO and CO₂ were leaked into the XPS chamber with a total pressure of 0.5 Torr. The cell was then heated to approximately 600 °C. The Au current collector of the working electrode (WE) was always grounded to the XPS chamber ($V_{\text{Au}} = 0.0 \text{ V}$) and the Pt counter electrode (CE) was biased by the potentiostat (**Figure 4-1**).^{56,79} Hence the overall cell bias V_{Cell} is defined as the potential difference between the Pt CE and the WE Au current collector: $V_{\text{Cell}} \equiv V_{\text{Pt}} - V_{\text{Au}}$, which simplifies to $V_{\text{Cell}} = V_{\text{Pt}}$ in the electrochemical cells in this study.

4.2.3 *Operando* Ambient Pressure X-ray Photoelectron Spectroscopy Measurement

Details describing the *operando* AP-XPS measurement can be found in Chapter 2. A brief overview is provided here. *Operando* AP-XPS measurements were conducted simultaneously with the electrochemical characterizations at ~600 °C with 0.5 Torr of 1:20 CO/CO₂ gas mixtures. The sample was oriented inside the end-station analysis chamber such that the X-ray incident angle was 75 ° and the electron emission angle was 0 ° with respect to the sample normal. The photon energy used for C 1s and Ce 4d was 490 eV and for O 1s was 650 eV. The binding energy (BE) calibrations were made by referencing against the bulk Au 4f_{7/2} peak (BE = 84.0 eV⁴²) collected with 490 eV photon energy.

Analysis of the two-dimensional (2D) XPS intensity maps was obtained by slicing the XPS image spectra into 20 or 60- μm segments against the axis of position.^{30,56,80} CasaXPS software (Version 2.3.15) was used for data analysis. After subtracting a Shirley background, each slice was fitted using a nonlinear, least squares routine with mixed Gauss-Lorentz function of 70% Gaussian and 30% Lorentzian. An asymmetric line shape was introduced to precisely fit the graphitic carbon peak in the C 1s region. In order to accurately reflect the relative intensities of the respective features, the integrated spectrum were normalized to the intensity of the gas phase CO₂ peak after background subtraction.

4.3 Results & Discussions

The single-sided polycrystalline YSZ cell contains one 300-nm-thick Pt counter electrode (CE) and two ceria working electrode (WE) pads with 300-nm-thick Au current collectors. The alumina films underneath the Au current collectors function to block O²⁻ ionic transport between YSZ and Au.⁸¹ By blocking the O²⁻ transport into the Au pad, the electrochemical side reactions on the Au current collector are precluded. Approximately 1000-nm-thick dense ceria films are patterned on top of the Au such that elongated Au pads on one end are left exposed for electric connections (**Figure 4-1**). The 600- μm regions of the ceria film has direct contact with the supporting YSZ electrolyte, allowing O²⁻ ions move across the CeO_{2-x}-YSZ interface. This cell geometry with the ceria WE and Pt CE deposited on the same side of the YSZ electrolyte support allows full access to all cell component surfaces for XPS studies.

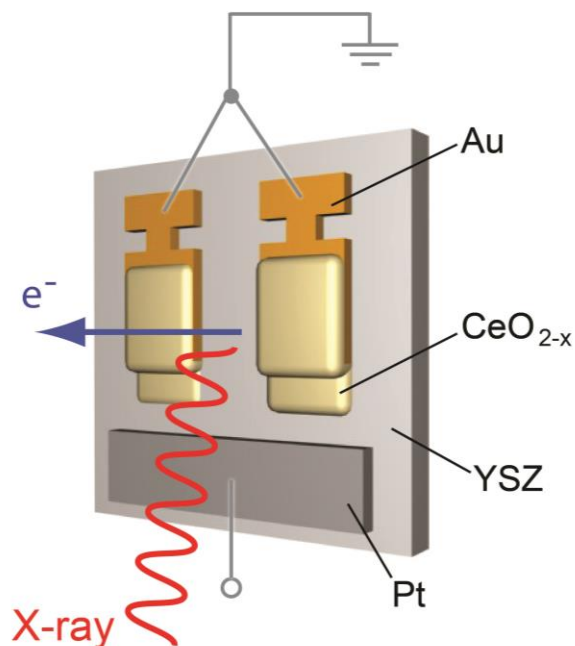
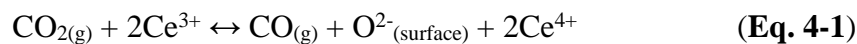


Figure 4-1. Schematic illustration of the electrochemical cell comprising a 300 nm Pt CE, a 300 nm Au current collector on top of a 30 nm Al₂O₃ film (not shown) and 1000 nm CeO_{2-x} WE patterned onto a polycrystalline YSZ substrate.

Since both the ceria WE and the Pt CE are exposed to the same gas environment of 0.5 Torr of 1:20 CO/CO₂ ~600 °C, there is no thermodynamic driving force when the gas phase reactants reach equilibrium with the electrode surfaces. This situation results in a near-zero open-circuit voltage (OCV) that reflects the differences in electrochemical potentials of the two electrodes. At OCV, the CeO_{2-x} surface reaches thermal equilibrium with the CO and CO₂ gases as described by the following process:



The presence of Ce³⁺ and Ce⁴⁺ species in this equilibrium is due to the fact that electrons are conducted through ceria along the Ce sites as described by the polaron

hopping mechanism (Chapter 1, Section 1.2.5). Therefore, the Ce^{3+} species actually represent electrons and **Eq. 4-1** can be written as: $\text{CO}_{2(\text{g})} + 2\text{e}^- \leftrightarrow \text{CO}_{(\text{g})} + \text{O}^{2-}_{(\text{surface})}$.

Under positive or negative bias conditions, the mixed-ionic-electronic-conducting (MIEC) behavior of ceria (see Chapter 1, Section 1.2.5) allows electric current pass across the SOC by exchanging electrons with the Au current collector and O^{2-} with the YSZ electrolyte support. Specifically, at positive bias ceria functions as a cathode and promotes CO_2 electrolysis reactions, while Pt acts as an anode and promotes CO electro-oxidation. At negative bias, the roles of the electrodes are reversed such that CO_2 electrolysis occurs on Pt and CO electro-oxidation occurs on ceria. **Figure 4-2** shows a schematic illustration of the electrochemical reactions occurring on the specially designed single-sided ceria-based SOC under positive and negative biases.

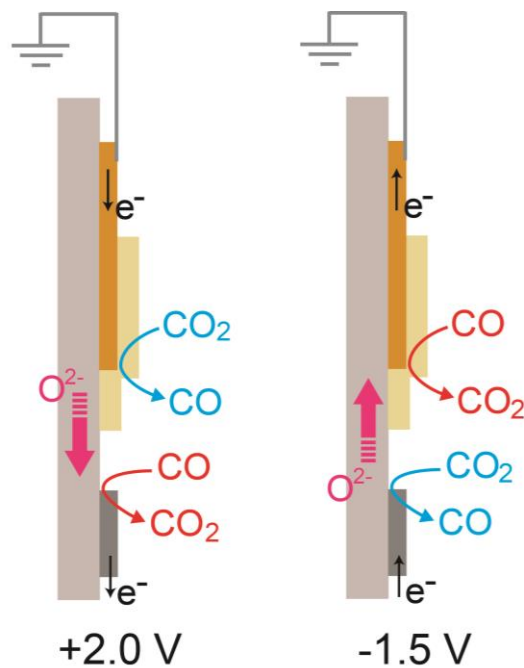


Figure 4-2. Schematic illustration of electrochemical reactions on the specially designed single-sided SOC under positive and negative biases.

A positive potential applied on the Pt electrode drives electrons from the Au current collector to ceria, and moves O^{2-} from the ceria surface down to the YSZ and out to the Pt electrode (**Figure 4-2**). Under such conditions, **Eq. 4-1** is driven away from the equilibrium value, and is favored in the forward direction. Therefore, the positive bias promotes CO_2 electro-reduction reactions on the ceria electrode surface and CO electro-oxidation reactions are promoted at the Pt-YSZ three phase boundary (TPB) (**Figure 4-2**). When the bias is reversed (negative bias on Pt), the surface reactions occur in the opposite direction to give CO electro-oxidation on ceria and CO_2 electrolysis at the Pt-YSZ edge.

4.3.1 C 1s and O 1s XPS

Figure 4-3 presents typical spatially-resolved XPS spectral images of the C 1s region obtained from the 2D detector system at OCV, -1.5 V, and +2.0 V applied biases. XPS photoelectron binding energy (BE) values (abscissa) are plotted against the cell position (ordinate) with the photoelectron intensities denoted by the color intensities. The schematic cell drawing on the left of the figure shows the corresponding cell position given in the ordinate, where 0.0 mm represents the edge of the Au current collector.

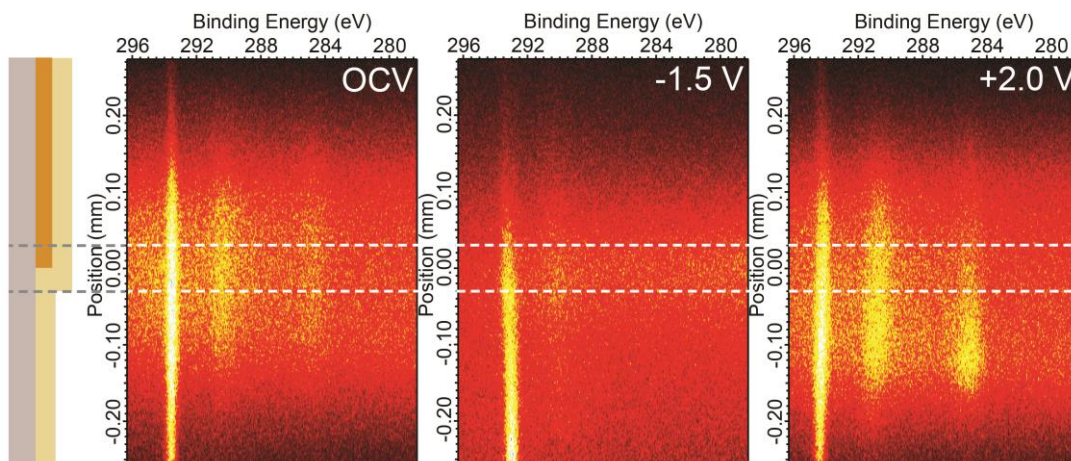


Figure 4-3. Spatially-resolved XPS measurements of the C 1s obtained with a 2D area detector at 0, -1.5 and +2.0 V applied potentials (~ 600 °C with 0.5 Torr of 1:20 CO/CO₂ mixtures). A corresponding schematic cell drawing is given on the left. Color scheme is denoted in **Figure 4-1**. The CeO_{2-x} is 1000 nm thick on the WE.

XPS spectra at different positions are obtained by slicing the XPS intensity maps into 20 or 60- μm segments as described in the experimental section (Section 4.2.3).⁵⁶ Because of the limited electronic and ionic conductivity of CeO_{2-x}, the electrochemically active region of the ceria electrode is limited to the ~ 200 μm region on either side of the Au edge.^{30,56,80} **Figure 4-4** shows representative spectra along the Au edge, which is the most electrochemically active region of the SOC. After subtraction of a Shirley background, the peaks are fitted using a nonlinear, least squares routine with mixed Gauss-Lorentz function of 70% Gaussian and 30% Lorentzian. An asymmetric line shape is introduced to fit the graphitic carbon peak in the C 1s region. To accurately reflect the relative intensities of the respective features, the background subtracted and integrated spectrum are normalized to the intensity of the gas phase CO₂ peak at ~ 293 eV.

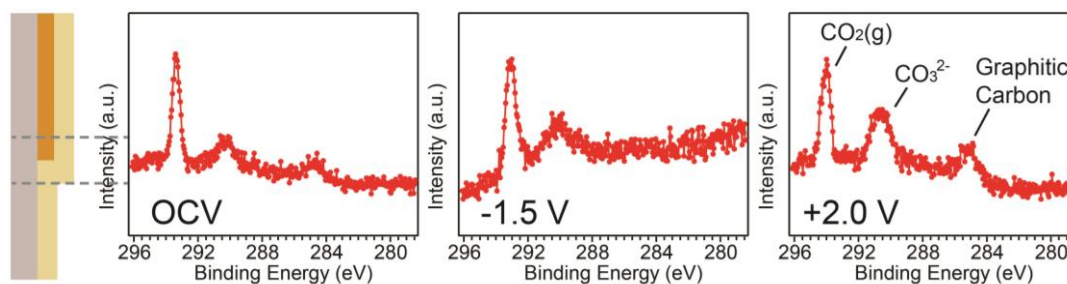


Figure 4-4. Integrated XPS spectra obtained by slicing a 60- μm -wide segment from the corresponding photoelectron signal in **Figure 4-3** at position of 0.0 mm. Intensities are normalized to the CO_2 gas phase peak ($\sim 600^\circ\text{C}$ with 0.5 Torr of 1:20 CO/CO_2 mixtures).

As shown in **Figure 4-4**, three features present at OCV in the C 1s spectra: 293.5, 290.3 and 284.8 eV. The peak at 293.5 eV is the CO_2 gas phase peak in the ambient environment,^{29,44,137} showing chemical shifts of 3 - 9 eV that result from surface contributions to higher BEs due to the final state effects⁴⁰. The peak at 284.8 eV is a graphitic/adventitious carbon species²⁹ on the surface. The third peak at 290.3 eV separates from the graphitic carbon feature by ~ 5.5 eV and is attributed to CO_3^{2-} species. The position of this peak is consistent with those reported for CO_3^{2-} on ceria surfaces^{28,29,134,138}.

No evidence of carboxylate ($\text{Ce-CO}_2^{\delta-}$) (BE = 285.8 - 288.5 eV^{29,134,139}) is found in the C 1s spectra. The presence of oxalate ($\text{C}_2\text{O}_4^{2-}$) (BE = 287 - 289 eV¹⁴⁰⁻¹⁴²) is also unlikely due to its low stability at high temperatures and the lack of C_2 products in high temperature CO_2 electrolysis reactions^{65,120,123,124}.

Upon applying a bias of -1.5 V, the graphitic carbon feature near 285 eV largely disappears around the edge of the Au current collector (**Figure 4-3** and **Figure 4-4**) as a result of electro-oxidation on the CeO_{2-x} electrode. At a bias of +2.0

V, the intensities of 290 and 285 eV peak increase, indicating the increases in steady-state concentration of CO_3^{2-} and graphitic carbon.

In the O 1s spectra shown in **Figure 4-5**, three oxygen-containing species are present at OCV: gas phase CO_2 at 539.6 eV,^{40,44,137} the CO_3^{2-} oxygen at 534.5 eV^{28,29,138} and the O^{2-} feature at 532.4 eV^{102,138,143,144}. The peak at 534.5 eV could be attributed to CO_3^{2-} , HCOO^- , $\text{Ce-CO}_2^{\delta-}$ and OH on CeO_{2-x} .²⁹ However, since the cell is exposed to gas mixtures of CO and CO_2 without hydrogen in the system, the presence of hydrogen-containing species, *i.e.*, HCOO and OH, are largely excluded. $\text{Ce-CO}_2^{\delta-}$ is ruled out by examining the C 1s spectra (**Figure 4-3** and **Figure 4-4**) as explained above.

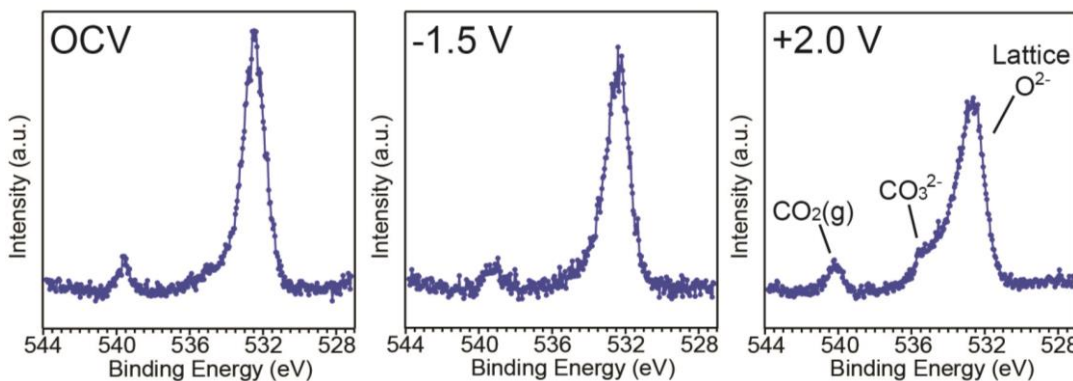


Figure 4-5. Integrated XPS spectra of the O 1s obtained at 0, -1.5 and +2.0 V applied biases at the cell position of 0.0 mm. The CeO_{2-x} is 1000 nm thick on the WE. Intensities are normalized to the CO_2 gas phase peak. Data are collected at $\sim 600^\circ\text{C}$ with 0.5 Torr of 1:20 CO/ CO_2 mixtures.

4.3.2 Reversible Change in Carbonate Coverage

To obtain a quantitative analysis of the relative surface carbonate coverage as a function of applied bias, the intensities of the CO_3^{2-} peak at 290 eV (C 1s) and 534 eV (O 1s) are integrated and then normalized to the integrated gas peak intensities

from the same spectrum. **Figures 4-6** and **Figure 4-7** plot the relative coverage of CO_3^{2-} adsorbates extracted from C 1s and O 1s data, respectively.

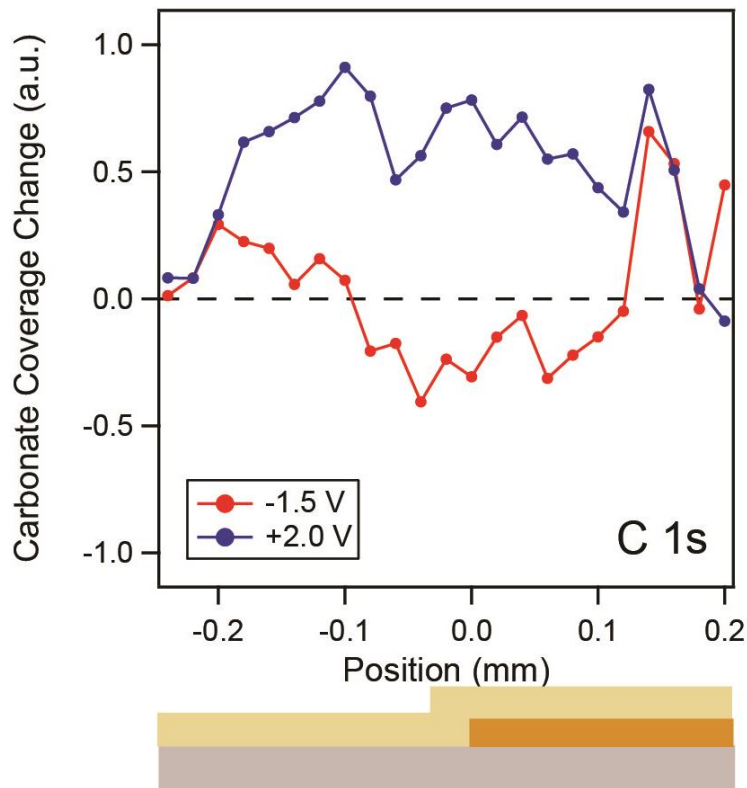


Figure 4-6. Coverage changes of CO_3^{2-} adsorbates away from OCV conditions derived from C 1s XPS spectra under -1.5 and +2.0 V applied bias ($\sim 600^\circ\text{C}$ with 0.5 Torr of 1:20 CO/CO_2 mixtures). The coverage is calculated from the integrated intensities of the adsorbate peak as shown in **Figure 4-3** and **Figure 4-4**, and these values are normalized to the integrated signals of the gas phase CO_2 peak from the same spectrum. Data extracted from edges of the detector window are less reliable and have been removed. Corresponding schematic cell drawing is given at the bottom. Color scheme is given in **Figure 4-1**.

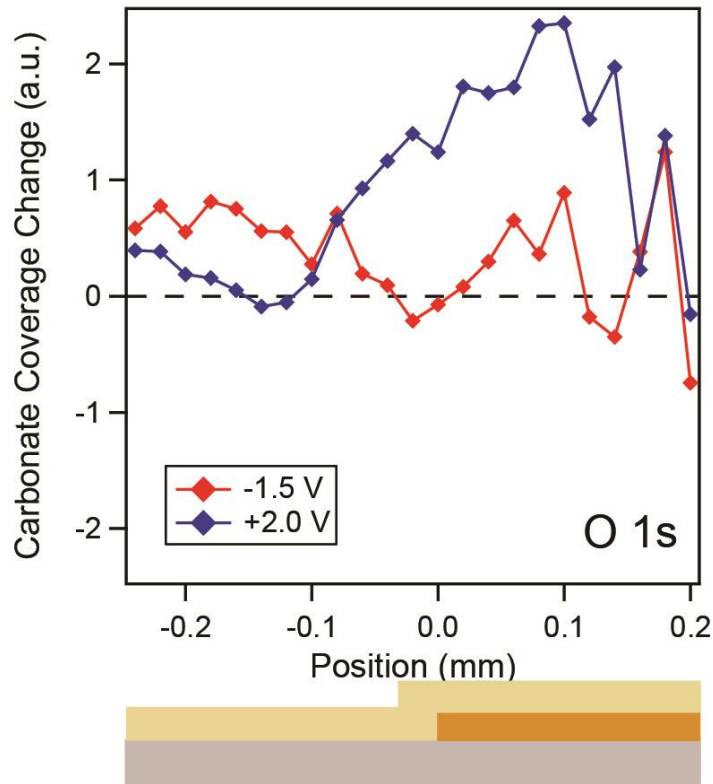


Figure 4-7. Coverage changes of CO_3^{2-} adsorbates away from OCV conditions derived from O 1s XPS spectra under -1.5 and +2.0 V applied bias ($\sim 600^\circ\text{C}$ with 0.5 Torr of 1:20 CO/ CO_2 mixtures). The coverage is calculated from the integrated intensities of the adsorbate peak as shown in **Figure 4-3** and **Figure 4-4**, and these values are normalized to the integrated signals of the gas phase CO_2 peak from the same spectrum. Data extracted from edges of the detector window are less reliable and have been removed. Corresponding schematic cell drawing is given at the bottom. Color scheme is given in **Figure 4-1**.

The presence of carbonate species on the cell surface at OCV results from the adsorption of CO_2 onto the oxide surface.^{138,145} As shown in **Figure 4-6** and **Figure 4-7**, when CO_2 electro-reduction is promoted at +2.0 V, the steady-state concentrations of CO_3^{2-} increases within the 400- μm region around the Au edge. A small but measurable decrease in CO_3^{2-} concentration is observed when CO electro-oxidation occurred on the ceria surface (-1.5 V). This increase/decrease in intensity of the CO_3^{2-} peak is reproduced when the cell is cycled among electro-reduction, OCV

and electro-oxidation conditions, which strongly suggests that CO_3^{2-} is involved in the electrochemical **Eq. 4-1** as a reaction intermediate.

The mapping of CO_3^{2-} coverage from O 1s (**Figure 4-7**) is hampered by the presence and gradual segregation of silicon oxide (SiO_2) impurity onto the electrode surface at elevated temperatures. Previous XPS results show that the O 1s XPS peak of Si-O has a BE ~ 2.0 eV higher than the lattice O^{2-} peak of ceria,⁸⁰ which is coincident with the CO_3^{2-} signal at 534.5 eV. In **Figure 4-6**, the CO_3^{2-} coverages extracted from C 1s show a decrease at -1.5 V and an increase at +2.0 V relative to the OCV equilibrium. However, the surface concentration of SiO_2 increases with the passage of time, regardless of the applied biases (**Figure 4-8**). Therefore, at -1.5 V, the decrease of CO_3^{2-} and the increase of SiO_2 counteract each other and the signal at 534.5 eV appears largely unchanged (**Figure 4-7**).

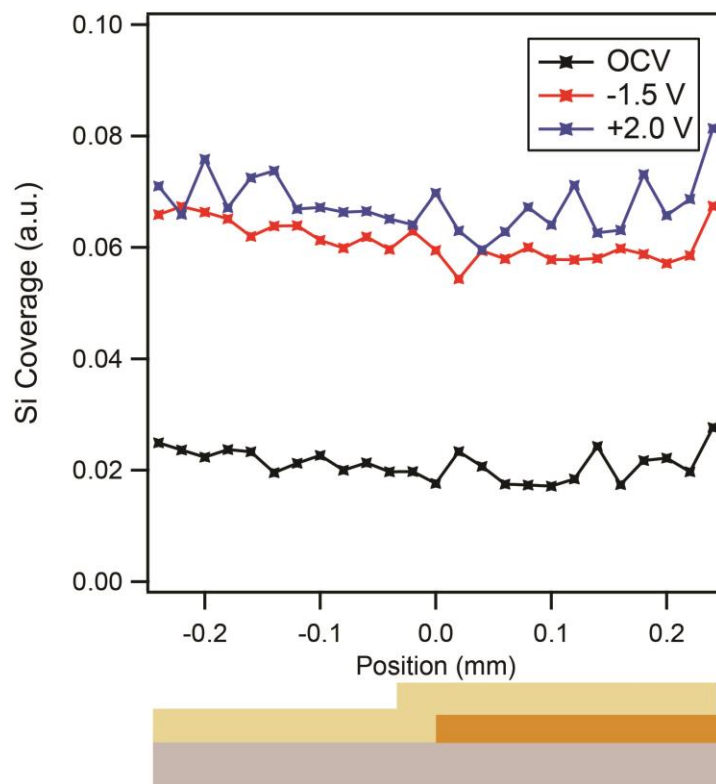
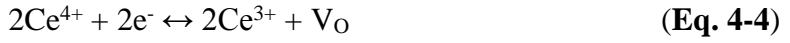
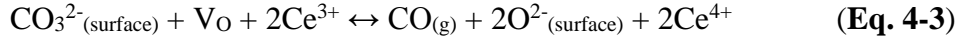
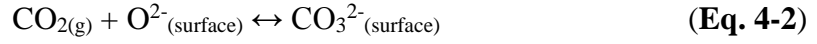


Figure 4-8. Coverage of SiO₂ on the CeO_{2-x} electrode surface under OCV, -1.5 V and +2.0 V (~600 °C with 0.5 Torr of 1:20 CO/CO₂ mixtures). The coverages are determined from the integrated intensities of the Si 2p peak. The values are normalized to the integrated signals of the Ce 4d peaks collected from the same spectrum. Corresponding schematic cell drawing is given at the bottom. Color scheme is denoted in **Figure 4-1**.

4.3.3 Rate-Limiting Process

Previous chapters (Chapter 2 and Chapter 3) and publications have demonstrated *operando* AP-XPS as a successful diagnostic technique in detecting reaction intermediates and providing mechanistic information in electrochemical studies of H₂/H₂O on SOCs.^{30,56,80} In this investigation of CO/CO₂ system, the detection of CO₃²⁻ over the ceria electrode and its observed reversible changes in steady-state concentration during CO₂ electrolysis and CO electro-oxidation reactions

indicates that CO_3^{2-} is an intermediate in both electro-chemical reactions. Therefore, the overall reaction **Eq. 4-1** can be described by three sequential, general equilibria:



Eq. 4-2 represents the thermal equilibrium of CO_3^{2-} formation from $\text{CO}_{2(\text{g})}$ with the lattice O^{2-} on the ceria surface; **Eq. 4-3** describes the general redox process involving charge transfer between the CO_3^{2-} species and the $\text{Ce}^{3+/4+}$ ions where V_O represents the oxygen vacancy; **Eq. 4-4** is the reversible polaron hopping process (Chapter 1, Section 1.2.5) that occurs in partially reduced CeO_{2-x} . The formation of Ce^{3+} on the surface is accompanied by formation of a surface oxide vacancy, V_O .

The observed increase in both CO_3^{2-} (**Figure 4-6** and **Figure 4-7**) and Ce^{3+} (**Figure 4-9**) concentrations at the +2.0 V bias within a 400- μm region (-0.2 to 0.2 mm) suggests that the overall process of **Eq. 4-3** is rate-limiting in the CO_2 electrolysis direction on ceria.

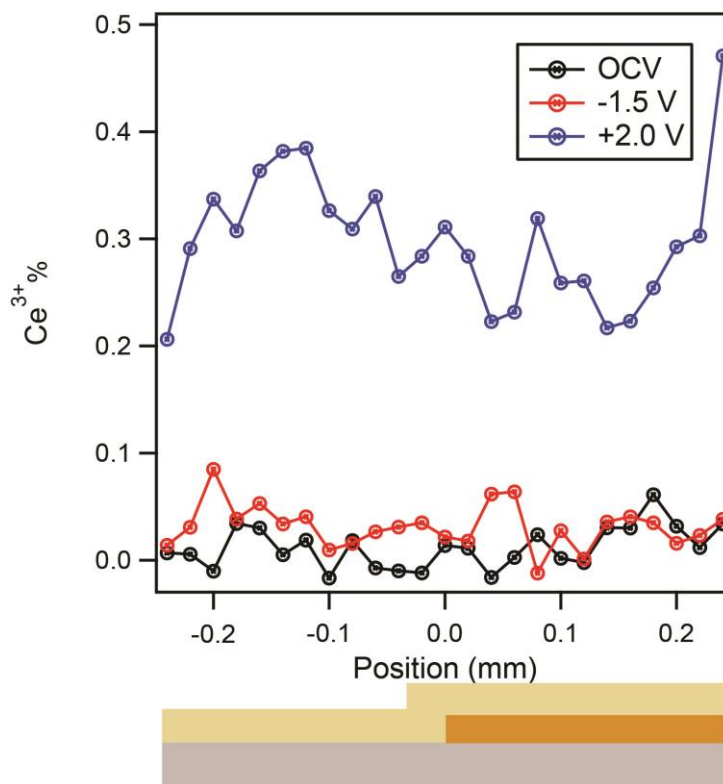


Figure 4-9. The relative concentrations of Ce^{3+} measured *operando* at OCV, -1.5 and +2.0 V ($\sim 600\text{ }^\circ\text{C}$ with 0.5 Torr of 1:20 CO/ CO_2 mixtures). The concentrations are determined from the ratio of the high BE Ce^{4+} to the total fitted Ce area.⁵⁶

At OCV equilibrium, the reaction intermediates of $\text{CO}_3^{2-}_{(\text{surface})}$, Ce^{4+} and Ce^{3+} are present and observable in the XPS measurement (**Figure 4-3**, **Figure 4-4**, and **Figure 4-9**). When the cell is biased, the reactions are driven out of equilibrium to achieve steady state concentrations commensurate with the applied potential. However, the shifts of the three reaction processes from equilibrium are not equivalent, which provides insight on the rate limiting process. It is important to note that each of these processes may involve several individual mechanistic steps and each equilibria described as **Eq. 4-2**, **Eq. 4-3** and **Eq. 4-4** represents a general process.

Specifically, when the positive bias is applied to promote CO₂ electrolysis on ceria, all three processes of **Eq. 4-2**, **Eq. 4-3** and **Eq. 4-4** are shifted towards the forward direction and away from their equilibrium positions. Before the steady state is reached, the three processes are occurring at different rates, *i.e.*, the generation of CO₃²⁻ and Ce³⁺ through **Eq. 4-2** and **Eq. 4-4** proceed faster than the consumption of CO₃²⁻ and Ce³⁺ through the rate-limiting process (**Eq. 4-3**). Therefore, this difference in reaction rates leads to an increase coverage of CO₃²⁻ and Ce³⁺ on the ceria surface. Once the steady state is achieved, the three processes again share the same rates, which stops the growth of CO₃²⁻ and Ce³⁺ and maintains their steady state concentrations. The sluggishness of **Eq. 4-3** indicates that the electrolysis reaction is rate limited by the electron transfer process from Ce³⁺ to CO₃²⁻.

When the potential bias is switched to -1.5 V, CO₃²⁻ coverage slightly decreases from OCV in a 200- μ m region (-0.1 to 0.1 mm). This small but observable change in CO₃²⁻ concentration suggests that **Eq. 4-3** is also rate-limiting in the reverse direction under negative bias. As a result, these data show that the reaction process described in **Eq. 4-3** is slower than the reactions processes of **Eq. 4-2** and **Eq. 4-4** in both ceria-catalyzed CO₂ electrolysis and CO electro-oxidation.

4.3.4 Reaction Mechanism of CO₂ Activation

Although the universal mechanism of CO₂ activation on ceria is not yet clear, earlier thermal studies suggest that defects sites, such as Ce³⁺ and V_(O), are active sites for CO₂ activation via formation of either CO₃²⁻ or carboxylate (Ce-CO₂).^{131,146} Staudt *et al.* investigated the reactivity of ceria surfaces toward CO₂ by introducing basic sites of MgO.¹³⁴ They observed that the formation of Ce-CO₂ ^{δ^-} and the re-oxidation of

ceria by CO₂ were suppressed when the addition of defect sites facilitated the formation of stable surface CO₃²⁻. They concluded that the surface Ce-CO₂^{δ-} was the true intermediate of the CO₂ activation process. In contrast, Wu *et al.* found that for pure ceria surfaces, the CO₃²⁻ species are associated with Ce³⁺ sites were the main reaction intermediates in CO oxidation.¹³⁵ DFT investigations of CO₂ activation on ceria also suggested reaction pathways that involve CO₃²⁻ intermediates but the carboxylate reaction pathways were very close in terms of energy.¹³³ These combined experimental and theoretical studies of CO and CO₂ activation on ceria suggest that reaction pathways involving CO₃²⁻ and Ce-CO₂^{δ-} intermediates are close in energy and the lowest energy pathway may depend on specific reaction conditions.

In this study, Ce-CO₂^{δ-} is not detected when the ceria electrode is exposed to CO/CO₂ gas mixture or biased at different potentials (Section 4.3.1). Only the CO₃²⁻ surface species show clear changes in steady-state concentration when the applied biases are switched to promote electrochemical reactions in different directions. While not directly comparable due to the markedly different reaction conditions, the studies described in this chapter are consistent with *in situ* vibrational studies of Wu *et al.*¹³⁵ although the different modes of carbonate binding, *i.e.*, unidentate or bridged carbonate, is not resolved by XPS. To determine what type of carbonate plays the major role in the reaction mechanism in high temperature electrochemical processes, other analytical techniques and further experiments are required.

4.3.5 Overpotentials at the Pt-YSZ Interface

As shown in **Figure 4-10**, the observed cell currents at negative applied bias are an order of magnitude smaller than those observed at positive applied bias. The

origins of the differences in currents are most likely due to the unfavorable CO₂ reduction overpotentials (η) at the Pt electrode and the increased electrical resistance at the ceria electrode at negative bias. Previous studies showed that approximately 70% of the potential loss at -1.5 V is associated with the CO₂ electrolysis occurred at the Pt-YSZ TPB (see **Figure 4-2**)¹³⁶. This large charge transfer overpotential and the increased electrical resistance of the ceria electrode give rise to a small current of +22 μ A at -1.5 V, which is in sharp contrast to the -240 μ A steady state current observed at +1.5 V (see **Figure 4-10**). The smaller change in surface CO₃²⁻ concentration at negative bias relative to positive bias is most likely a result of this reduced electric current. Note that the currents between -1.5 V and -2.0 V do not significantly change (**Figure 4-11**) and therefore data collected at -1.5 V that has better signal resolution is shown.

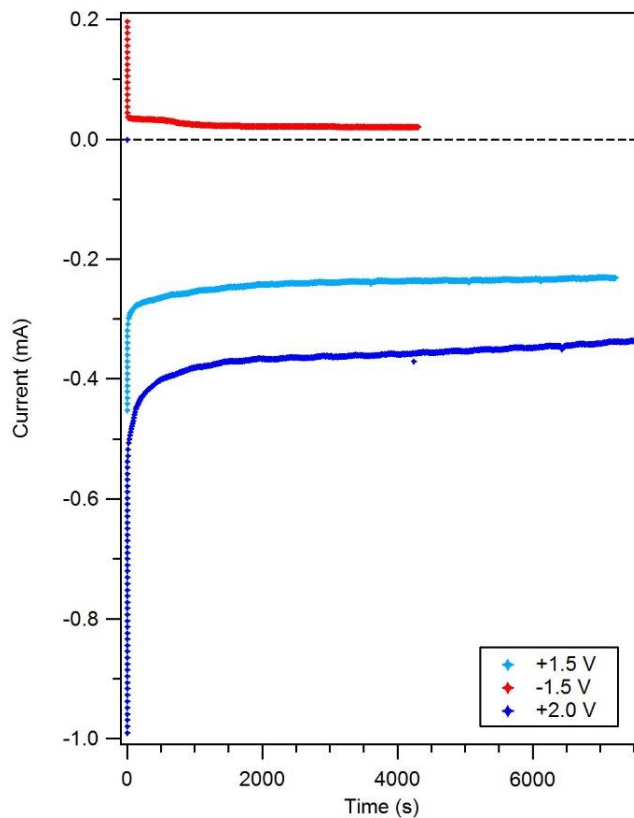


Figure 4-10. Plot of cell current as a function of time under different applied biases (+1.5 V, -1.5 V, and +2.0 V). Measurement are collected on an SOC with 1000-nm-thick ceria film at ~600 °C with 0.5 Torr of 1:20 CO/CO₂ mixture.

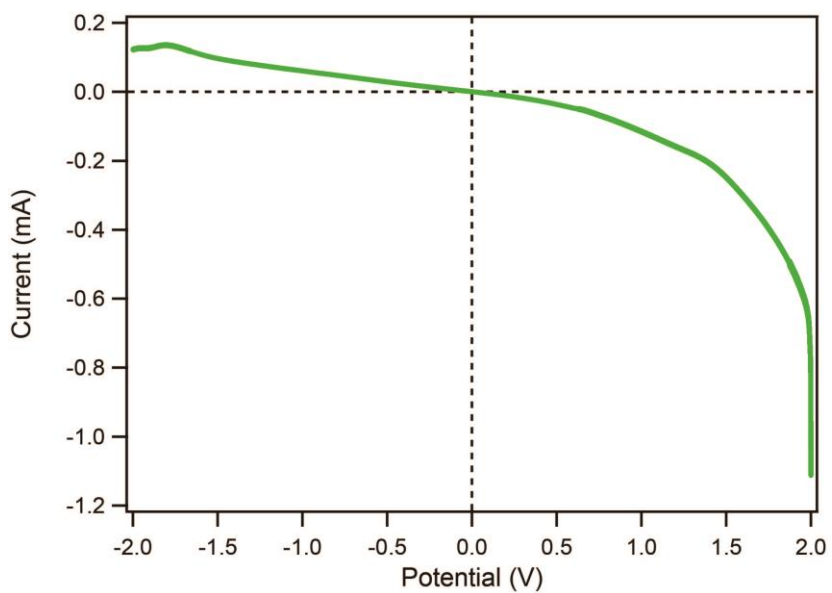


Figure 4-11. LSV polarization curves of SOC with 1000-nm-thick CeO_{2-x} film at ~600 °C with 0.5 Torr of 1:20 CO/CO₂ mixture.

The large overpotential η at the Pt-YSZ interface is consistent with the findings of Sridhar *et al.*¹¹⁹ Subsequent studies of CO₂ electrolysis on Ni/YSZ and GDC-based materials showed significantly lower η values and better performance.^{121,123,124} The poor performance on the Pt electrode could be due to its inability to form CO₃²⁻ intermediates on the Pt surface (no CO₃²⁻ formation is observed at the Pt electrode in this case). As a result, a direct initial electron transfer step to the CO₂ molecule is required (CO₂ + e⁻ → CO₂⁻). In solution studies, it is well known that this initial electron transfer step poses the largest energy barrier (highest η) to solution based electro-reduction of CO₂.¹¹⁵ The ability of CeO_{2-x} to accommodate CO₃²⁻ intermediates can be the mechanistic origin of lower overall η and superior performance.

4.3.6 Electrochemically Active Region in CO/CO₂ System

In **Figure 4-6**, the 200 μm wide region of CO₃²⁻ depletion at negative bias demarcates the electrochemically active region. This active region is significantly smaller than the 400 μm wide active region observed at positive bias. The smaller active region at negative bias presumably results from the lower ratio of Ce³⁺/Ce⁴⁺ (**Figure 4-9**) and the consequent reduced electronic conductivity under these oxidizing conditions, which is consistent with previous studies^{30,80}.

In addition, the growth of conducting graphitic carbon species under +2.0 V applied bias also enhances electronic conductivity⁶² in the ceria electrode, and, therefore, extends the electrochemically active region further away from the Au edge.¹³⁶

4.4 Summary

Electro-reduction of CO₂ and electro-oxidation of CO over ceria-based SOCs is investigated through the use of *operando* AP-XPS in the presence of 0.5 Torr of CO/CO₂ gas mixtures at ~600 °C. During CO₂ electrolysis reactions on ceria at positive applied biases, the steady-state concentration of CO₃²⁻ increases over a 400-μm-wide active region on the CeO_{2-x} electrode surface. In contrast, the CO₃²⁻ concentration slightly decreases during CO electro-oxidation. The build-up of CO₃²⁻ at positive biases suggests that 1) the CO₂ electrolysis reaction goes through a CO₃²⁻ intermediate, and requires the pre-coordination of CO₂ to the ceria surface to form a CO₃²⁻ intermediate (CO_{2(g)} + O²⁻_(surface) → CO₃²⁻_(surface)); 2) this reaction step precedes a rate limiting electron transfer process to give CO and oxide ions (CO₃²⁻_(surface) + 2Ce³⁺ → CO_(g) + 2O²⁻_(surface) + 2Ce⁴⁺). Similarly, the electron transfer process is shown rate-limiting in the reverse direction, resulting in the depletion of CO₃²⁻ during CO electro-oxidation under negative applied bias. However, the magnitude of CO₃²⁻ depletion occurs with a much smaller magnitude, most likely due to the unfavorable CO₂ electrolysis (high overpotential) at the Pt CE and the significantly reduced cell current generated under -1.5 V applied bias.

Chapter 5

Carbon Deposits and Pt-YSZ Overpotentials on Ceria-Based Solid Oxide Electrochemical Cell

5.1 Introduction

5.1.1 Carbon Dioxide Reduction on Ceria Catalyst

Fossil fuels such as coal, natural gas, and oil have been used for producing energy and commodity chemicals for the past two centuries. However, due to environmental concerns of global warming and economic incentives, interests are driven towards developing processes to convert carbon dioxide into fuels and chemicals in recent years.¹⁴⁷ The biggest challenge for CO₂ conversion is that CO₂ is a very stable molecule,^{114,145} requiring significant energy input and expensive catalysts to reduce it to carbon monoxide. Among various CO₂ conversion approaches being investigated, including thermolysis under extremely high temperatures and homogeneous catalysis by metal electrodes or molecularly modified electrodes, solar-driven reduction of CO₂ in combination with photocatalytic water splitting is suggested as an attracting approach to reduce CO₂ to CO.^{65,114} By using cerium oxide as catalyst materials, the fuel productivity (which determines the amount of catalyst required), the fuel production rate, and the thermodynamic efficiency has been reported to be further enhanced.^{128,148}

Ceria is a well-known catalyst for reactions of three-way conversion, water-gas shift reactions, steam reforming of methane as well as CO/CO₂ conversion (see Chapter 1, Section 1.2.5). Since Ce can reversibly convert between Ce⁴⁺ and Ce³⁺ upon release and storage of oxygen, ceria is commonly used for oxidation and reduction reactions. Ceria is also remarkable in that at high temperatures it can accommodate exceptionally high oxygen vacancy concentrations without significant change in crystallographic structure.³¹ Solar-driven thermochemical splitting of H₂O and CO₂ on reduced ceria catalysts has been investigated for fuel production applications.¹⁴⁸ Electrochemical conversions of CO and H₂ mixtures are also of interest for use as fuels in solid oxide fuel cells (SOFCs) that incorporate ceria electrocatalysts.

Since CO and H₂ are major components of syn-gas and reformed biogas feeds, it is important to understand the surface electrochemistry and the origins of cell losses in both electro-oxidation and electro-reduction processes. However, mechanistic understanding in these electrochemical reactions is still limited due to the lack of *in situ* or *operando* probing techniques and the complexity of the electrochemical processes involving many elementary steps.

5.1.2 Scope of the Chapter

The previous chapters (Chapter 2 and Chapter 3) have demonstrated that oxygen based charge transfer steps are rate-limiting with H₂/H₂O mixtures on Pt/yttria-stabilized zirconia (YSZ)/CeO_{2-x} solid oxide electrochemical cells (SOCs) and that surface potential losses and overpotential losses are fairly evenly distributed across the SOC (between the Pt and the CeO_{2-x} electrodes). In this chapter *operando*

ambient pressure X-ray photoelectron spectroscopy (AP-XPS) is utilized to investigate the single-sided Pt/YSZ/CeO_{2-x} electrochemical cell with CO/CO₂ gas reactants (the same experimental setup as that in Chapter 4). Unlike the H₂/H₂O system, the observed growth of graphitic carbon with the CO/CO₂ mixture in this study is shown to facilitate electron conduction within the ceria electrode, which extends the electrochemically active region away from the Au electron source. In addition, the cell losses with the CO/CO₂ mixture are dominated by the charge transfer overpotentials at the Pt-YSZ electrode-electrolyte interface, which contrasts the results from previous H₂/H₂O studies described in Chapter 2. The work described here involves close collaboration with Professor Zhi Liu and his research team at ALS.

5.2 Experimental

5.2.1 Solid Oxide Electrochemical Cell Preparation

Details regarding the cell fabrication can be found in Chapter 2 and Chapter 4. A brief overview is given here. The YSZ powder (8 mol%) was pressed, cut into square supports, heated to 1450 °C (1 °C/min), and sintered for 3 h. Aluminum oxide (Al₂O₃), Au, and Pt electrodes were sputtered with patterned stainless steel shielding masks. The Al₂O₃, Au, and Pt films are 30, 300, and 300 nm in thickness, respectively. Ceria films were deposited under 5 mTorr of O₂/Ar gas mixture (10% O₂). Two thicknesses (350 and 1000 nm) of ceria films were prepared for this study.

All samples were pre-annealed at 800 °C for 3 h before electrochemical and XPS measurements.

5.2.2 Electrochemical Measurements

Details describing the electrochemical measurements can be found in Chapter 2 and Chapter 4. A brief overview is given here. Electrochemical characterization of two-probe linear sweep voltammetry (LSV) and electrochemical impedance spectroscopy (EIS) measurements were conducted by using a Bio-Logic potentiostat. The single-chamber cells were clamped onto a ceramic heater and loaded into the AP-XPS end-stations⁷⁷ at beamline 9.3.2 of the Advanced Light Source (ALS), Lawrence Berkeley National Laboratory (LBNL). The spring-loaded probes of the cell mounting platen served as both clamps and electrical contacts/current collectors for electrodes (**Figure 2-2**).⁷⁸ Gas mixtures of 1:20 CO/CO₂ were leaked into the XPS chamber with a total pressure of 0.5 Torr. The cell was then heated to approximately 600 °C.

In each experiment the Au current collector of the working electrode (WE) was always grounded to the XPS chamber ($V_{\text{Au}} = 0.0 \text{ V}$) and the Pt counter electrode (CE) was biased by the potentiostat.^{56,79} Hence, the overall cell bias V_{Cell} is defined as the potential difference between the Pt CE and the WE Au current collector: $V_{\text{Cell}} \equiv V_{\text{Pt}} - V_{\text{Au}}$, which simplifies to $V_{\text{Cell}} = V_{\text{Pt}}$ in this cell geometry.

5.2.3 *Operando* Ambient Pressure X-ray Photoelectron Spectroscopy

Measurement

Details describing the XPS measurements can be found in Chapter 2 and Chapter 4. A brief description is given here. *Operando* AP-XPS measurements were conducted simultaneously with the electrochemical characterizations at ~600 °C with 0.5 Torr of 1:20 CO/CO₂ gas mixtures. Two-dimensional (2D) AP-XPS spectral maps were obtained by using the differentially pumped electron analyzer^{77,78} installed at beamline 9.3.2 of the ALS at LBNL.⁷⁷

The sample was oriented such that the X-ray incident angle was 75 ° and the electron emission angle was 0 ° with respect to the sample normal. The photon energy used for C 1s, Ce 4d, Pt 4f and Zr 3d was 490 eV and for O 1s was 650 eV. The binding energy (BE) values of C 1s and Ce 4d were calibrated by referencing against the bulk Au 4f_{7/2} peak (BE = 84.0 eV⁴²) collected with 490 eV photon energy.

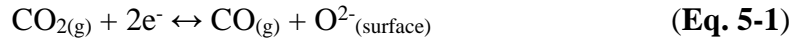
Analysis of the 2D XPS intensity maps was obtained by slicing the XPS intensity maps into 20 or 60-μm segments against the axis of position.^{30,56,80} CasaXPS software (Version 2.3.15) was used for data analysis. After subtracting a Shirley background, each slice was fitted using a nonlinear, least squares routine with mixed Gauss-Lorentz function of 70% Gaussian and 30% Lorentzian. An asymmetric line shape is introduced to precisely fit the graphitic carbon peak in the C 1s region.

5.3 Results & Discussion

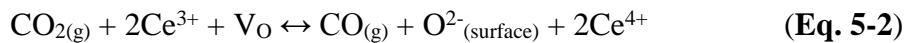
The specially designed single-sided polycrystalline YSZ cells contain one 300-nm-thick Pt counter electrode (CE) and two CeO_{2-x} working electrodes (WEs)

with 300-nm-thick Au current collectors. The alumina films underneath each of the Au films block ionic transport between YSZ and Au.⁸¹ By blocking the O²⁻ transport into the Au pad, electrochemical side reactions are precluded on the Au current collector. Dense thin ceria films (350 and 1000-nm-thick) are patterned on top of the Au with elongated Au pads exposed for electrical connections (**Figure 4-1**). The approximately 600 μm region of the ceria film has direct contact with the supporting YSZ electrolyte, which defines the O²⁻ ions transport pathway at the CeO_{2-x}-YSZ interface. Approximately 600 μm of uncovered YSZ separates the ceria edge and the nearest Pt edge. This cell geometry with the ceria WE and Pt CE deposited on the same side of the YSZ electrolyte support allows full access to all cell component surfaces for XPS studies.

Since both the ceria WE and the Pt CE are exposed to the same gas environment of 0.5 Torr of 1:20 H₂/H₂O ~600 °C, no thermodynamic driving force exists when the electrochemical reactions on both electrodes reach equilibrium with the gas phase. This situation results in a near-zero open-circuit voltage (OCV). At OCV, the cell surfaces reach thermal equilibrium with the CO and CO₂ gases as described by the following reactions:



On the CeO_{2-x} electrode electrons are localized on the Ce sites and reduce Ce⁴⁺ to Ce³⁺ as described by the polaron hopping mechanism (see Chapter 1, Section 1.2.5). When Ce^{3+/4+} species and oxygen vacancy sites (V_O) are taken into consideration, the above equation can be written as:



Under positive or negative bias conditions, the mixed-ionic-electronic-conducting (MIEC) behavior of CeO_{2-x} (see Chapter 1, Section 1.2.5) allows electric current pass across the SOC by exchanging electrons with the Au current collector and O^{2-} with the YSZ electrolyte support. At positive bias ceria promotes CO_2 electrolysis reactions as a cathode, while Pt promotes CO electro-oxidation. At negative bias, the roles of the electrodes are reversed such that CO_2 electrolysis occurs on Pt and CO electro-oxidation occurs on ceria. **Figure 5-1** shows a schematic illustration of the electrochemical reactions occurring on the specially designed single-sided ceria-based SOC under positive and negative applied biases.

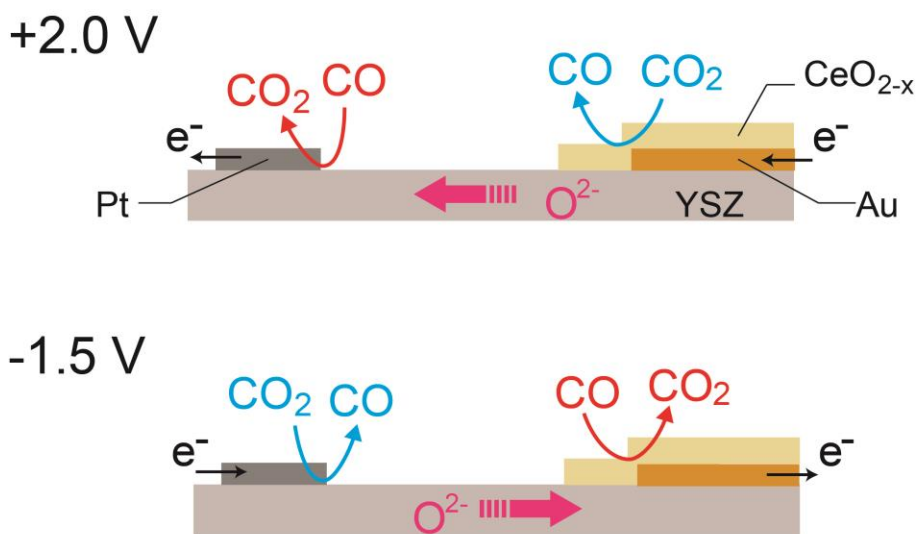


Figure 5-1. Schematic illustrations of electrochemical reactions under bias conditions on the single-sided SOC composed of a 300 nm Pt CE, a 300 nm Au current collector on top of a 30 nm Al_2O_3 film (not shown) and a 350 or 1000 nm CeO_{2-x} WE patterned onto the YSZ substrate. The drawing is not to scale.

More specifically, a positive applied potential (+2.0 V) on the Pt electrode drives electrons from the Au current collector to ceria, and moves O^{2-} from the ceria surface down to YSZ and out to the Pt electrode (**Figure 5-1**). Under such conditions,

Eq. 5-2 is driven away from equilibrium and is favored in the forward direction on ceria. Therefore, the positive bias promotes CO₂ electro-reduction reaction on the ceria electrode surface and CO electro-oxidation reaction occurs at the Pt-YSZ edge. At negative applied bias, electrochemical reactions are driven in the opposite direction, *i.e.*, CO electro-oxidation on CeO_{2-x} and CO₂ electrolysis at the Pt-YSZ interface (**Figure 5-1**, -1.5 V). Results of electrochemical measurements are given in Chapter 4, Section 4.3.5.

5.3.1 Graphitic Carbon Deposition on Ceria

In the integrated C 1s XPS spectra (Chapter 4, Section 4.3.1, **Figure 4-4**), a peak at 293.5 eV is identified as the CO₂ gas phase peak in front of the entrance aperture.^{29,40,44,137} Another peak at 284.8 eV is attributed to graphitic carbon species⁸⁶ on the surface. A chemical shift of 8.7 eV between the gas phase signal and the surface carbon signal results from final state effects⁴⁰. Upon -1.5 V bias, the graphitic carbon feature near 285 eV disappears around the Au edge, whereas under +2.0 V biases, this peak becomes better defined, indicating the concentration increase of graphitic carbon (**Figure 4-3** and **Figure 4-4**). To quantify the coverages of graphitic carbon formed on the ceria electrode under applied biases, intensities of the graphitic carbon peaks (~285 eV) are integrated. The integrated intensities are then normalized to the integrated signal of the gas phase CO₂ peak from the same spectrum.

As shown in **Figure 5-2**, the -1.5 V applied bias results in a small decrease in graphitic carbon coverage from the OCV condition, which is associated with the electro-oxidation of graphitic carbon species under the oxidizing bias. When CO₂ electrolysis is promoted on ceria at +2.0 V, the graphitic carbon coverage increases in

a 200- μm region in front of the Au current collector. A subsequent C 1s XPS spectrum is collected after the +2.0 V bias has been applied on the SOC for an hour. The graphitic carbon concentration in this subsequent C 1s spectrum (after biased for 1 h) shows significant increase relative to the OCV equilibrium, not only in the 200- μm region but also on the ceria electrode which covers the Au current collector (**Figure 5-2**). This observation suggests that the graphitic carbon is not maintaining a steady-state concentration on ceria under CO₂ electrolysis operation. In fact, it is continually formed and gradually accumulates over the ceria electrode surfaces.

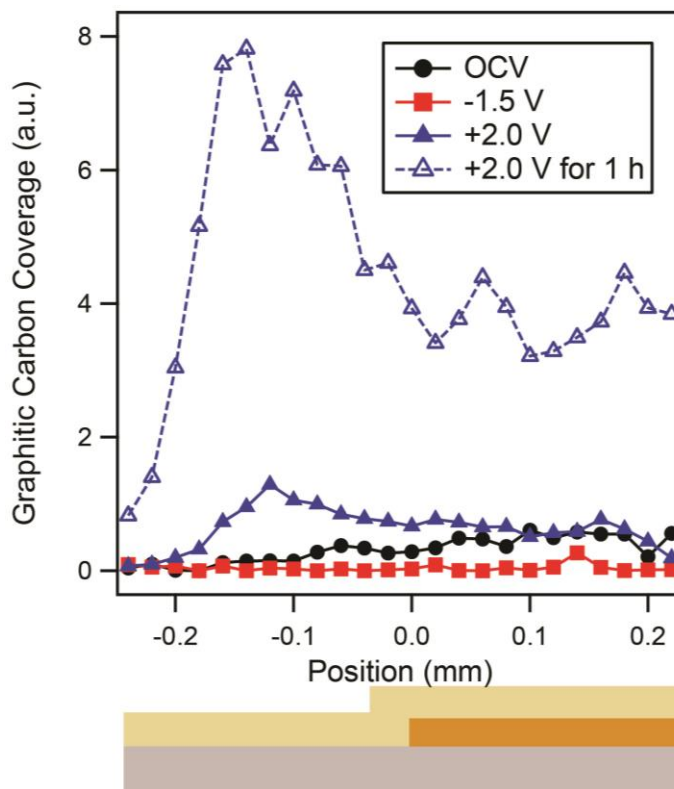


Figure 5-2. Coverages of graphitic carbon species extracted from C 1s under OCV, -1.5 and +2.0 V biases with 1:20 CO/CO₂ gas mixtures at ~600 °C. The coverages is obtained by integrating the intensities of the graphitic carbon peak and normalizing them to the integrated signals of the gas phase CO₂ peak. A subsequent spectrum is taken after the cell has been biased at +2.0 V for 1 hour. Data extracted from edges of the detector window are less reliable and hence removed.

5.3.2 Interpretations of Graphitic Carbon Deposition

Previous thermal studies of CO and CO₂ adsorption behaviors on oxidized and reduced ceria surfaces^{149–152} suggest the CO disproportionation reaction ($2\text{CO} \rightarrow \text{C} + \text{CO}_2$) is favored over reduced CeO_{2-x} at defect sites of Ce³⁺ and V_O and is responsible for the formation of free carbon species. To quantify the coverages of Ce³⁺ on the electrode surface in this study, Ce 4d XPS spectra are obtained and analyzed. **Figure 5-3** shows the relative Ce³⁺ coverages (*i.e.*, Ce³⁺/Ce⁴⁺ ratio) under different applied biases extracted from Ce 4d XPS spectra^{56,80}. It reveals that ~2% Ce³⁺ species present on the ceria surface at OCV. At -1.5 V bias the redox states largely maintain the OCV equilibrium values. However, when the cell bias is switched to +2.0 V to promote electro-reduction of CO₂ over ceria, the Ce³⁺ percentages increase to approximately 30%. More importantly, the Ce redox changes demarcate an electrochemically active region of 400 μm (**Figure 5-2**), which is the same as that revealed from the formation of graphitic carbon (**Figure 5-3**). These data suggest the presence of graphitic carbon is strongly related to the coverages of defect sites of Ce³⁺ and oxygen vacancies on ceria, which agrees well with previous thermal studies^{149–152}.

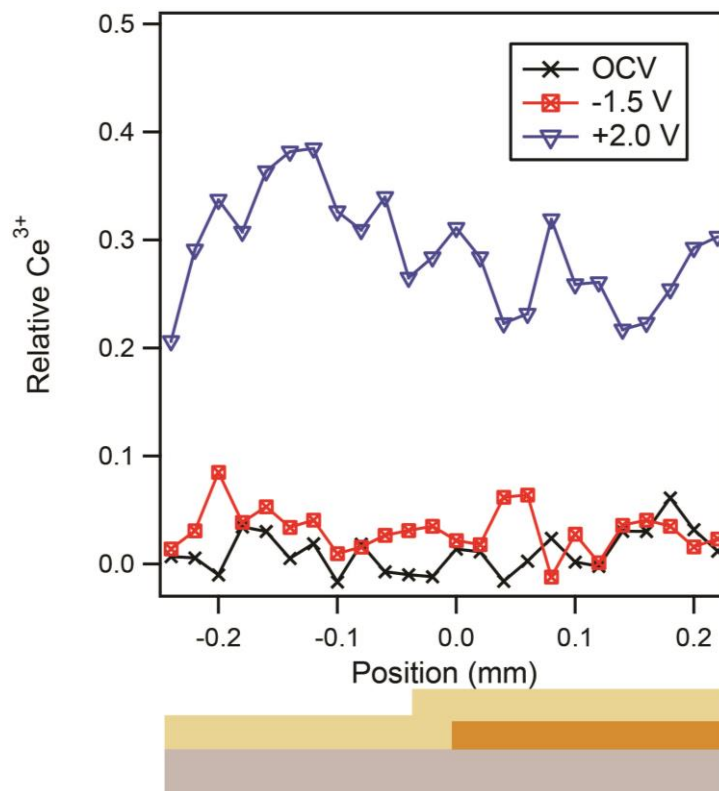


Figure 5-3. The relative concentrations of Ce^{3+} measured *operando* under potentials of OCV, -1.5 V and +2.0 V with 1:20 CO/CO₂ mixtures at ~600 °C. The concentrations are determined from the ratio of the high binding energy Ce^{4+} to the total fitted Ce area.^{56,80} Data measured from edges of the detector window are less reliable and hence removed.

An alternative cause for the formation of graphitic carbon is the electro-reduction of CO₂ or CO to carbon ($\text{CO}_2 + 4\text{e}^- \rightarrow \text{C} + 2\text{O}^{2-}$ or $\text{CO} + 2\text{e}^- \rightarrow \text{C} + \text{O}^{2-}$). By comparing ceria electrodes in different thicknesses (350 and 1000-nm-thick) it is determined that the contribution from these electro-reduction reactions to the formation of carbon is much smaller than the above-mentioned carbon disproportionation reaction. With identical cell geometry, an SOC with 350-nm-thick ceria electrode produces cell current of -340 μA at +2.0 V, similar to the current of -350 μA generated by the 1000-nm-thick ceria electrode at the same applied bias. However, the growth of graphitic carbon species on the 350 nm electrode is much

faster than that observed on the 1000 nm ceria cell. The significant increase in the speed of carbon growth and the same cell currents suggest that the production of graphitic carbon is not due to the electro-reduction of CO_2 or CO. In fact, the difference in how quickly the graphitic carbon formed over CeO_{2-x} is more likely associated with the different coverages of defect sites. On the 350-nm electrode, ~60% Ce^{3+} is present on the surface at +2.0 V, which is twice as much as surface Ce^{3+} concentration on the 1000-nm electrode. The results from this comparison again agree with the reported findings^{149–152} that the disproportionation reaction of CO is favored on reduced CeO_{2-x} surfaces.

5.3.3 Extension of Electrochemically Active Region

The presence of conductive graphitic carbon on the electrode surface results in improving the electron conduction capability of the ceria electrode. Chapter 2 and previous studies^{56,80} have shown how local surface potentials (V_L) under biased conditions can be directly measured across an electrochemical cell by monitoring the shifts in apparent BE values relative to those at OCV. With similar analysis approaches described in Chapter 2, the map of entire cell surface potentials is obtained from monitoring the trace element of Si on the cell surface and is plotted in **Figure 5-4**.

The local surface potentials from this study extracted from the Si 2p photoelectron peak at -1.5 and +2.0 V is given in **Figure 5-4**. In contrast to previous studies with $\text{H}_2/\text{H}_2\text{O}$ mixture that show sharp potential losses in the ~200 μm electrochemically active region centers at the edge of the Au current collectors

(**Figure 2-8** and **Figure 2-9**), the current studies reveal broad and continuous potential losses over the entire ceria tab.

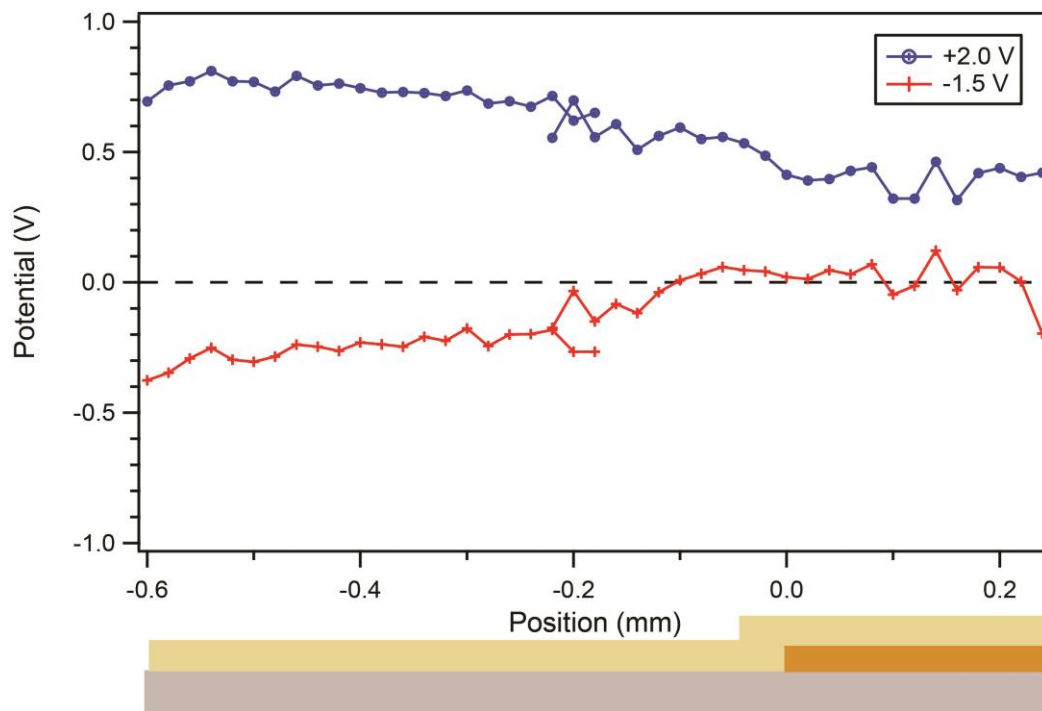


Figure 5-4. Plots of local surface potential calculated from the BE shifts in Si 2p photoelectrons relative to OCV conditions. The data are collected at -1.5 V and +2.0 V with 0.5 Torr of 1:20 CO/CO₂ mixtures at ~600 °C. Data extracted from edges of the detector window are less reliable and hence removed. Two windows of data overlap at the position of -0.2 mm.

Previous investigations into H₂/H₂O system at ~700 °C with the same SOC geometry reveal electrochemically active region 150 - 200 μm away from current collectors on ceria electrodes (**Figure 2-9**, **Figure 2-10** and **Figure 2-11**).^{56,80} In this study, the observed extension of the active region for CO/CO₂ system at an even lower operating temperature of 600 °C suggests that electrical transport property of CeO_{2-x} is enhanced by the presence of conducting graphitic carbon species formed on the surface. Once the graphitic carbon is produced from the CO disproportionation reaction (discussed in Section 5.3.2), it functions to facilitate the electron conduction

on the ceria electrode and allows the extension of active region further away from the Au electron source. Similar electrical enhancements have been documented in ceria based SOFCs by other research groups.⁶² McIntosh *et al.* found that exposure of a porous YSZ/CeO₂/Cu anode to n-butane at 700 °C resulted in the deposition of electronically conducting carbonaceous film. The carbonaceous deposits enhanced the cell performance by providing electronically conducting bridges between isolated regions of the three-phase boundary (TPB) near the electrolyte-electrode interface and the current collector.⁶²

However, even though the electrical conductivity of the ceria electrode is improved by the presence of graphitic carbon, the observed cell currents does not significantly change when carbon accumulated on the surface. The lack of current enhancement implies the CO₂ electrolysis reactions over CeO_{2-x} are no longer limited by the electron transport through CeO_{2-x}. It is possible the slow process of removing O²⁻ from the CeO_{2-x} catalyst to the YSZ electrolyte at ~600 °C becomes more rate-limiting in the overall electro-reduction of CO₂ in these investigated systems. Another possibility is that graphitic carbon species block the active sites on ceria and counteract the enhanced electronic conductivity.

5.3.4 Overpotentials at the Electrode-Electrolyte Interface

The single-sided SOC investigated in this study exhibits an OCV of 0 V when equilibrium is reached between the gas reactants and the electrode surfaces.

Therefore, the overpotentials, η , under applied biases can be directly calculated from the difference in local potentials of two elements at the same position.⁸⁰ More details of calculations of the overpotentials on these SOCs can be found in Chapter 2.

As shown in **Figure 5-5**, at -1.5 V applied bias, the overpotential $\eta_{L(\text{Pt-YSZ})}$ represented by the difference in Pt and Zr local potential is -1.0 V with a cell current (I) of +22 μA , whereas at +2.0 V, the overpotential $\eta_{L(\text{Pt-YSZ})}$ is +1.0 V with a -350 μA current. The larger ratio of $\eta_{L(\text{Pt-YSZ})}$ to I at -1.5 V reflects the much higher charge transfer resistance is associated with CO_2 electrolysis at the Pt-YSZ interface than CO electro-oxidation. This difference may result from the much lower affinity of CO_2 gas on Pt than CO. Also, the spillover oxygen⁸⁶ from YSZ to the Pt electrode at +2.0 V facilitates CO electro-oxidation at the Pt-YSZ interface, which further contributes to the relatively lower charge transfer resistance associated with the reaction.

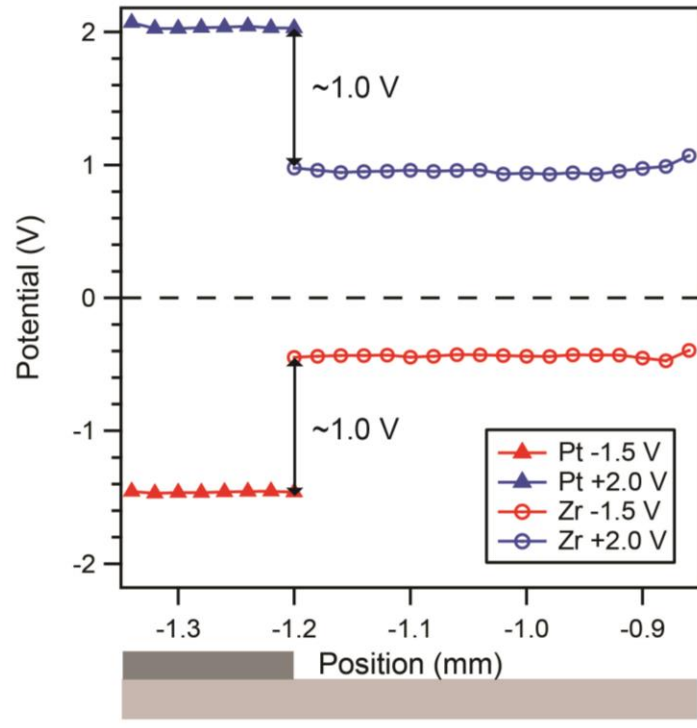


Figure 5-5. Plots of local surface potential extracted from the kinetic energy shifts in Pt 4f and Zr 3d photoelectrons relative to OCV condition. Data are collected *operando* under 1:20 CO/CO_2 gas environment at $\sim 600^\circ\text{C}$. The overpotentials at the Pt-YSZ interface are determined from the difference in local surface potentials of Pt and Zr at the same position.

5.3.5 Comparison with Studies of H₂/H₂O

Results of previous studies into H₂/H₂O system at the Pt-YSZ edge⁸⁰ is described in Chapter 2, Section 2.3.5. The +1.2 V applied bias results in $\eta_{L(\text{Pt-YSZ})} = 0.4$ V with -618 μA current and the -1.2 V bias shows a slightly larger η of 0.5 V at $I = 148$ μA (**Figure 2-13**).⁸⁰ Both the CO electro-oxidation and CO₂ electro-reduction reveal higher charge transfer resistances than the corresponding electrochemical reactions for H₂/H₂O. The lowest resistance for H₂ electro-oxidation at the Pt-YSZ interface could be explained by the spillover of hydrogen from Pt onto YSZ and the simultaneous spillover of oxygen⁹⁵ from YSZ to Pt under the positive bias condition.

5.4 Summary

Electro-reduction of CO₂ and electro-oxidation of CO over ceria-based SOCs is investigated through the use of *operando* AP-XPS in the presence of 0.5 Torr of CO/CO₂ gas mixtures at ~600 °C. During CO₂ electrolysis reactions on ceria at positive applied bias, the graphitic carbon formation is observed over a 400- μm -wide region on the CeO_{2-x} electrode surfaces. The formation of graphitic carbon at reducing conditions extends the electrochemically active region by enhancing the electronic conductivity of the CeO_{2-x}. Also, measurements of overpotentials at the Pt-YSZ edge reveal very high charge transfer resistance at the electrode-electrolyte interface for CO₂ electrolysis that dominated the cell losses in these environments. These results allow obtaining detailed understanding in reaction kinetics and mechanisms of CO₂ electrolysis and CO electro-oxidation on MIEC ceria-based electrocatalyst surfaces.

Chapter 6

Summary and Future Work

6.1 Introduction

The research described in this thesis has examined the electrochemical reactions of hydrogen-water mixture and carbon monoxide-carbon dioxide mixture on ceria-based solid oxide electrochemical cells (SOCs). A novel *operando* ambient pressure X-ray photoelectron spectroscopy (AP-XPS) technique has been utilized to probe solid oxide electrode surfaces under ambient pressure conditions and elevated operating temperatures of 600 - 700 °C. The successful implementation of this technique allowed for the direct measure of fundamental properties responsible for the electrode behaviors and SOC performances. Identification of reaction intermediates on the electrode surfaces under operating conditions, combined with the characterization of electrochemistry studies, provided unprecedented insight into the mechanism of reaction processes in solid oxide devices.

6.2 Summary of Major Results

6.2.1 Fundamental Characterization of Solid Oxide Electrochemical Cell Chemistry

Through the use of novel *operando* methods of AP-XPS in combination with voltammetry and impedance spectroscopy, a single-sided SOC was characterized

under operating conditions. With the two-dimensional (2D) imaging capability and enhanced spatial resolution of the AP-XPS end-stations at the Advanced Light Source (ALS) at Lawrence Berkeley National Laboratory (LBNL), fundamental properties of solid oxide electrochemical devices are characterized *operando* in details, including local surface potentials, electrode redox changes, overpotentials at the electrode-electrolyte interfaces, and surface potential steps at the gas-solid interface.

6.2.2 Reaction Intermediates and Mechanisms

Investigations into H₂O electrolysis ($\text{H}_2\text{O} + 2\text{e}^- \rightarrow \text{H}_2 + \text{O}^{2-}$) and H₂ electro-oxidation ($\text{H}_2 + \text{O}^{2-} \rightarrow \text{H}_2\text{O} + 2\text{e}^-$) on ceria reveal a transient build-up of surface intermediates (OH⁻ and Ce³⁺). Quantification of the relative amounts and locations of surface oxide species provides detailed understanding of O²⁻, OH⁻ and oxygen vacancy on the surface of an operating SOC electrode. Also, the potential separation between surface adsorbates OH⁻ and electrode O²⁻ that occur exclusively in the electrochemically active region represents the surface potential step of adsorbates at the gas-solid interface. The observations of surface potential step and increase in intermediate steady-state concentration suggest that the same charge transfer process ($\text{H}_2\text{O} + \text{Ce}^{3+} \leftrightarrow \text{Ce}^{4+} + \text{OH}^- + \text{H}\cdot$) is rate-limiting in both H₂O electrolysis and H₂ electro-oxidation reactions on ceria.

In similar studies, CO₂ electrolysis reactions ($\text{CO}_2 + 2\text{e}^- \rightarrow \text{CO} + \text{O}^{2-}$) and CO electro-oxidation reactions ($\text{CO} + \text{O}^{2-} \rightarrow \text{CO}_2 + 2\text{e}^-$) over ceria electrodes reveal that the electrolysis of CO₂ appear to go through a carbonate intermediate on the ceria surface. During CO₂ electrolysis the process of pre-coordination of CO₂ to the ceria surface to form a carbonate intermediate ($\text{CO}_2 + \text{O}^{2-}_{(\text{ceria})} \rightarrow \text{CO}_3^{2-}$) is identified

preceding a rate-limiting electron transfer process to CO_3^{2-} to give CO and oxide ions ($\text{CO}_3^{2-} + 2\text{e}^- \rightarrow \text{CO} + 2\text{O}^{2-}$).

These AP-XPS experiments provide a detailed picture of fundamental chemistry on operating SOCs. The charge separation at a gas-solid interface and the parameters governing electrochemical reactions of the cells such as intermediate species and rate-limiting processes are identified. These findings could be of significant value to next generation practical cell design and material selection.

6.3 Future Works & Recommendations

Quantitative correlations between electrochemical data and *operando* spectroscopic observations presented in this thesis has demonstrated their success of in the study of fuel cell chemistry. Despite the resulting advancements in the mechanistic understanding of electrolysis and fuel oxidation, there remains many unanswered questions.

6.3.1 Further Applications of *Operando* Techniques

One emphasis of future work should be extending the application of these *operando* diagnostic techniques to investigations of wider selection of electrochemical devices, *e.g.*, cermet electrodes and anode-supported solid oxide fuel cells (SOFCs). Detailed information obtained from these studies will be important in determining the chemical mechanisms responsible for operation with more complex hydrocarbon fuels.

Another focus is to realize the transition from single-sided SOCs to more practical double-sided SOFCs. The XPS results coupled with other advanced spectroscopic measurements, such as near infrared (NIR) and Raman, will provide a more comprehensive perspective into reaction mechanisms and other fundamental properties responsible for cell performance. The goal is to obtain a more general and complementary understanding on electrochemical reactions and to correlate the results from model, low pressure cells studies with those from electrochemical devices that are closer to practical conditions.

6.3.2 *Operando* Studies of Electrolysis on Solid Oxide Electrocatalyst

To fully understand the nature of the carbonate bonding on ceria surfaces (terminal versus bridging) and their difference in activity, Fourier transform infrared emission spectroscopy (FTIRES) is an ideal tool to resolve this problem because CO_3^{2-} has a strong IR band in the region near 1400 cm^{-1} . By incorporating isotopically enriched C^{18}O_2 in the electrolysis feeds and monitoring the equilibrium exchange rates relative to the exchange current densities, the kinetic information of electrolysis can potentially be obtained.

Also, the systematic studies of CO_2 and H_2O electrolysis individually described in this dissertation provide the basis to investigate the co-electrolysis of CO_2 and H_2O mixtures through *operando* experiments. For example, it is possible that new intermediates, such as formates, bicarbonates and other H-C-O molecular intermediates are formed during co-electrolysis, which are excluded from the individual electrolysis reactions. X-ray adsorption spectroscopy (XAS) studies can be

valuable as it provides more detailed information about the unoccupied states in the system.

6.3.3 Poisoning Mechanisms

Catalyst deactivation by impurities in the fuel stream, such as sulfur, presents one primary sources of fuel cell degradation.^{153–155} However, the current lack of the atomistic level understanding of sulfur poisoning impedes the development of new sulfur tolerance strategies. It is important to understand the mechanistic surface chemistry and bulk-phase chemistry of sulfur with SOFC anodes at elevated temperatures and far-from-equilibrium conditions, which is associated with operational SOFCs. Due to the lack of proper diagnostic technology, most of the investigations of sulfur poisoning, to date, have been conducted under equilibrium conditions and by *ex situ* methods. Studies that directly examine the far-from-equilibrium surface chemistry associated with sulfur poisoning in an operational SOFC has so far been limited to electrochemical characterizations.¹⁵⁶ Hence little has been achieved regarding the speciation of sulfur, the mechanism of sulfur poisoning on electrode surfaces, or the mechanisms that lead to sulfur removal.

Studies described in this work have shown that surface intermediates and shifts in electrode redox states can be identified through *operando* XPS analysis, which provides new insight into SOFC surface chemistry. Therefore, experiments utilizing these *operando* capabilities to study sulfur poisoning are promising. Specifically, the AP-XPS can be used to detect and identify sulfur-containing impurity species on SOFC anodes whereas X-ray diffraction (XRD) and XAS studies can provide information on bulk electrode properties. In particular, extended X-ray

absorption fine structure (EXAFS) and near edge X-ray absorption fine structure (NEXAFS) can monitor oxidation state changes and coordination geometries. Cermet electrodes and ceria-based systems can be investigated as representative cases. More importantly, the simultaneous measurements of electrochemistry and spectroscopy assure monitoring the sulfur poisoning process on SOFC anodes under *operando* conditions, providing a comprehensive picture of anode behavior during cell operation.

6.3.4 Characterization of Cathode Materials

The use of *operando* XPS, XRD, NEXAFS, and EXAFS can also be applied in evaluating cathode materials. These *operando* studies will provide a detailed picture of surface and bulk chemistry of cathode structures under operational conditions. In addition, the complementary *operando* investigation will cover a continuum of experimental conditions ranging from the relatively low pressure in synchrotron based experiments to the high pressure, high current density experiments in practical device applications. One additional promising technique for oxidation state analysis of cathode material is the Auger method, especially for catalysts containing transition metals, *e.g.*, Co, Fe, and Mn. The oxygen polarization information from Auger measurement can also provide insights into the understanding of surface adsorbate behavior and the surface potential step at gas-solid interface.

References

- (1) Minh, N. Q. *J. Am. Ceram. Soc.* **1993**, *76*, 563.
- (2) Ormerod, R. M. *Chem. Soc. Rev.* **2003**, *32*, 17.
- (3) Pomfret, M. B.; Owrutsky, J. C.; Walker, R. A. *Annu. Rev. Anal. Chem.* **2010**, *3*, 151.
- (4) Singhal, S. *High-temperature Solid Oxide Fuel Cells: Fundamentals, Design and Applications: Fundamentals, Design and Applications*; Elsevier, 2003.
- (5) Fergus, J.; Hui, R.; Li, X.; Wilkinson, D. P.; Zhang, J. *Solid Oxide Fuel Cells: Materials Properties and Performance*; CRC Press, 2008.
- (6) Grove, W. R. *Philos. Mag. Ser. 3* **1839**, *14*, 127.
- (7) Etsell, T. H.; Flengas, S. N. *Chem. Rev.* **1970**, *70*, 339.
- (8) Steele, B. C. H.; Heinzl, A. *Nature* **2001**, *414*, 345.
- (9) Heraeus, W. C. *Z. Für Elektrochem.* **1899**, *6*, 41.
- (10) Möbius, H.-H. *Naturwissenschaften* **1965**, *52*, 529.
- (11) Baur, E.; Preis, H. *Z. Für Elektrochem. Angew. Phys. Chem.* **1937**, *43*, 727.
- (12) Taroco, H. A.; F. Santos, J. A. F.; Domingues, R. Z.; Matencio, T. In *Advances in Ceramics - Synthesis and Characterization, Processing and Specific Applications*; Sikalidis, C., Ed.; InTech, 2011.
- (13) Nguyen, Q. M. *Science and technology of ceramic fuel cells*; Elsevier Science: Amsterdam ; New York, 1995.
- (14) Heuer, A. H.; Society, A. C. *Science and technology of zirconia II*; American Ceramic Society, 1984.

- (15) Tuller, H. L.; Nowick, A. S. *J. Electrochem. Soc.* **1975**, *122*, 255.
- (16) Fu, D.; Itoh, M. In *Ferroelectrics - Material Aspects*; Lallart, M., Ed.; InTech, 2011.
- (17) Tedmon, C. S.; Spacil, H. S.; Mitoff, S. P. *J. Electrochem. Soc.* **1969**, *116*, 1170.
- (18) Brett, D. J. L.; Kucernak, A. R.; Aguiar, P.; Atkins, S. C.; Brandon, N. P.; Clague, R.; Cohen, L. F.; Hinds, G.; Kalyvas, C.; Offer, G. J.; Ladewig, B.; Maher, R.; Marquis, A.; Shearing, P.; Vasileiadis, N.; Vesovic, V. *ChemPhysChem* **2010**, *11*, 2714.
- (19) Singhal, S. C.; Dokiya, M. *Solid Oxide Fuel Cells (SOFC VI): Proceedings of the Sixth International Symposium*; The Electrochemical Society, 1999.
- (20) Pomfret, M. B.; Marda, J.; Jackson, G. S.; Eichhorn, B. W.; Dean, A. M.; Walker, R. A. *J. Phys. Chem. C* **2008**, *112*, 5232.
- (21) Mogensen, M. *Solid State Ion.* **2000**, *129*, 63.
- (22) Murray, E. P.; Tsai, T.; Barnett, S. A. *Nature* **1999**, *400*, 649.
- (23) Park, S.; Vohs, J. M.; Gorte, R. J. *Nature* **2000**, *404*, 265.
- (24) Tao, S.; Irvine, J. T. S. *Nat. Mater.* **2003**, *2*, 320.
- (25) Huang, Y.-H.; Dass, R. I.; Xing, Z.-L.; Goodenough, J. B. *Science* **2006**, *312*, 254.
- (26) Yang, L.; Wang, S.; Blinn, K.; Liu, M.; Liu, Z.; Cheng, Z.; Liu, M. *Science* **2009**, *326*, 126.
- (27) Chueh, W. C.; Hao, Y.; Jung, W.; Haile, S. M. *Nat. Mater.* **2012**, *11*, 155.
- (28) Senanayake, S. D.; Stacchiola, D.; Evans, J.; Estrella, M.; Barrio, L.; Pérez, M.; Hrbek, J.; Rodriguez, J. A. *J. Catal.* **2010**, *271*, 392.

- (29) Mudiyansele, K.; Senanayake, S. D.; Fera, L.; Kundu, S.; Baber, A. E.; Graciani, J.; Vidal, A. B.; Agnoli, S.; Evans, J.; Chang, R.; Axnanda, S.; Liu, Z.; Sanz, J. F.; Liu, P.; Rodriguez, J. A.; Stacchiola, D. J. *Angew. Chem. Int. Ed.* **2013**, *52*, 5101.
- (30) Zhang, C.; Yu, Y.; Grass, M. E.; Dejoie, C.; Ding, W.; Gaskell, K.; Jabeen, N.; Hong, Y. P.; Shavorskiy, A.; Bluhm, H.; Li, W.-X.; Jackson, G. S.; Hussain, Z.; Liu, Z.; Eichhorn, B. W. *J. Am. Chem. Soc.* **2013**, *135*, 11572.
- (31) *Catalysis by ceria and related materials*; Catalytic science series; Imperial College Press: London, 2002.
- (32) Miki, T.; Ogawa, T.; Haneda, M.; Kakuta, N.; Ueno, A.; Tateishi, S.; Matsuura, S.; Sato, M. *J. Phys. Chem.* **1990**, *94*, 6464.
- (33) Chueh, W. C.; Haile, S. M. *Philos. Trans. R. Soc. Math. Phys. Eng. Sci.* **2010**, *368*, 3269.
- (34) Blumenthal, R. N.; Pinz, B. A. *J. Appl. Phys.* **1967**, *38*, 2376.
- (35) Naik, I. K.; Tien, T. Y. *J. Phys. Chem. Solids* **1978**, *39*, 311.
- (36) Brugner, F. S.; Blumenthal, R. N. *J. Am. Ceram. Soc.* **1971**, *54*, 57.
- (37) Faulkner, L. R. *J. Electrochem. Soc.* **1988**, *135*, 245C.
- (38) Briggs, D.; Seah, M. P. *Practical surface analysis: by auger and x-ray photoelectron spectroscopy*; Wiley, 1983.
- (39) Corcoran, C. J.; Tavassol, H.; Rigsby, M. A.; Bagus, P. S.; Wieckowski, A. *J. Power Sources* **2010**, *195*, 7856.
- (40) Nilsson, A. *J. Electron Spectrosc. Relat. Phenom.* **2002**, *126*, 3.

- (41) Axnanda, S.; Scheele, M.; Crumlin, E.; Mao, B.; Chang, R.; Rani, S.; Faiz, M.; Wang, S.; Alivisatos, A. P.; Liu, Z. *Nano Lett.* **2013**, *13*, 6176.
- (42) NIST Standard Reference Database 20, Version 4.1
<http://srdata.nist.gov/xps/Default.aspx> (accessed Apr 13, 2013).
- (43) Seah, M. P.; Dench, W. A. *Surf. Interface Anal.* **1979**, *1*, 2.
- (44) Bluhm, H. *J. Electron Spectrosc. Relat. Phenom.* **2010**, *177*, 71.
- (45) Crumlin, E. J.; Bluhm, H.; Liu, Z. *J. Electron Spectrosc. Relat. Phenom.* **2013**, *190, Part A*, 84.
- (46) Elder, F. R.; Langmuir, R. V.; Pollock, H. C. *Phys. Rev.* **1948**, *74*, 52.
- (47) Willmott, P. *An Introduction to Synchrotron Radiation: Techniques and Applications*; John Wiley & Sons, Ltd: Chichester, UK, 2011.
- (48) Winick, H.; Bienenstock, A. *Annu. Rev. Nucl. Part. Sci.* **1978**, *28*, 33.
- (49) Kim, K.-J. In *AIP Conference Proceedings*; AIP Publishing, 1989; Vol. 184, pp. 565–632.
- (50) Attwood, D. T. *Soft x-rays and extreme ultraviolet radiation: principles and applications*; Cambridge University Press: Cambridge ; New York, 2000.
- (51) Siegbarn, H.; Asplund, L.; Kelfve, P.; Hamrin, K.; Karlsson, L.; Siegbahn, K. *J. Electron Spectrosc. Relat. Phenom.* **1974**, *5*, 1059.
- (52) Fellner-Feldegg, H.; Siegbahn, H.; Asplund, L.; Kelfve, P.; Siegbahn, K. *J. Electron Spectrosc. Relat. Phenom.* **1975**, *7*, 421.
- (53) Siegbahn, H. *J. Phys. Chem.* **1985**, *89*, 897.
- (54) Ogletree, D. F.; Bluhm, H.; Lebedev, G.; Fadley, C. S.; Hussain, Z.; Salmeron, M. *Rev. Sci. Instrum.* **2002**, *73*, 3872.

- (55) Bluhm, H.; Andersson, K.; Araki, T.; Benzerara, K.; Brown, G. E.; Dynes, J. J.; Ghosal, S.; Gilles, M. K.; Hansen, H.-C.; Hemminger, J. C.; Hitchcock, A. P.; Ketteler, G.; Kilcoyne, A. L. D.; Kneedler, E.; Lawrence, J. R.; Leppard, G. G.; Majzlam, J.; Mun, B. S.; Myneni, S. C. B.; Nilsson, A.; Ogasawara, H.; Ogletree, D. F.; Pecher, K.; Salmeron, M.; Shuh, D. K.; Tonner, B.; Tyliczszak, T.; Warwick, T.; Yoon, T. H. *J. Electron Spectrosc. Relat. Phenom.* **2006**, *150*, 86.
- (56) Zhang, C.; Grass, M. E.; McDaniel, A. H.; DeCaluwe, S. C.; Gabaly, F. E.; Liu, Z.; McCarty, K. F.; Farrow, R. L.; Linne, M. A.; Hussain, Z.; Jackson, G. S.; Bluhm, H.; Eichhorn, B. W. *Nat. Mater.* **2010**, *9*, 944.
- (57) Salmeron, M.; Schlogl, R. *Surf. Sci. Rep.* **2008**, *63*, 169.
- (58) Gurlo, A.; Riedel, R. *Angew. Chem. Int. Ed.* **2007**, *46*, 3826.
- (59) Haw, J. F. In *In-Situ Spectroscopy in Heterogeneous Catalysis*; Haw, J. F., Ed.; Wiley-VCH Verlag GmbH & Co. KGaA, 2002; pp. 1–14.
- (60) Schlögl, R. In *Basic Principles in Applied Catalysis*; Baerns, P. D. M., Ed.; Springer Series in Chemical Physics; Springer Berlin Heidelberg, 2004; pp. 321–360.
- (61) Caillol, N.; Pijolat, M.; Siebert, E. *Appl. Surf. Sci.* **2007**, *253*, 4641.
- (62) McIntosh, S.; He, H.; Lee, S.-I.; Costa-Nunes, O.; Krishnan, V. V.; Vohs, J. M.; Gorte, R. J. *J. Electrochem. Soc.* **2004**, *151*, A604.
- (63) Tikekar, N. M.; Armstrong, T. J.; Virkar, A. V. *J. Electrochem. Soc.* **2006**, *153*, A654.
- (64) Lai, W.; Haile, S. M. *J. Am. Ceram. Soc.* **2005**, *88*, 2979.

- (65) Graves, C.; Ebbesen, S. D.; Mogensen, M.; Lackner, K. S. *Renew. Sustain. Energy Rev.* **2011**, *15*, 1.
- (66) Nicholas, J. D. *Electrochem. Soc. Interface* **2013**, *22*, 49.
- (67) Fleig, J. *Phys. Chem. Chem. Phys.* **2005**, *7*, 2027.
- (68) Cheng, Z.; Liu, M. *Solid State Ion.* **2007**, *178*, 925.
- (69) Pomfret, M. B.; Owrutsky, J. C.; Walker, R. A. *Anal. Chem.* **2007**, *79*, 2367.
- (70) El Gabaly, F.; Grass, M.; McDaniel, A. H.; Farrow, R. L.; Linne, M. A.; Hussain, Z.; Bluhm, H.; Liu, Z.; McCarty, K. F. *Phys. Chem. Chem. Phys.* **2010**, *12*, 12138.
- (71) Liu, D.-J.; Almer, J. *Appl. Phys. Lett.* **2009**, *94*, 224106.
- (72) Shinoda, K.; Suzuki, S.; Yashiro, K.; Mizusaki, J.; Uruga, T.; Tanida, H.; Toyokawa, H.; Terada, Y.; Takagaki, M. *Surf. Interface Anal.* **2010**, *42*, 1650.
- (73) Ladas, S.; Kennou, S.; Bebelis, S.; Vayenas, C. G. *J. Phys. Chem.* **1993**, *97*, 8845.
- (74) Siegbahn, H.; Lundholm, M. *J. Electron Spectrosc. Relat. Phenom.* **1982**, *28*, 135.
- (75) Doron-Mor, I.; Hatzor, A.; Vaskevich, A.; van der Boom-Moav, T.; Shanzer, A.; Rubinstein, I.; Cohen, H. *Nature* **2000**, *406*, 382.
- (76) Ertas, G.; Suzer, S. In *Surface Chemistry in Biomedical and Environmental Science*; Blitz, P. J. P.; Gun'ko, P. V. M., Eds.; Springer Netherlands, 2006; pp. 45–58.
- (77) Grass, M. E.; Karlsson, P. G.; Aksoy, F.; Lundqvist, M.; Wannberg, B.; Mun, B. S.; Hussain, Z.; Liu, Z. *Rev. Sci. Instrum.* **2010**, *81*, 053106.

- (78) Whaley, J. A.; McDaniel, A. H.; El Gabaly, F.; Farrow, R. L.; Grass, M. E.; Hussain, Z.; Liu, Z.; Linne, M. A.; Bluhm, H.; McCarty, K. F. *Rev. Sci. Instrum.* **2010**, *81*, 086104.
- (79) DeCaluwe, S. C.; Grass, M. E.; Zhang, C.; Gabaly, F. E.; Bluhm, H.; Liu, Z.; Jackson, G. S.; McDaniel, A. H.; McCarty, K. F.; Farrow, R. L.; Linne, M. A.; Hussain, Z.; Eichhorn, B. W. *J. Phys. Chem. C* **2010**, *114*, 19853.
- (80) Zhang, C.; Grass, M. E.; Yu, Y.; Gaskell, K. J.; DeCaluwe, S. C.; Chang, R.; Jackson, G. S.; Hussain, Z.; Bluhm, H.; Eichhorn, B. W.; Liu, Z. *ACS Catal.* **2012**, *2*, 2297.
- (81) Zhang, C.; Grass, M. E.; DeCaluwe, S. C.; Liu, Z.; Bluhm, H.; Hussain, Z.; Jackson, G. S.; Eichhorn, B. W. *ECS Trans.* **2011**, *33*, 19.
- (82) Mizusaki, J. *Solid State Ion.* **1992**, *53-56*, 126.
- (83) Jang, S.-E.; Kim, H. *J. Am. Chem. Soc.* **2010**, *132*, 14700.
- (84) Xu, F.; Wang, M.; Liu, Q.; Sun, H.; Simonson, S.; Ogbeifun, N.; Stach, E. A.; Xie, J. *J. Electrochem. Soc.* **2010**, *157*, B1138.
- (85) Ziomek-Moroz, M. E.; Adler, T.; Alman, D. E.; Jablonski, P. D.; Clark, J.; Penner, L. ECS, 2008; Vol. 12, pp. 273–281.
- (86) Vayenas, C. G.; Koutsodontis, C. G. *J. Chem. Phys.* **2008**, *128*, 182506.
- (87) Bard, A. J. *Electrochemical methods: fundamentals and applications*; 2nd ed.; Wiley: New York, 2001.
- (88) Greiner, M. T.; Helander, M. G.; Tang, W.-M.; Wang, Z.-B.; Qiu, J.; Lu, Z.-H. *Nat. Mater.* **2011**, *11*, 76.
- (89) Imbihl, R. *Prog. Surf. Sci.* **2010**, *85*, 241.

- (90) Somorjai, G. A.; Park, J. Y. *Chem. Soc. Rev.* **2008**, *37*, 2155.
- (91) Diebold, U. *Surf. Sci. Rep.* **2003**, *48*, 53.
- (92) Sun, C.; Li, H.; Chen, L. *Energy Environ. Sci.* **2012**, *5*, 8475.
- (93) Mutoro, E.; Crumlin, E. J.; Pöpke, H.; Luerssen, B.; Amati, M.; Abyaneh, M. K.; Biegalski, M. D.; Christen, H. M.; Gregoratti, L.; Janek, J.; Shao-Horn, Y. *J. Phys. Chem. Lett.* **2012**, *3*, 40.
- (94) Ganduglia-Pirovano, M. V.; Hofmann, A.; Sauer, J. *Surf. Sci. Rep.* **2007**, *62*, 219.
- (95) *Electrochemical activation of catalysis: promotion, electrochemical promotion, and metal-support interactions*; Kluwer Academic/Plenum Publishers: New York, 2001.
- (96) Zhu, H.; Kee, R. J.; Janardhanan, V. M.; Deutschmann, O.; Goodwin, D. G. *J. Electrochem. Soc.* **2005**, *152*, A2427.
- (97) Kharton, V. V.; Figueiredo, F. M.; Navarro, L.; Naumovich, E. N.; Kovalevsky, A. V.; Yaremchenko, A. A.; Viskup, A. P.; Carneiro, A.; Marques, F. M. B.; Frade, J. R. *J. Mater. Sci.* **2001**, *36*, 1105.
- (98) Liu, X.; Zhou, K.; Wang, L.; Wang, B.; Li, Y. *J. Am. Chem. Soc.* **2009**, *131*, 3140.
- (99) Campbell, C. T. *Science* **2005**, *309*, 713.
- (100) Esch, F. *Science* **2005**, *309*, 752.
- (101) *The CRC handbook of solid state electrochemistry*; CRC Press: Boca Raton, Fla, 1997.
- (102) Mullins, D. .; Overbury, S. .; Huntley, D. . *Surf. Sci.* **1998**, *409*, 307.

- (103) Duhm, S.; Heimel, G.; Salzmann, I.; Glowatzki, H.; Johnson, R. L.; Vollmer, A.; Rabe, J. P.; Koch, N. *Nat. Mater.* **2008**, *7*, 326.
- (104) Xie, Y.; Hikita, Y.; Bell, C.; Hwang, H. Y. *Nat. Commun.* **2011**, *2*, 494.
- (105) Vázquez, H.; Dappe, Y. J.; Ortega, J.; Flores, F. J. *Chem. Phys.* **2007**, *126*, 144703.
- (106) Schmickler, W.; Santos, E. *Interfacial electrochemistry*; Springer: Heidelberg; New York, 2010.
- (107) *Chemical bonding at surfaces and interfaces*; 1st ed.; Elsevier: Amsterdam ; Boston [Mass.], 2008.
- (108) El Gabaly, F.; McDaniel, A. H.; Grass, M.; Chueh, W. C.; Bluhm, H.; Liu, Z.; McCarty, K. F. *Chem. Commun.* **2012**, *48*, 8338.
- (109) Adler, S. B. *Chem. Rev.* **2004**, *104*, 4791.
- (110) Vetter, K. . *Electrochemical kinetics: theoretical and experimental aspects*; Academic Press: New York, N.Y, 1967.
- (111) Bockris, J. O. *Modern electrochemistry*; 2nd ed.; Plenum Press: New York, 1998.
- (112) *CRC Handbook of Chemistry and Physics, 95th Edition*.
- (113) Lim, R. J.; Xie, M.; Sk, M. A.; Lee, J.-M.; Fisher, A.; Wang, X.; Lim, K. H. *Catal. Today* **2013**.
- (114) Kondratenko, E. V.; Mul, G.; Baltrusaitis, J.; Larrazábal, G. O.; Pérez-Ramírez, J. *Energy Environ. Sci.* **2013**, *6*, 3112.
- (115) Benson, E. E.; Kubiak, C. P.; Sathrum, A. J.; Smieja, J. M. *Chem. Soc. Rev.* **2008**, *38*, 89.

- (116) Sav éant, J.-M. *Chem. Rev.* **2008**, *108*, 2348.
- (117) Hori, Y.; Murata, A.; Takahashi, R. *J. Chem. Soc. Faraday Trans. 1 Phys. Chem. Condens. Phases* **1989**, *85*, 2309.
- (118) Hori, Y. In *Handbook of Fuel Cells*; John Wiley & Sons, Ltd, 2010.
- (119) Sridhar, K. R.; Vaniman, B. T. *Solid State Ion.* **1997**, *93*, 321.
- (120) Ebbesen, S. D.; Mogensen, M. *J. Power Sources* **2009**, *193*, 349.
- (121) Zhan, Z.; Zhao, L. *J. Power Sources* **2010**, *195*, 7250.
- (122) Yue, X.; Irvine, J. T. S. *J. Electrochem. Soc.* **2012**, *159*, F442.
- (123) Bidrawn, F.; Kim, G.; Corre, G.; Irvine, J. T. S.; Vohs, J. M.; Gorte, R. J. *Electrochem. Solid-State Lett.* **2008**, *11*, B167.
- (124) Green, R. D.; Liu, C.-C.; Adler, S. B. *Solid State Ion.* **2008**, *179*, 647.
- (125) Cheng, C.-Y.; Kelsall, G. H.; Kleiminger, L. *J. Appl. Electrochem.* **2013**, *43*, 1131.
- (126) Miller, J. E.; Allendorf, M. D.; Diver, R. B.; Evans, L. R.; Siegel, N. P.; Stuecker, J. N. *J. Mater. Sci.* **2008**, *43*, 4714.
- (127) Singh, P.; Hegde, M. S. *Chem. Mater.* **2010**, *22*, 762.
- (128) Chueh, W. C.; Haile, S. M. *ChemSusChem* **2009**, *2*, 735.
- (129) Abanades, S.; Legal, A.; Cordier, A.; Peraudeau, G.; Flamant, G.; Julbe, A. *J. Mater. Sci.* **2010**, *45*, 4163.
- (130) Atkinson, A.; Barnett, S.; Gorte, R. J.; Irvine, J. T. S.; McEvoy, A. J.; Mogensen, M.; Singhal, S. C.; Vohs, J. *Nat. Mater.* **2004**, *3*, 17.
- (131) Li, C.; Sakata, Y.; Arai, T.; Domen, K.; Maruya, K.; Onishi, T. *J. Chem. Soc. Faraday Trans. 1 Phys. Chem. Condens. Phases* **1989**, *85*, 929.

- (132) Bradford, M. C. J.; Vannice, M. A. *Catal. Rev.* **1999**, *41*, 1.
- (133) Cheng, Z.; Sherman, B. J.; Lo, C. S. *J. Chem. Phys.* **2013**, *138*, 014702.
- (134) Staudt, T.; Lykhach, Y.; Tsud, N.; Skála, T.; Prince, K. C.; Matolín, V.; Libuda, J. *J. Phys. Chem. C* **2011**, *115*, 8716.
- (135) Wu, Z.; Li, M.; Overbury, S. H. *J. Catal.* **2012**, *285*, 61.
- (136) Yu, Y.; Geller, A. I.; Mao, B.; Chang, R.; Liu, Z.; Eichhorn, B. W. *ECS Trans.* **2013**, *57*, 3119.
- (137) Yamamoto, S.; Bluhm, H.; Andersson, K.; Ketteler, G.; Ogasawara, H.; Salmeron, M.; Nilsson, A. *J. Phys. Condens. Matter* **2008**, *20*, 184025.
- (138) Senanayake, S. D.; Mullins, D. R. *J. Phys. Chem. C* **2008**, *112*, 9744.
- (139) Lykhach, Y.; Staudt, T.; Streber, R.; Lorenz, M. P. A.; Bayer, A.; Steinrück, H.-P.; Libuda, J. *Eur. Phys. J. B* **2010**, *75*, 89.
- (140) Brittain, H. G.; Sachs, C. J.; Lynch, J. F.; Ogle, K. M.; Perry, D. L. *Inorganica Chim. Acta* **1987**, *127*, 229.
- (141) Matta, J.; Courcot, D.; Abi-Aad, E.; Aboukaš, A. *J. Therm. Anal. Calorim.* **2001**, *66*, 717.
- (142) Li, J.-T.; Swiatowska, J.; Seyeux, A.; Huang, L.; Maurice, V.; Sun, S.-G.; Marcus, P. *J. Power Sources* **2010**, *195*, 8251.
- (143) Albrecht, P. M.; Mullins, D. R. *Langmuir* **2013**, *29*, 4559.
- (144) Engelhard, M.; Azad, S.; Peden, C. H. F.; Thevuthasan, S. *Surf. Sci. Spectra* **2004**, *11*, 73.
- (145) Freund, H.-J.; Roberts, M. W. *Surf. Sci. Rep.* **1996**, *25*, 225.
- (146) Appel, L. G.; Eon, J. G.; Schmal, M. *Catal. Lett.* **1998**, *56*, 199.

- (147) Arakawa, H.; Aresta, M.; Armor, J. N.; Barteau, M. A.; Beckman, E. J.; Bell, A. T.; Bercaw, J. E.; Creutz, C.; Dinjus, E.; Dixon, D. A.; Domen, K.; DuBois, D. L.; Eckert, J.; Fujita, E.; Gibson, D. H.; Goddard, W. A.; Goodman, D. W.; Keller, J.; Kubas, G. J.; Kung, H. H.; Lyons, J. E.; Manzer, L. E.; Marks, T. J.; Morokuma, K.; Nicholas, K. M.; Periana, R.; Que, L.; Rostrup-Nielson, J.; Sachtler, W. M.; Schmidt, L. D.; Sen, A.; Somorjai, G. A.; Stair, P. C.; Stults, B. R.; Tumas, W. *Chem. Rev.* **2001**, *101*, 953.
- (148) Chueh, W. C.; Falter, C.; Abbott, M.; Scipio, D.; Furler, P.; Haile, S. M.; Steinfeld, A. *Science* **2010**, *330*, 1797.
- (149) Liu, Y.; Wen, C.; Guo, Y.; Liu, X.; Ren, J.; Lu, G.; Wang, Y. *ChemCatChem* **2010**, *2*, 336.
- (150) Swanson, M.; Pushkarev, V. V.; Kovalchuk, V. I.; d' Itri, J. L. *Catal. Lett.* **2007**, *116*, 41.
- (151) Li, C.; Sakata, Y.; Arai, T.; Domen, K.; Maruya, K.; Onishi, T. *J. Chem. Soc. Chem. Commun.* **1991**, 410.
- (152) Holmgren, A.; Andersson, B.; Duprez, D. *Appl. Catal. B Environ.* **1999**, *22*, 215.
- (153) Pomfret, M. B.; Pietron, J. J.; Owrutsky, J. C. *Langmuir* **2010**, *26*, 6809.
- (154) Swider-Lyons, K. E.; Campbell, S. A. *J. Phys. Chem. Lett.* **2013**, *4*, 393.
- (155) Netwall, C. J.; Gould, B. D.; Rodgers, J. A.; Nasello, N. J.; Swider-Lyons, K. *E. J. Power Sources* **2013**, *227*, 137.
- (156) Cheng, Z.; Wang, J.-H.; Choi, Y.; Yang, L.; Lin, M. C.; Liu, M. *Energy Environ. Sci.* **2011**, *4*, 4380.